Analysis of the Scratch Test for Cohesive-Frictional Materials

by

Romain Bard

Ingénieur diplômé de l'École Polytechnique (2008)

Submitted to the Department of Mechanical Engineering
in partial fulfillment of the requirements for the degree of

Master of Science in Mechanical Engineering

at the

MASSACHUSETTS INSTITUTE OF TECHNOLOGY

June 2010

Author .....
Department of Mechanical Engineering
May 20, 2010

Certified by .....
Franz-Josef Ulm
Professor of Civil and Environmental Engineering
Thesis Supervisor

Certified by .....
Lallit Anand
Professor of Mechanical Engineering
Thesis Reader

Accepted by .....
David E. Hardt
Chairman, Departmental Committee on Graduate Students

Analysis of the Scratch Test for Cohesive-Frictional Materials

by

Romain Bard

Submitted to the Department of Mechanical Engineering
on May 20, 2010, in partial fulfillment of the
requirements for the degree of
Master of Science in Mechanical Engineering

Abstract

In this thesis we develop analytical solutions for the relations between scratch hardness and strength properties of cohesive-frictional materials of the Mohr-Coulomb and Drucker-Prager type. Based on the lower-bound yield design approach, closed form solutions are derived for frictionless scratch devices, and validated against computational upper bound and elastoplastic Finite Element solutions. The influence of friction at the blade–material interface is also investigated, for which a simple computational optimization is proposed.
The model is extended to porous cohesive-frictional materials through the use of a homogenized strength criterion based on the Linear Comparison Composite theory. Relations between scratch hardness, porosity and strength properties are proposed in the form of fitted functions.
Illustrated for scratch tests on cement paste, we show that the proposed solutions provide a convenient way to determine estimates of cohesion and friction parameters from scratch data, and may serve as a benchmark to identify the relevance of strength models for scratch test analysis.

Thesis Supervisor: Franz-Josef Ulm
Title: Professor of Civil and Environmental Engineering

Acknowledgments

First, I want to express my deep gratitude to Prof. Franz-Josef Ulm for exceeding all the expectations one can have about an academic supervisor. His scientific guidance has been key for the completion of my Master's degree. His selfless care for his students has added a priceless personal component to the rewarding experience of working for him.

Besides, my Master of Science at MIT could not have been a success without all the friends God put on my way during these 21 months. I want to thank the "French squad" (Damien, Nadège, Matthieu, Per Einar, Martin...), the research group "RedCements" (Alberto, Jimmy, Zenzile, Rouzbeh, Angie, MJ, Amer, Muhannad, Hegoi, Simone), and my GCF friends (Yong, Jon, Kevin, Heather...), for their continuous support and all the good times they shared with me.

Finally, I gratefully acknowledge that this work was made possible by the funding provided by the MIT–OU–GeoGenome Industry Consortium, directed by Prof. Younane Abousleiman.

Contents

List of Figures

List of Tables

Part I

General Presentation

Chapter 1

Introduction

1.1 Industrial Context

The scratch test is most likely the oldest mechanics-of-materials test for property characterization. It suffices to recall the Mohs scale of mineral hardness which rationalized, in 1822, the scratch resistance into a quantitative metric for the classification of various minerals [39]. The idea of the scratch test is simple: plowing and cutting with a scratch device the surface of a weaker material; and quantifying the scratch resistance by means of the scratch hardness [66]:

$$H_S \stackrel{def}{=} \frac{F_T}{A_{LB}} \tag{1.1}$$

where F_T is the horizontal force applied to the apparatus; and A_{LB} is the projected load bearing area resisting the horizontal force; that is, the horizontal projection of the contact area between the scratch device and the scratched material. Thanks to progress in force and depth sensing measurement devices, the scratch test remains a popular alternative to other material property test methods, and is relevant today in many fields of engineering, ranging from macroscopic testing of adhesion properties of coatings [49], to damage and wear of metals and polymers [67], [12], and strength of rocks [50], [51], [55].

1.2 Research Objectives and Approach

The combination of advanced theoretical micromechanics and nanoindentation makes it possible to understand and measure the properties of complex materials at micro- or even nanoscopic scale. The technique developed by Ganneau, Constantinides and Ulm [25] on cementitious materials, and by Gathier, Ortega and Ulm [43] on shales, relies on the determination of two mechanical properties at the microscale: elasticity and strength through the indentation modulus and hardness respectively. The overall objective of the present work is to find relationships between material properties and quantities measurable in a scratch test.

Our approach is based on yield design theory. Approximating the stress field that develops in scratch tests, by a simple piecewise constant field depending on a few degrees of freedom enables us to find explicit relations between scratch hardness, material properties and geometric parameters of the test. This approach yields a lower bound for the actual scratch hardness and is then validated by means of a combination of the complementary approach of yield design theory, the upper bound approach, and by finite element simulations of elastoplastic materials. Finally, the application of these relations to real scratch tests on cement paste and rocks shows both the potential and the limits of the strength model.

1.3 Thesis Outline

This thesis is divided in four parts: Part I briefly introduces the reader to the scratch test, and sits the stage for the analysis by introducing assumptions and hypotheses on which the model is based. Part II is devoted to the development and validation of a lower bound model for the scratch test. The hardness–strength relations derived from this model are compared with three other models: a simple upper bound model, an advanced limit analysis solver yielding an upper bound for the hardness, and elasto-plastic finite element simulations. In Part III, we show a possible extension of the model to porous cohesive-frictional material by the implementation of a homogenized

strength criterion. Then we show an application of the model to actual scratch tests performed on cement paste. In the final part, we discuss the limits of the strength approach and means of overcoming these limitations by accounting for the possibility of fracture. This leads us to the conclusion and perspectives for further work.

1.4 Research Significance

The scratch test is commonly used in industry to measure material properties. While it is very appropriate to measure quantities such as the adhesion of coating or the resistance to wear in frictional contact situations, the use of the scratch test to measure classic material properties such as yield stress requires better models based on a mechanistic understanding of the scratch test. Various analyses have been conducted on different materials but to our knowledge no result on frictional material is available: in this thesis we show how scratch hardness of materials represented by a Drucker-Prager or a Mohr-Coulomb criterion relates to the cohesion and internal friction. Validated against finite element simulations, the main contribution of this model is its simplicity which enables us to find explicit relations between hardness, strength properties, and geometry of the test. These relations can be used as benchmark for refined analysis of the scratch test.

Chapter 2

Presentation of the scratch test

2.1 Overall Presentation

The scratch test consists in pulling a hard indenter through a softer material (Figure 2-1). Yet, the simplicity of the procedure belies its complexity. In fact, a combination of the following parameters affects the scratch response:

- The geometry of the test;
- The loading conditions: most tests are either realized at constant scratch speed and controlled vertical loading, or constant scratch speed and controlled depth of scratch;
- Interface properties: friction can occur at the interface.

2.1.1 Dimensional Analysis

Dimensional analysis [5] is a powerful tool often used in science to understand physical situations involving various quantities. The fundamental idea is that physical laws do not depend on arbitrarily chosen basic units of measurement. This basic idea leads to the so-called Π-theorem which has been attributed to Buckingham [13]. It allows one to identify key ratios in the problem and to reduce the number of parameters in the different mathematical expressions. Dimensional analysis has proven to be useful

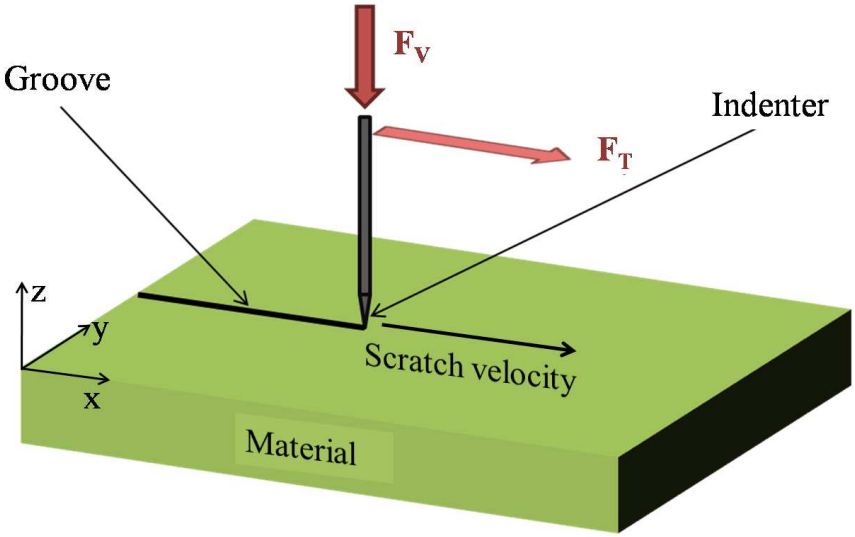

Figure 2-1: Schematic of the scratch test

to the study of the contact mechanics for instrumented normal indentation [20]. We follow here a similar approach on the steady-state scratch test.

We first choose our set of dependent variables, *i.e.* the quantities measured during a scratch test and for which we seek predictive relationships with the controllable parameters:

- The force required to pull the blade through the material at constant depth: $\underline{F} = F_T \underline{e}_x - F_V \underline{e}_z$ (see Figure 2-1), where $(\underline{e}_x, \underline{e}_y, \underline{e}_z)$ are the basis vectors used throughout this work, the $x-$direction being the direction of the scratch, F_T is the tangential force, and F_V is the normal, or vertical, force applied on the indenter.

- The contact area A_c between the indenter and the material. We define the load-bearing contact area A_{LB} as the horizontal projection of A_c. It enters the tangential hardness definition (1.1) and represents the effective area through which the tangential force F_T is transmitted from the indenter to the material.

These variables depend on the test parameters, namely:

- The geometry of the test: There exist different geometries for the scratch test. We will denote d_j $(j = 0, ..., n-1)$ and θ_k $(k = 1, ..., m)$, the n lengths and m

various angles necessary to describe the geometry.

- The elastic properties of the blade (Young's modulus E^b), and of the scratched material: Young's modulus E and Poisson's ratio ν.

- The plastic properties of the material: strength (for example the uniaxial compressive strength σ_0, and the internal friction coefficient α) and hardening (for example the hardening exponent n in the classic power-law of hardening).

- The fracture toughness of the material K_{Ic}.

- The interface friction between the blade and the material μ_i.

We seek to express our dependent variables as functions of the independent parameters:

$$F_T = f_T(d_j, \theta_k, E^b, E, nu, \sigma_0, \alpha, n, K_{Ic}, \mu_i) \tag{2.1}$$

$$F_V = f_V(d_j, \theta_k, E^b, E, nu, \sigma_0, \alpha, n, K_{Ic}, \mu_i) \tag{2.2}$$

$$A_{LB} = f_A(d_j, \theta_k, E^b, E, nu, \sigma_0, \alpha, n, K_{Ic}, \mu_i) \tag{2.3}$$

Application of the Π-theorem to (2.1) to (2.3) yields the dimensionless relations:

$$\frac{F_T}{\sigma_0 d_0^2} = \Pi_T \left(\frac{d_j}{d_0}, \theta_k, \frac{\sigma_0}{E}, \frac{\sigma_0}{E^b}, \nu, \alpha, n, \mu_i, \mathcal{I} = \frac{d_0}{(K_{Ic}/\sigma_0)^2} \right) \tag{2.4}$$

$$\frac{F_V}{\sigma_0 d_0^2} = \Pi_V \left(\frac{d_j}{d_0}, \theta_k, \frac{\sigma_0}{E}, \frac{\sigma_0}{E^b}, \nu, \alpha, n, \mu_i, \mathcal{I} = \frac{d_0}{(K_{Ic}/\sigma_0)^2} \right) \tag{2.5}$$

$$\frac{A_{LB}}{d_0^2} = \Pi_A \left(\frac{d_j}{d_0}, \theta_k, \frac{\sigma_0}{E}, \frac{\sigma_0}{E^b}, \nu, \alpha, n, \mu_i, \mathcal{I} = \frac{d_0}{(K_{Ic}/\sigma_0)^2} \right) \tag{2.6}$$

The dimensionless functions Π_T, Π_V and Π_A depend on dimensionless parameters: the geometry of the test (d_j/d_0, θ_k), the relative influence of elasticity over plasticity (σ_0/E^b,σ_0/E), other elasticity and plasticity parameters (ν, n, and α), and the relative influence of fracture over plasticity ($\mathcal{I}$). This dimensionless parameter can be written in the form $\mathcal{I} = \frac{d_0}{2\pi r_p}$ where $r_p = \frac{1}{2\pi}\left(\frac{K_{Ic}}{\sigma_0}\right)^2$ is the radius of the plastic zone, as used in ductile fracture mechanics [68]. $\mathcal{I}$ is then the ratio of a characteristic length of the

problem, d_0, to the size of the plastic zone, as opposed to the characteristic length scale of fracture phenomena. As a consequence, a great (respectively low) influence of fracture will be characterized by a large (respectively small) value of $\mathcal{I}$.
The main quantity of interest in scratch tests is the tangential hardness (1.1). Using dimensional analysis, H_S can be expressed as:

$$H_S = \sigma_0 \times \Pi \left(\frac{d_j}{d_0}, \theta_k, \frac{\sigma_0}{E}, \frac{\sigma_0}{E^b}, \nu, \alpha, n, \mu_i, \mathcal{I} = \frac{d}{(K_{Ic}/\sigma_0)^2} \right) \tag{2.7}$$

The problem thus defined can be studied from different points of view. In the following paragraphs, we propose a brief review of several approaches adopted by previous researchers in their study of the scratch test.

2.2 Main Application: Resistance to Wear

The underlying idea at the origin of the first scratch hardness classifications and test procedures was based on surface wear: the hardness of a material is determined by its ability to resist scratch. Mohs [39] and later O'Neill [42] measured the hardness by visual examination of the damage created by a scratch performed under controlled load. Today, the most common application of scratch tests is no doubt the measure of the resistance to wear of a surface. Applied to various materials like polymers (see e.g. [12] [67]), it is commonly used to measure the quality of films and coatings (see e.g. [62] [31]). Even though this fields is not a direct application for this thesis, one cannot present the scratch test without evoking its use as a measure of wear.
Surface wear of two bodies in contact is partially explained by the plowing of the softer material by small asperities of the harder material. The scratch test seems the best way to capture this process, the hard indenter playing the role of a hard asperity put in contact with the material. In the normal configuration of a wear resistance test, a very hard (diamond or carbide) indenter is drawn across the coated surface under an increasing load until some well defined failure occurs at a load which is often termed the critical load, L_C [36]. The identification of failure is key to the reliability of this

method. However, as pointed out by Bull for the testing of coatings [14], many different failure modes are observed which include coating detachment, through-thickness cracking and plastic deformation or cracking in the coating or substrate. In certain cases, some of these failure modes may even occur simultaneously. Combined with a significant effect of the test geometry [49], this makes the quantification of the quality of a coating using scratch tests not yet well defined.

This difficulty calls for the use of standardized tests, which provide an accurate comparative measure of the quality of a surface. Most recent testing procedures detect failure with three independent sensing tools: change in tangential force, acoustic emission or visual observation of the scratch groove using an advcanced optical device [28].

2.3 Scratch Test as a Means to Measure Strength Properties

Progress in indentation tests have led to an accurate characterization of classical material properties such as elasticity constants and strength, and its implementation at the nanoscale [41] [20]. Based on the same idea, scratch hardness is believed to be linked to strength properties. Here is a review of different approaches used to define this link.

2.3.1 Link Between Indentation Hardness and Scratch Hardness

In 1950, Tabor [58] showed that indentation hardness could be related to yield stress of metals by a straightforward relation $H_{indentation} = C\sigma_0$, where $C \approx 3$. Like indentation, scratch test is a measure of the resistance to penetration of a material, and hence should also to some extent be linked to the yield stress or other strength properties.

A first approach consists dividing the tangential force required to pull the indenter

in two terms [66]:

$$F_T = F_p + F_a \tag{2.8}$$

where F_p is the 'plowing' force and F_a is the 'adhesion' force. The main idea of this model is to decouple the force required to deform the material from the force due to friction between the indenter and the material. The plowing force is expected to be related to conventional indentation hardness and the adhesion term is measured by subtracting the plowing force to the global tangential force F_T. Briscoe showed [11] that the plowing hardness is actually different from the normal indentation hardness, which renders the decoupling between adhesion force and plowing force less relevant. The fundamental difference between indentation and scratch tests is the significant amount of plastic strain that occurs in the scratching direction. Models devoted to the scratch test only are hence necessary.

2.3.2 Complete Models

The first models for the scratch tests are 2D models capable of predicting the overall friction coefficient $\mu = F_T/F_V$ as a function of the shear strength k of the material and the interfacial friction between the indenter and the material. In particular, Challen and Oxley [18] [19] proposed several 2D models for the scratch of a soft material by a wedge, describing the transition from plowing, where a plastically deformed wave of material is pushed in front of the indenter, to chipping, where material is removed from the surface. This yields a relation:

$$\mu = \frac{F_T}{F_V} = \Pi(\theta, f) \tag{2.9}$$

where θ is the back-rake angle and f is the interfacial friction coefficient defined as the ratio of the interfacial shear stress to the shear strength of the material τ/k. Similar results were obtained by Komvopoulos et al. [33]. These results are based on the slip-line theory and are in good agreement with experiments carried out on metals. However, they fail to extend to conventional 3D indenters such as pyramid, cones or

spheres.

2.3.3 Upper Bound Models

Another way of tackling the problem is the use of upper bound solutions describing the flow of material around the indenter during the scratch. A series of model for a pyramidal indenter have shown good prediction of the tangential force as a function of the geometry of the indenter θ_1, the attack angle θ_2, and the friction interface f [63] [27] [1] [2]. In these models, a pyramidal indenter is dragged at constant depth d through the material and the material flows around the tip in rigid blocks. These models give a prediction of the tangential force F_T, vertical force F_V, and geometry of the flow pattern, like the height of the ridges h_r:

$$\begin{cases} F_T = \sigma_0 d^2 \times \Pi_a(\theta_1, \theta_2, f) \\ F_V = \sigma_0 d^2 \times \Pi_b(\theta_1, \theta_2, f) \\ h_r = d \times \Pi_c(\theta_1, \theta_2, f) \end{cases} \tag{2.10}$$

These results are given by the minimization of the total dissipated energy. However, the application of the upper bound to determine the geometry of the flow pattern was put into question by Azarkhin [4], on the basis of a more rigorous application of the upper bound approach that yields significantly different results on the geometry of the flow. The predictions of the tangential and vertical forces remain mostly valid.

2.3.4 Numerical Studies

The development of numerical simulation represents an opportunity to find solutions for the scratch test and investigate the influence of new parameters, such as strain hardening. In 2007, Bellemare et al. [7] developed a finite element model to predict the normal hardness, tangential hardness and pile-up height h_p observed in front of a rigid conical indenter of semiapex angle $\theta = 70.3°$ in frictional sliding on an

elastoplastic material with strain hardening:

$$\begin{cases} H_V = \sigma_0 \times \Pi_a(\theta = 70.3°, \frac{\sigma_0}{E^*}, n, \mu_i = 0.15) \\ H_T = \sigma_0 \times \Pi_b(\theta = 70.3°, \frac{\sigma_0}{E^*}, n, \mu_i = 0.15) \\ h_p = d \times \Pi_c(\theta = 70.3°, \frac{\sigma_0}{E^*}, n, \mu_i = 0.15) \end{cases} \tag{2.11}$$

where E^* is the reduced contact Young's modulus [32], n is the strain-hardening exponent, μ_i is the Amontonian friction coefficient defined as the ratio of the tangential force to the normal force of the contact, and d is the depth of scratch. They conducted a comprehensive study of the influence of elstoplasticity through the ratio E^*/σ_0 and strain hardening n. However, neither the dependence on the geometry nor the influence of the friction coefficient μ_i were studied.

A similar approach was used by Lee et al. [35] to model spherical nanoscratch tests [59], suggesting a normal scratch hardness relation of the form:

$$H_V = \sigma_0 f(E, \sigma_0) \tag{2.12}$$

The obtained relation was found to be in agreement with known experimental values and was proposed to be used as such to predict nanoscratch hardness of material with small hardening. However, the fact that (2.12) is not in a dimensionless form hints toward the unstudied influence of other parameters.

2.3.5 Scratch Tests on Rocks

All the models reviewed above are suitable for metals, thin coatings, or polymers. Recently, scratch tests have been used for rocks and cementitious materials. The ease of use of the scratch test represents a competitive argument for making it standard procedure for rock strength testing compared to classical strength measurements (see e.g. [54]). It is believed that the scratch hardness is correlated to the uniaxial compressive strength (UCS) σ_0. The model mostly used to interpret data from a scratch test on rocks was developed during the last decade by Detournay et al. [37] [50] [55], as an extension of the model of rock cutting [23]. In such tests, the indenter

is rectangular of width w, and dragged through the material at constant depth d and constant velocity V, with a back-rake angle θ. In the idealized case of a perfectly sharp cutter, the so-called *specific energy* ϵ is defined as:

$$\epsilon = \frac{F_T}{wd} \tag{2.13}$$

The specific energy is associated with the amount of energy required to cut a unit volume of rock. During experimental tests, the appearance of a wear flat on the cutter leads to the creation of a frictional surface. Using an Amontonian friction law, the term due to friction is subtracted from the measured force so as to yield the specific energy, which corresponds to the more classical definition of tangential hardness (1.1). The following empirical relation is found, based on tests on different types of rocks with an angle $\theta = 15°$, including limestones , sandstones and chalk:

$$\epsilon = C(w)\sigma_0 \ ; \ \text{with } C(w = 10\text{mm}) \approx 1.026 \tag{2.14}$$

The experimental data show that ϵ depends on w, which calls for the standardized use of a single width w in scratch tests on rocks. However, no satisfying explanation of this dependence has yet been proposed.

2.4 Focus of the Study

The brief literature review conducted in the previous section shows the tremendous diversity of scratch tests, that no complete model is able to capture. More specifically, the good correlation between scratch hardness and UCS for rocks suggests that a model applicable to cohesive-frictional materials would provide an analytical base for this empirical relation. This motivates the forthcoming development.

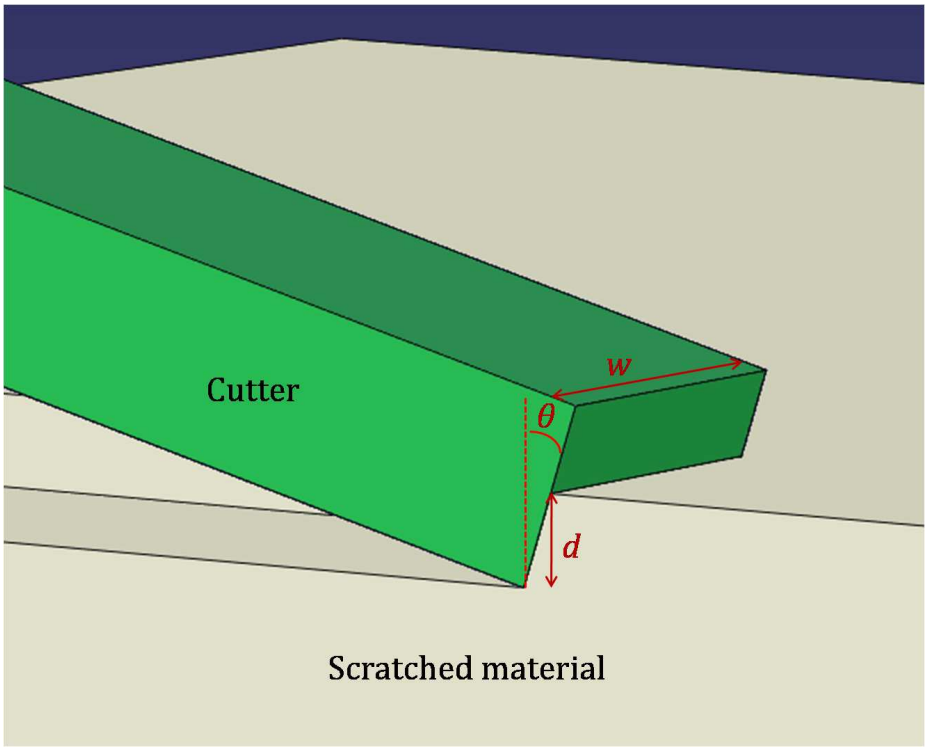

Figure 2-2: Geometry of the scratch test considered in the analysis

2.4.1 Geometry of the Test

In this thesis we consider the same scratch geometry as the one used by Detournay et al. ([37]) to test rocks and used in the oil industry to test rocks extracted from prospection fields. The rectangular blade of width w, is dragged through the tested sample at constant depth d, inclined with a back-rake angle θ (Figure 2-2), at constant velocity V. This geometry translates into a model as defined on figure 2-3. The two-dimensional model consists in an infinite half-space with a pre-existing groove of depth d. The surfaces in front of and behind the cutter are supposed stress free ($\underline{T}^d = \underline{0}$), and no-displacement kinematic boundary conditions are imposed far from the cutter $\underline{U}^d = \underline{0}$ for $|\underline{x}| \to +\infty$. The blade is pulled through the material at a horizontal velocity $\underline{V} = V\underline{e}_x$ with an inclination θ. The reaction force necessary to this displacement is $\underline{F} = F_T\underline{e}_x - F_V\underline{e}_z$, F_T and F_V being positive. Given the size of the system, gravity is neglected. Thus, no volume force is considered.

The third dimension (y-direction) is included in the model by adding a width w to the blade and the groove. The geometry is then an infinite half-space grooved

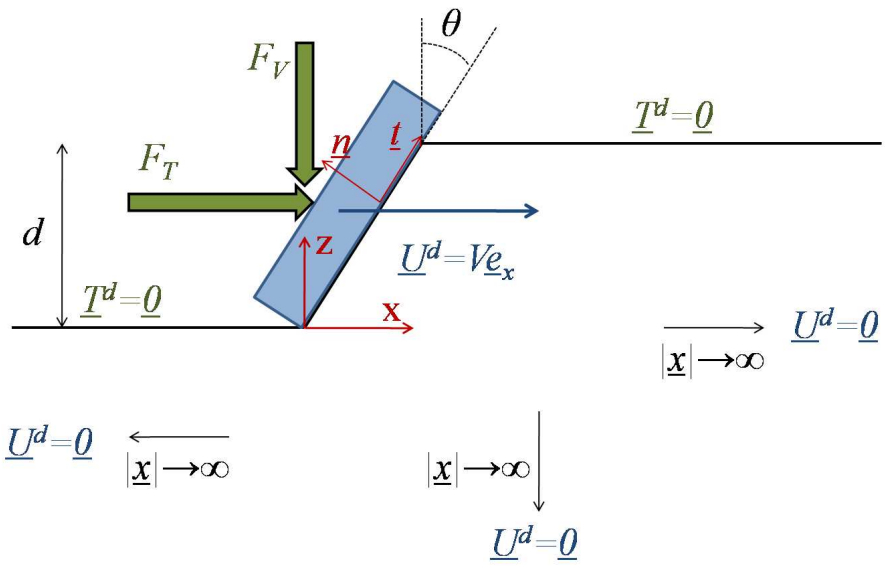

Figure 2-3: Two-dimensional model of the scratch test

between $y = -w/2$ and $y = w/2$ for $x < 0$ (Figure 2-2). The definition of the boundary conditions is a direct transposition of the 2D boundary conditions.

2.4.2 Assumptions

We now list the assumptions that are made in this thesis on which depend all the the hardness–to–strength relations found in this thesis:

- The indenter is perfectly rigid $E^b \to +\infty$, such that $\sigma_0/E^b \to 0$.
- The material is rigid ($E \to +\infty$, no more dependence on ν) and perfectly plastic ($n = 0$). According to [66], this assumption is reasonable provided that $E/\sigma_0 > 200$.
- Except for the last part of this thesis, where fracture is briefly investigated, fracture phenomena are neglected: $\mathcal{I} \to 0$.

As a consequence, the scope of this thesis is to find analytical expressions for different materials with the relationship:

$$H_S = \sigma_0 \times \Pi\left(\frac{d}{w}, \theta, \frac{\sigma_0}{E} \to 0, \frac{\sigma_0}{E^b} \to 0, \alpha, n = 0, \mu_i, \mathcal{I} \to 0\right) \tag{2.15}$$

or:

$$\boxed{H_S = \sigma_0 \times \tilde{\Pi}\left(\frac{d}{w}, \theta, \alpha, \mu_i\right)} \tag{2.16}$$

2.5 Chapter Summary

In this chapter, we showed a glimpse of various applications of the scratch test. Several rigid-plastic and elastoplatic models can be found in the literature for various types of indenters (pyramid, conical, spherical) and test configurations. The recent surge in the use of the scratch tests on rocks and its promising applications leads us to develop the first rigid-plastic model for cohesive-frictional materials scratched with rectangular indenters.

Part II

Strength Model

Chapter 3

Lower Bound Model

In this chapter we consider the scratch test using a static approach. We propose a simple stress field developed in the material in reaction to the forces applied to the blade. As stated by the lower bound theorem of yield design theory, this approach leads us to a lower bound for the tangential hardness. Purely cohesive and cohesive-frictional are considered, as well as friction on the blade–material interface. The hardness is found by solving an optimization problem. In the frictionless case, this approach yields closed form relations between hardness, geometry and strength parameters.

3.1 Theoretical Background

3.1.1 Lower Bound Limit Theorem

The underlying idea of yield design is that at plastic collapse the applied load is entirely dissipated into heat form through plastic sliding in the material bulk and along surfaces of discontinuity.
Mathematically, this is expressed by

$$\underline{Q}^{lim} \cdot \underline{q} = \int_{\Omega} \underline{\underline{\sigma}} : \underline{\underline{d}} \, d\Omega + \int_{\Gamma} \underline{T} \cdot [\![\underline{U}]\!] \, d\Gamma \tag{3.1}$$

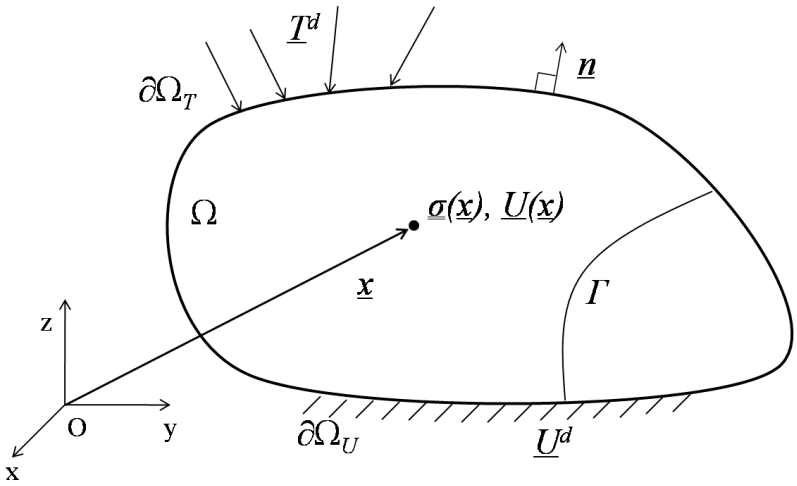

Figure 3-1: Nomenclature of the yield design framework

where $\underline{Q}^{lim}$ is the collapse load vector, $\underline{q}$ the associated velocity vector, $\underline{\underline{\sigma}}$ the statically admissible stress tensor, $\underline{\underline{d}}$ the strain rate tensor, $\underline{T} = \underline{\underline{\sigma}} \cdot \underline{n}$ the stress vector on any surface of discontinuity Γ oriented by the unit normal $\underline{n}$, and $[\![\underline{U}]\!]$ the velocity jump vector over the surfaces of discontinuity (Figure 3-1).

Limit theorems provide estimates of the actual dissipation capacity at plastic failure, as expressed by (3.1). In particular, the lower bound theorem approaches the actual dissipation capacity through stress fields, which are:

- statically admissible, i.e. in equilibrium both internally and externally with the applied load;

- plastically admissible (or strength compatible), i.e. compatible with the strength domain of the material in all the domain.

Mathematically, the set of admissible stress field $\mathcal{S}$ is expressed by

$$\mathcal{S} = \left\{ \underline{\underline{\sigma}}' \;\middle|\; \begin{array}{ll} \underline{\underline{\sigma}} \cdot \underline{n} = \underline{T}^d \text{ on } \partial\Omega_T & \text{(a)} \\ [\![\underline{T}']\!] = [\![\underline{\underline{\sigma}}']\!] \cdot \underline{n} = 0 \text{ along } \Gamma & \text{(b)} \\ \underline{\text{div}}\, \underline{\underline{\sigma}}' = \underline{0} \text{ and } \underline{\underline{\sigma}}' = \underline{\underline{\sigma}}'^T \text{ in } \Omega & \text{(c)} \end{array} \right\} \tag{3.2}$$

If we denote by $f(\underline{x}, \underline{\underline{\sigma}}'(\underline{x}))$ the scalar function representing the local strength domain, then the global strength domain $\mathcal{G}$ is defined by:

$$\mathcal{G} = \left\{ \underline{\underline{\sigma}}' \,\middle|\, f(\underline{x}, \underline{\underline{\sigma}}'(\underline{x})) \leqslant 0 \;\forall\; \underline{x} \in \Omega \right\} \tag{3.3}$$

Then it can be shown, through application of the principle of maximum work [61], that stress fields both statically admissible and strength compatible, in the sense of (3.2) and (3.3), provide a lower bound to the dissipation capacity (3.1) of the system:

$$\int_\Omega \underline{\underline{\sigma}}' : \underline{\underline{d}} \; d\Omega + \int_\Gamma \underline{T}' \cdot [\![\underline{U}]\!] \; d\Gamma \leqslant \underline{Q}^{lim} \cdot \underline{q} \;;\; \forall\; \underline{\underline{\sigma}}' \in \mathcal{S} \cap \mathcal{G} \tag{3.4}$$

This result leads to the lower bound limit theorem:

Theorem 1 *Any stress field $\underline{\underline{\sigma}}'$ which is statically admissible with the loading $\underline{Q}'$ and which is everywhere below or at yield, $\underline{\underline{\sigma}}' \in \mathcal{G}$, delivers a lower bound $\underline{Q}' \cdot \underline{q}$ to the actual dissipation rate $\underline{Q}^{lim} \cdot \underline{q}$ of the ultimate load $\underline{Q}^{lim}$ along the velocity field $\underline{q}$:*

$$\underline{Q}' \cdot \underline{q} \leqslant \underline{Q}^{lim} \cdot \underline{q} = \int_\Omega \max_{\underline{\underline{\sigma}}' \in \mathcal{S} \cap \mathcal{G}} (\underline{\underline{\sigma}}' : \underline{\underline{d}}) \; d\Omega + \int_\Gamma \max_{\underline{\underline{\sigma}}' \in \mathcal{S} \cap \mathcal{G}} (\underline{n} \cdot \underline{\underline{\sigma}}' \cdot [\![\underline{U}]\!]) \; d\Gamma \tag{3.5}$$

The lower bound theorem turns the mechanical problem into an optimization problem: maximize $\underline{Q}' \cdot \underline{q}$ through the choice of appropriate stress fields so as to approximate the actual limit load $\underline{Q}^{lim}$.

3.1.2 Material Behavior

Applying the lower bound limit theorem (3.5) requires the use of stress fields both statically and plastically compatible. Statical admissibility, as expressed in (3.2), is the continuum expression of Newton's laws of equilibrium, whose accuracy is not disputed at the scale of classical mechanical system. In contrast, strength compatibility requires the use of incomplete models to represent phenomena still misunderstood. We present in this section the law of friction used to model the blade–material interface and the strength criteria used to represent the scratched material.

Friction As stated by Rabinowicz [48], "friction is expressed in quantitative terms as a force, being the force exerted by either of two contacting bodies tending to oppose relative tangential displacement of the other one." The most commonly used model of friction comes directly from the experimental observations of the pioneers of tribology, including Amontons and Coulomb. Their findings are summarized in the following three laws:

1. The friction force F is proportional to the normal load N applied through the area of contact (Amontons 1^{st} law). The coefficient of proportionality is known as the coefficient of friction μ:
$$\mu = \frac{F}{N} \tag{3.6}$$

2. The friction force F does not depend on the apparent area of contact (Amontons 2^{nd} law).

3. The friction force F does not depend on the sliding velocity (Coulomb's law).

These three laws yield the classic Amontons-Coulomb friction law:

$$|F| \leqslant \mu N \tag{3.7}$$

This law accounts for two regimes. On the one hand, the inequality is strict for static friction, in which there is no relative displacement of the two bodies in contact. On the other hand, the inequality is saturated for kinetic friction, corresponding to sliding of the bodies against each other.

This law has been proved to be an oversimplification of the complex phenomenon of friction. First, the friction coefficient μ has different values in the static and kinetic regimes: $\mu_s > \mu_k$. The origin and nature of the static and kinetic friction coefficients have been the subject of numerous studies (e.g. [10],[57]). It has also been shown experimentally that the sliding velocity can affect the kinetic friction coefficient [47], invalidating Coulomb's law. Finally, several studies show that the friction coefficient actually depends on the normal load [10] [15], invalidating Amonton's first law.

This very brief overview of the modeling of friction illustrates the difficulty of dealing

with frictional contact problems. In fact, the most commonly admitted explanation of kinetic friction involves ploughing and abrasion phenomena which are themselves problems that can be viewed as scratch tests at the scale of the asperities of the materials in contact. A better understanding of the scratch test can hence itself help for a better modeling of friction.

Cohesive and Cohesive-Frictional Materials Cohesive materials are materials which fail when submitted to a limit shear stress that does not depend on the hydrostatic pressure. The first model proposed to encompass their behavior is attributed to Tresca in 1864 [60]. Based on an extensive series of experiments on various materials, Tresca inferred that a solid could flow like a fluid when submitted to sufficient shear, namely the *cohesion* of the material. This behavior is represented by the inequality:

$$f(\underline{T} = \underline{\underline{\sigma}} \cdot \underline{n}) = |T_t| - c \leqslant 0 \tag{3.8}$$

where $T_t = \underline{t} \cdot \underline{\underline{\sigma}} \cdot \underline{n}$ is the shear stress applied on the material surface oriented by $\underline{n}$. This criterion can also be expressed as a function of the principal stresses $\sigma_I \geqslant \sigma_{II} \geqslant \sigma_{III}$:

$$f(\underline{\underline{\sigma}}) = \sigma_I - \sigma_{III} - 2c \leqslant 0 \tag{3.9}$$

In 1913, von Mises proposed another criterion suitable for ductile materials such as metals [64], known as the von Mises criterion. Like the Tresca criterion, it predicts a failure due to limited resistance to shear of the material independent of the hydrostatic pressure. It differs from the Tresca criterion by involving the three principal stresses in its calculation of the equivalent stress:

$$f(\underline{\underline{\sigma}}) = \sigma_d - k = \sqrt{\frac{1}{6}\left((\sigma_I - \sigma_{II})^2 + (\sigma_{II} - \sigma_{III})^2 + (\sigma_{III} - \sigma_I)^2\right)} - k \leqslant 0 \tag{3.10}$$

where k is the shear strength of the material, $\sigma_d = \sqrt{\frac{1}{2}\underline{\underline{s}} : \underline{\underline{s}}}$ is the deviatoric stress, and $\underline{\underline{s}} = \underline{\underline{\sigma}} - \frac{1}{3}\mathrm{tr}(\underline{\underline{\sigma}})\,\underline{\underline{1}}$ is the deviatoric stress tensor.

A lot of materials, including most geomaterials, are pressure sensitive: their cohesion increases with the hydrostatic pressure, resulting in stronger response in compression than in tension. As a result, they cannot be satisfyingly represented by either Tresca or Von Mises criteria.

This increase of the cohesion is explained by the frictional forces that act in-between the grains of the material: an increase in the hydrostatic pressure results in an increase of the normal load governing the contact between grains. According to Amontons-Coulomb law (3.7), this, in turn, increases the maximum tangential friction force, yielding a greater cohesion for the confined material. Based on this premise, the Mohr-Coulomb criterion is expressed as surface stress criterion reading:

$$f(\underline{T} = \underline{\underline{\sigma}} \cdot \underline{n}) = |T_t| + \mu T_n - C \leqslant 0. \tag{3.11}$$

where $T_n = \underline{n} \cdot \underline{\underline{\sigma}} \cdot \underline{n}$ is the normal stress on a surface oriented by $\underline{n}$, $\mu = \tan\varphi$ is the friction coefficient, and φ the Mohr-Coulomb friction angle. In terms of principal stresses the criterion reads:

$$f(\underline{\underline{\sigma}}) = \sigma_I - \sigma_{III} + (\sigma_I + \sigma_{III})\sin\varphi - 2c\cos\varphi \leqslant 0 \tag{3.12}$$

The Mohr-Coulomb criterion is hence the frictional generalization of the Tresca criterion with a confining stress $\sigma_I + \sigma_{III}$. The Tresca criterion (3.9) is obtained by letting the friction angle φ equal 0.

The Drucker-Prager criterion [24] is a generalization of the Mohr-Coulomb criterion which involves the three principal stresses. The confinement stress is $\sigma_m = \frac{1}{3}\mathrm{tr}\ \underline{\underline{\sigma}} = \frac{1}{3}(\sigma_I + \sigma_{II} + \sigma_{III})$ and the criterion is expressed as:

$$f(\underline{\underline{\sigma}}) = \sigma_d + \alpha\sigma_m - k \leqslant 0 \tag{3.13}$$

where α is called the friction coefficient, k is the Drucker-Prager cohesion. Letting α equal 0 yields the Von Mises criterion (3.10). Given that both criteria represent the same kinds of materials, it can be useful to be able to relate them. This is done

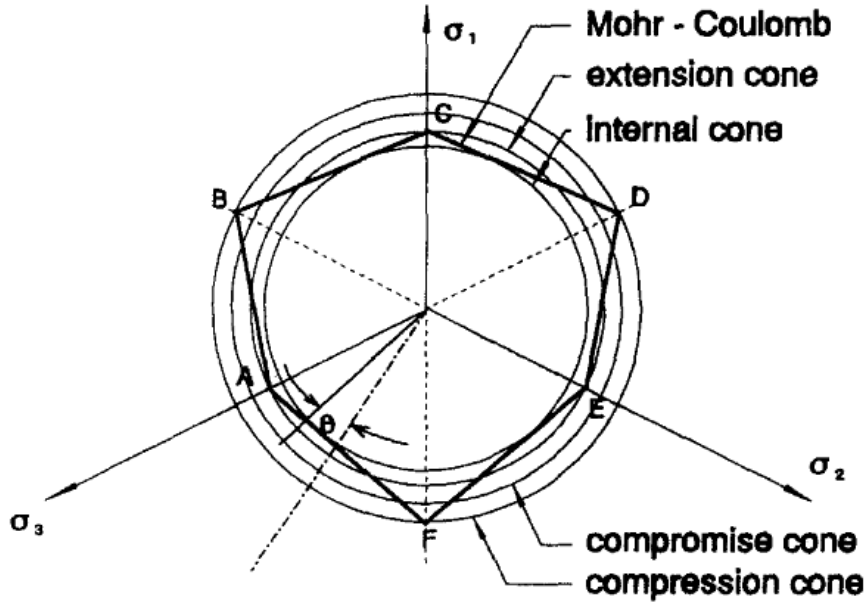

Figure 3-2: Correspondence between the Mohr-Coulomb and the Drucker-Prager criterion in the deviatoric stress plane (from [56]).

by projecting the Drucker-Prager strength function on the deviatoric stress plane, defined in the principal stresses space by $\sigma_I + \sigma_{II} + \sigma_{III} = 0$. In this plane, the Drucker-Prager criterion can be considered as a Mohr-Coulomb criterion by using relations linking Drucker-Prager coefficients (k,α) to Mohr-Coulomb parameters (c,φ) [56]. As shown on figure 3-2, several choices are possible. Among them are found the ones yielding the greatest (internal cone) and the smallest (compression cone) Mohr-Coulomb cohesions for a given couple (k, α):

$$\begin{array}{lll} \text{Compression Cone} & c = \frac{3-\sin\varphi}{2\sqrt{3}\cos\varphi}k & \sin\varphi = \frac{3\alpha}{\alpha+2\sqrt{3}} \\ \text{Internal Cone} & c = \sqrt{\frac{3+\sin^2\varphi}{3\cos^2\varphi}} & \sin\varphi = \sqrt{\frac{3\alpha^2}{3-\alpha^2}} \end{array} \tag{3.14}$$

It is important to note that there is a limitation in the choice of the friction coefficient α [22]:

$$\alpha < \sqrt{\frac{3}{4}} \tag{3.15}$$

Indeed, this value corresponds to a friction angle of $\varphi = 90°$ for the 'internal cone'

Criterion	$f(\underline{\underline{\sigma}})$
Tresca	$\sigma_I - \sigma_{III} - 2c$
Von Mises	$\sqrt{\frac{1}{6}\left((\sigma_I - \sigma_{II})^2 + (\sigma_{II} - \sigma_{III})^2 + (\sigma_{III} - \sigma_I)^2\right)} - k$
Mohr-Coulomb	$\sigma_I(1 + \sin\varphi) - \sigma_{III}(1 - \sin\varphi) - 2c\cos\varphi$
Drucker-Prager	$\sqrt{\frac{1}{6}\left((\sigma_I - \sigma_{II})^2 + (\sigma_{II} - \sigma_{III})^2 + (\sigma_{III} - \sigma_I)^2\right)} + \frac{\alpha}{3}\left(\sigma_I + \sigma_{II} + \sigma_{III}\right) - k$

Table 3.1: Definition of the strength criteria. c is the cohesion; k is the shear strength; φ is the internal friction angle; α is the internal friction coefficient.

Criterion	σ_0
Tresca	$2c$
Von Mises	$\sqrt{3}k$
Mohr-Coulomb	$\frac{2c\cos\varphi}{1-\sin\varphi}$
Drucker-Prager	$\frac{\sqrt{3}k}{1-\alpha/\sqrt{3}}$

Table 3.2: Uniaxial compressive strength σ_0 for the classic strength criteria. c is the cohesion; k is the shear strength; φ is the internal friction angle; α is the internal friction coefficient.

correspondence of the Mohr-Coulomb criterion (3.14).

Table 3.1 summarizes the four strength criteria considered in this chapter. From a practical point of view, the uniaxial compressive strength (UCS) σ_0 is commonly used as a measure for the strength of geomaterials due to the simplicity of its experimental measurement and its model-independence. It can be linked to the material parameters (c, k, φ, α) by considering the case $(\sigma_I = \sigma_{II} = 0, \sigma_{III} = -\sigma_0)$ in the strength functions $f(\underline{\underline{\sigma}})$. The correspondence for each material is listed in Table 3.2.

3.2 Application of the Lower Bound Theorem to the Scratch Test

3.2.1 Formulation of the Plastic Work Rate

Consider the problem of the scratch test defined in chapter 2 (Figure 2-2): a rigid blade of width w is pulled through the material at a velocity $\underline{V} = V\underline{e}_x$ at constant depth d, inclined with an angle θ w.r.t. $\underline{e}_z$. The loading associated with the velocity

$\underline{V}$ is the force imposed by the blade on the material $\underline{F} = F_T \underline{e}_x - F_V \underline{e}_z$. All the other boundaries have either zero-velocity or stress-free conditions. As a result the plastic dissipation rate is given by:

$$\underline{Q}^{lim} \cdot \underline{q} = \underline{F} \cdot \underline{V} = F_T^{lim} V \tag{3.16}$$

The material is considered rigid perfectly plastic. Therefore the contact area between the blade and the material is known and its horizontal projection is wd. Using definition (1.1) of the hardness, we find that $F_T^{lim} = H_T^{lim} wd$, which yields the dissipation rate as a function of the limit hardness H_T:

$$\underline{Q}^{lim} \cdot \underline{q} = H_T^{lim} wdV \tag{3.17}$$

3.2.2 Application of the Lower Bound Theorem

Let us denote $H_T(\underline{\underline{\sigma}}')$ the tangential hardness yielded by any stress field $\underline{\underline{\sigma}}'$. Inserting relation (3.17) into the lower bound theorem (3.5) and dividing the result by the positive constant (i.e. independent of $\underline{\underline{\sigma}}'$) term wdV yields:

$$\boxed{H'_T(\underline{\underline{\sigma}}') \leqslant H_T^{lim} \quad \forall\, \underline{\underline{\sigma}}' \in \mathcal{S} \cap \mathcal{G}} \tag{3.18}$$

This fundamental inequality constitutes the basis of the lower bound approach. Any stress field both statically and plastically admissible yields a tangential hardness H_T smaller than the actual hardness of the material H_T^{lim}. The application of the theorem naturally calls for the following step-by-step procedure:

1. Propose a family of stress fields with limited degrees of freedom;
2. Apply the conditions for statical admissibility;
3. Apply the conditions for strength compatibility;
4. Obtain the best lower bound reachable with the chosen family of stress fields by maximizing the hardness H_T with respect to the remaining degrees of freedom.

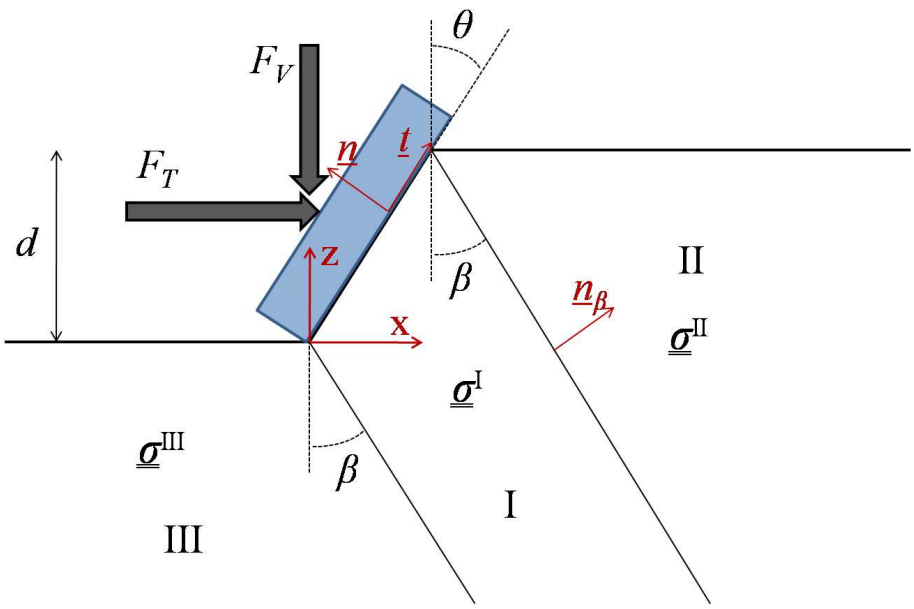

Figure 3-3: Geometry of the 2D model of the scratch test.

It is worthwhile to note that, in accordance with the notion of plastic collapse, that is an uncontrolled indefinite yield, the scratch velocity V appears as a dummy parameter of the problem.

3.3 Development of the Lower Bound Model

3.3.1 Family of Stress Fields

For purpose of analysis, consider the scratch plane in the (xz) plane divided in three zones (Fig. 3-3) delimited by straight lines inclined w.r.t. the z axis by an angle β. For these three zones, consider piecewise constant diagonal stress fields enriched by a shear stress $\tau = \sigma_{xz}$:

$$\underline{\underline{\sigma}}^J = \sigma_x^J \underline{e}_x \otimes \underline{e}_x + \sigma_y^J \underline{e}_y \otimes \underline{e}_y + \sigma_z^J \underline{e}_z \otimes \underline{e}_z + \tau^J \left(\underline{e}_x \otimes \underline{e}_z + \underline{e}_z \otimes \underline{e}_x\right);\ J = I, II, III \quad (3.19)$$

This defines a subspace of stress fields of dimension 12 (4 variables per zone). It is worthwhile to note that the shape of the stress field is chosen in accordance with the plane strain rate assumption, which is suitable to infinitely wide scratch test in the

y-direction.

3.3.2 Statical Admissibility

We first tackle the statical admissibility of $\underline{\underline{\sigma}}'$ of the shape described in (3.19). First, it is immediate to check that the local equilibrium (3.2c) is satisfied by these symmetric piecewise-constant stress fields. As a consequence, the statical admissibility is only restricted by the boundary conditions on $\partial\Omega_I$, $\partial\Omega_{II}$, and $\partial\Omega_{III}$, and the interface conditions on Γ_{I-II} and Γ_{II-III}.

$$\text{on } \partial\Omega_I \quad : \quad \underline{\underline{\sigma}}^I \cdot \underline{n} = H_T \cos\theta \underline{e}_x - H_V \sin\theta \underline{e}_z \tag{3.20}$$

$$\Leftrightarrow \quad \begin{cases} \tau \tan\theta - \sigma_x = H_T & (a) \\ \\ \tau \cot\theta - \sigma_z = H_V & (b) \end{cases} \tag{3.21}$$

$$\text{on } \partial\Omega_J; J = II, III \quad : \quad \underline{\underline{\sigma}}^J \cdot \underline{e}_z = 0 \Leftrightarrow \underline{\underline{\sigma}}^J = \left(\sigma_x^J e_x \otimes e_x + \sigma_y^J e_y \otimes e_y\right) \tag{3.22}$$

$$\text{on } \Gamma_{I-J}; J = II, III \quad : \quad \underline{\underline{\sigma}}^I \cdot \underline{n}_\beta = \underline{\underline{\sigma}}^J \cdot \underline{n}_\beta \tag{3.23}$$

$$\Leftrightarrow \quad \begin{cases} \sigma_z \tan\beta = -\tau & (a) \\ \\ \sigma_x^J = \sigma_x - \dfrac{\tau^2}{\sigma_z} & (b) \end{cases} \tag{3.24}$$

where $\underline{n} = -\cos\theta\ \underline{e}_x + \sin\theta\ \underline{e}_z$ is the (outward) normal to the scratch blade–material interface $\partial\Omega_I$; $H_T = F_T/(wd)$ and $H_V = F_V/(wd\tan\theta)$ are the average force components acting per projected contact area on $\partial\Omega_I$; $\underline{n}_\beta = \cos\beta\ \underline{e}_x + \sin\beta\ \underline{e}_z$ is the normal at the interfaces Γ_{I-II} and Γ_{I-III} between the three domains. Let us notice that the same boundary and interface conditions apply on $\underline{\underline{\sigma}}^{II}$ and $\underline{\underline{\sigma}}^{III}$. Given the same material in both zones, the strength compatibility conditions must also be the same. As a consequence, $\underline{\underline{\sigma}}^{II} = \underline{\underline{\sigma}}^{III}$. From now on we do not distinguish them, using for both the same superscript II, whereas we omit the superscript I for the stress components of $\underline{\underline{\sigma}}^I$.

The angle β, which serves as one degree of freedom in the optimization problem,

is geometrically restricted to $-\beta < \theta$ which is equivalent in our range of angles to $-\tan(\beta) < \tan(\theta)$. In the light of relation (3.24a), this implies:

$$\frac{\tau}{\sigma_z} - \tan(\theta) < 0 \tag{3.25}$$

The subset of statically admissible stress fields $\mathcal{S}$ described by (3.2) is then reduced to five stress unknowns $\left(\sigma_x, \sigma_y, \sigma_z, \tau, \sigma_y^{II}\right)$ linked together by equations (3.21) and (3.24), and constrained by (3.25).

3.3.3 Strength Compatibility

The set of strength compatible stress fields $\mathcal{G}$ includes both the strength behavior of the scratched material and the frictional nature of the scratch blade–material interface. The strength behavior of the material is represented by scalar strength functions $f(\underline{\underline{\sigma}}) \leqslant 0$ (Table 3.1). The strength compatibility condition imposed by the material plastic law reads:

$$f(\underline{\underline{\sigma}}^J) \leqslant 0; J = I, II \tag{3.26}$$

Denoting by $\sigma_t = \underline{t} \cdot \underline{\underline{\sigma}}^I \cdot \underline{n}$ and $\sigma_n = \underline{n} \cdot \underline{\underline{\sigma}}^I \cdot \underline{n}$ the tangential and normal stress components of the stress vector at the blade–material interface, Amontons-Coulomb law of friction (3.7)reads:

$$|\sigma_t| + \mu_i \sigma_n \leqslant 0 \tag{3.27}$$

with $\sigma_n \leqslant 0$, which ensures contact between the blade and the material. Note that this condition is included in (3.27) provided that $\mu_i \neq 0$. Using the relationships (3.21) and (3.24) derived from statical admissibility, we find the expressions of these stress components at the interface:

$$\sigma_t = \underline{t} \cdot \underline{\underline{\sigma}}^I \cdot \underline{n} = (\sigma_z - \sigma_x) \sin\theta \cos\theta + \tau \left(\sin^2\theta - \cos^2\theta\right) = \cos\theta \sin\theta \left(H_T - H_V\right) \tag{3.28a}$$

$$\sigma_n = \underline{n} \cdot \underline{\underline{\sigma}}^I \cdot \underline{n} = \sigma_x \cos^2\theta + \sigma_z \sin^2\theta - 2 \sin\theta \cos\theta \, \tau = -\cos^2\theta H_T - \sin^2\theta H_V \leqslant 0 \tag{3.28b}$$

These inequalities, in combination with the strength of the material, give the expression of the set of strength compatibility:

$$\mathcal{G} = \left\{ \underline{\underline{\sigma}}^J \;\middle|\; \begin{array}{c} f(\underline{\underline{\sigma}}^J) \leqslant 0 \\ 2\sin\theta\cos\theta\,\tau - \left(\sigma_x \cos^2\theta + \sigma_z \sin^2\theta\right) \leqslant 0 \\ \left|(\sigma_z - \sigma_x)\sin\theta\cos\theta + \tau\left(\sin^2\theta - \cos^2\theta\right)\right| \leqslant \mu_i \left(2\sin\theta\cos\theta\,\tau - \left(\sigma_x \cos^2\theta + \sigma_z \sin^2\theta\right)\right) \end{array} \right\} \tag{3.29}$$

or equivalently:

$$\mathcal{G} = \left\{ \underline{\underline{\sigma}}^J \;\middle|\; \begin{array}{c} f(\underline{\underline{\sigma}}^J) \leqslant 0 \\ \cos^2\theta H_T + \sin^2\theta H_V \leqslant 0 \\ \left|\cos\theta\sin\theta\,(H_T - H_V)\right| \leqslant \mu_i \left(\cos^2\theta H_T + \sin^2\theta H_V\right) \end{array} \right\} \tag{3.30}$$

3.3.4 Lower Bound Optimization Problem

A combination of relations (3.20) to (3.30) leads to the following expression of the lower bound optimization problem:

$$H_S = H_T^{lim} \;\geqslant\; H_T^{opt} = \sup\left\{\tau\tan\theta - \sigma_x | (\sigma_x, \sigma_y, \sigma_z, \tau, \sigma_y^{II}) \in \mathbb{R}^5\right\} \tag{3.31}$$

$$s.t. \left\{ \begin{array}{ll} \dfrac{\tau}{\sigma_z} - \tan\theta < 0 & (a) \\ \sigma_n \leqslant 0 & (b) \\ |\sigma_t| + \mu_i \sigma_n \leqslant 0 & (c) \\ f\left(\underline{\underline{\sigma}}^I\right) \leqslant 0 & (d) \\ f\left(\underline{\underline{\sigma}}^{II}\right) \leqslant 0 & (e) \end{array} \right. \tag{3.32}$$

As stated previously, condition (3.32b) is included in (3.32c) in the case of a non-zero friction coefficient. However it is necessary to consider it in the frictionless case, $\mu_i = 0$, to ensure the contact between the blade and the material.

While derived here for a scratch test in the (xz) plane, and thus for an unspecified scratch width, the previous set of equations also holds for scratch tests of finite width w with orthogonal frictionless boundaries. Indeed, it suffices to consider diagonal

stress fields in adjacent material domains of the form (3.19). As a consequence, this lower bound model does not show any dependence of the hardness on the depth–to–width ratio d/w.

3.4 Analytical Solutions for Frictionless Contact

The optimization problem thus defined can be easily solved with appropriate optimization software. For some simple reference yield surfaces, closed form solutions can be derived, which is the focus of this Section. Throughout this section we will assume frictionless interface conditions ($\mu_i = 0$), so that, using (3.28), $H_T = H_V$ and:

$$\text{on } \partial\Omega_I : \underline{\underline{\sigma}}^I \cdot \underline{n} = \sigma_n \underline{n} = -H_T \underline{n} \tag{3.33}$$

In this case, the eigenvectors of $\underline{\underline{\sigma}}^I$ are oriented by $\underline{n}$, $\underline{t}$, and $\underline{e}_y$:

$$\underline{\underline{\sigma}}^I = \sigma_1 \underline{t} \otimes \underline{t} + \sigma_2 \underline{e}_y \otimes \underline{e}_y - H_T \underline{n} \otimes \underline{n} \tag{3.34}$$

where $\sigma_1 = \underline{t} \cdot \underline{\underline{\sigma}}^I \cdot \underline{t}$, $\sigma_2 = \underline{e}_y \cdot \underline{\underline{\sigma}}^I \cdot \underline{e}_y$, and $\sigma_3 = \underline{n} \cdot \underline{\underline{\sigma}}^I \cdot \underline{n} = -H_T$ are principal stresses. The principal stress σ_1 can be derived from the interface condition $\underline{\underline{\sigma}}^I \cdot \underline{n}_\beta = \underline{\underline{\sigma}}^{II} \cdot \underline{n}_\beta$ with $\underline{n}_\beta = \sin(\theta + \beta)\underline{t} - \cos(\theta + \beta)\underline{n}$. In the $(\underline{n}, \underline{t})$ base, the interface condition reads:

$$\sigma_1 \sin(\theta + \beta)\underline{t} - \sigma_3 \cos(\theta + \beta)\underline{n} = \sigma_x^{II} (\underline{e}_x \cdot \underline{n}_\beta)\underline{e}_x \tag{3.35}$$

Projecting this equality on vectors $\underline{e}_x$ and $\underline{e}_z$ yields the following scalar equations:

$$\sigma_1 \sin(\theta + \beta) \sin\theta + \sigma_3 \cos(\theta + \beta) \cos\theta = \sigma_x^{II} \cos\beta \tag{3.36}$$

$$\sigma_1 \sin(\theta + \beta) \cos\theta - \sigma_3 \cos(\theta + \beta) \sin\theta = 0 \tag{3.37}$$

This yields:

$$\sigma_1 = -H_T \frac{\tan\theta}{\tan(\theta + \beta)} \tag{3.38}$$

while:

$$\sigma_x^{II} = -H_T\,(1 - \tan\theta \tan\beta) \tag{3.39}$$

These relations largely simplify the derivation of analytical solutions for some simple yield criteria, reducing the optimization problem to two stress unknowns, $\sigma_2 = \sigma_y^I$ and σ_y^{II}, in addition to angle β. Ordering the principal stresses according to $\sigma_I \geqslant \sigma_{II} \geqslant \sigma_{III}$ yields:

	σ_I	$\geqslant \sigma_{II} \geqslant$	σ_{III}
Zone I:	$\sigma_1 = -H_T \dfrac{\tan\theta}{\tan(\theta+\beta)}$	$\sigma_y^I \in [\sigma_I, \sigma_{III}]$	$\sigma_3 = -H_T$
Zone II:	$\sigma_z^{II} = 0$	$\sigma_y^{II} \in [\sigma_I, \sigma_{III}]$	$\sigma_x^{II} = -H_T\,(1 - \tan\theta\tan\beta)$

(3.40)

3.4.1 Cohesive Materials: Tresca and Von-Mises

We start by considering purely cohesive materials, as expressed by the Tresca and Von Mises strength criteria defined in Table 3.1. Consider first the Tresca case. The use of the principal stresses (3.40) in the strength criterion $f(\underline{\sigma}) = \sigma_I - \sigma_{III} - 2c \leqslant 0$ yields:

$$H_T = 2c \max_{\beta} \begin{cases} \left(1 - \dfrac{\tan\theta}{\tan(\theta+\beta)}\right)^{-1} & \text{Zone I} \\ \\ \dfrac{1}{1 - \tan\theta\tan\beta} & \text{Zone II} \end{cases} \tag{3.41}$$

The solution of the optimization problem is achieved for $f(\underline{\underline{\sigma}}^I) = f(\underline{\underline{\sigma}}^{II}) = 0$, which entails[1]:

$$\boxed{H_S \geqslant \max_\beta H_T = 2c\,(1+\sin\theta)};\ \text{with:}\ \beta = \frac{\pi}{4} - \frac{\theta}{2} \tag{3.42}$$

Consider next the Von-Mises case, which distinguishes itself from the Tresca material through the contribution of the intermediate principal stress σ_{II} in yield function (Table 3.1). Thus, the optimization must include σ_{II}, in addition to angle β. It is readily understood that the best σ_{II} is the one that minimizes the strength function $f(\underline{\underline{\sigma}}^J)$ for given values of σ_I and σ_{III}:

$$\left.\frac{\partial f}{\partial \sigma_{II}}\right|_{\sigma_I,\sigma_{III}} = 0 \Leftrightarrow \sigma_{II} = \frac{1}{2}(\sigma_I + \sigma_{III}) \tag{3.43}$$

Introducing this optimal value into the function reduces the Von-Mises criterion to a Tresca form:

$$f(\sigma_I^J \geqslant \sigma_{II} = \frac{1}{2}\left(\sigma_I^J + \sigma_{III}^J\right) \geqslant \sigma_{III}^J) = \left|\sigma_I^J - \sigma_{III}^J\right| - 2k \leqslant 0 \tag{3.44}$$

It follows that solution (3.42) remains valid for the Von-Mises criterion provided one replaces the Tresca cohesion c by the Von-Mises shear strength k. It should be noted, however, that due to the difference in uniaxial strength–cohesion relationship of the two criteria, displayed in Table 3.2, the scratch hardness–to–yield strength relations

---

[1]

$$f(\underline{\underline{\sigma}}^I) = f(\underline{\underline{\sigma}}^{II}) \Leftrightarrow \frac{\tan(\theta+\beta)}{\tan(\theta+\beta)-\tan\theta} = \frac{1}{1-\tan\theta\tan\beta}$$

$$\Leftrightarrow \tan\beta = \frac{1-\sin\theta}{\cos\theta}\ \text{using}\ \tan(\theta+\beta) = \frac{\tan\theta+\tan\beta}{1-\tan\theta\tan\beta}$$

Given that $\cos\theta = \frac{1-u^2}{1+u^2}$ and $\sin\theta = \frac{2u}{1+u^2}$ with $u = \tan\frac{\theta}{2}$, we find:

$$\tan\beta = \frac{1-u}{1+u} = \frac{\tan\frac{\pi}{4} - \tan\frac{\theta}{2}}{1+\tan\frac{\pi}{4}\tan\frac{\theta}{2}} = \tan\left(\frac{\pi}{4} - \frac{\theta}{2}\right)$$

differ:

$$\frac{H_S}{\sigma_0} \geqslant \frac{H_T}{\sigma_0} = (1+\sin\theta)\begin{cases} 1 & \text{Tresca } (\sigma_0 = 2c) \\ \dfrac{2}{\sqrt{3}} & \text{Von-Mises } \left(\sigma_0 = \sqrt{3}k\right) \end{cases} \tag{3.45}$$

3.4.2 Cohesive–Frictional Materials: Mohr-Coulomb and Drucker-Prager

Pressure sensitive materials are best represented with the Mohr-Coulomb and Drucker-Prager criteria, whose expressions are given in Table 3.1. Following the same procedure as developed for the Tresca and Von-Mises case, we arrive at the following hardness–cohesion–friction relationships:

- For the Mohr-Coulomb material:

$$\boxed{H_S \geqslant \max_\beta H_T = 2c\frac{\cos\varphi\left(1-\sin^2\theta\right)}{1-\sin\theta\cos\varphi\sqrt{1+(\tan\varphi\sin\theta)^2}-\sin\varphi\cos^2\theta}} \tag{3.46}$$

  with:

$$\tan\beta = \frac{\sqrt{1+\tan^2\theta-\sin^2\varphi}-\tan\theta}{1-\sin\varphi} \tag{3.47}$$

- For the Drucker-Prager material, using $\sigma_{II} = \frac{1}{2}(\sigma_I+\sigma_{III}) - \frac{\alpha}{2\sqrt{1-\alpha^2/3}}(\sigma_I-\sigma_{III})$:

$$\boxed{H_S \geqslant \max_\beta H_T = 2k\frac{1-\sin^2\theta}{\sqrt{1-\frac{\alpha^2}{3}}-\sin\theta\sqrt{1-\alpha^2\left(\frac{1}{3}+\cos^2\theta\right)}-\alpha\cos^2\theta}} \tag{3.48}$$

  with:

$$\tan\beta = \frac{\sin\theta\sqrt{1-\frac{\alpha^2}{3}}-\sqrt{1-\alpha^2\left(\frac{1}{3}+\cos^2\theta\right)}}{\left(\alpha-\sqrt{1-\frac{\alpha^2}{3}}\right)\cos\theta} \tag{3.49}$$

It is straightforward to verify that (3.46) and (3.48) reduce to (3.42) for the frictionless case ($\varphi = 0$ and $\alpha = 0$). Using the correspondence between σ_0 and (c,φ) or (k,α), we can formulate the hardness–to–UCS ratio of frictional cohesive materials

in the Mohr-Coulomb and Drucker-Prager cases:

$$\boxed{H_S \geqslant H_T = \sigma_0 \frac{\left(1-\sin^2\theta\right)(1-\sin\varphi)}{1-\sin\theta\cos\varphi\sqrt{1+(\tan\varphi\sin\theta)^2}-\sin\varphi\cos^2\theta}} \tag{3.50}$$

$$\boxed{H_S \geqslant H_T = \sigma_0 \frac{2}{\sqrt{3}} \frac{\left(1-\sin^2\theta\right)\left(1-\alpha/\sqrt{3}\right)}{\sqrt{1-\frac{\alpha^2}{3}}-\sin\theta\sqrt{1-\alpha^2\left(\frac{1}{3}+\cos^2\theta\right)}-\alpha\cos^2\theta}} \tag{3.51}$$

From these relations we can draw two conclusions: first, there is no direct correlation between tangential hardness and either cohesion or UCS. Instead, a dependence on the internal friction of the material appears in the hardness–to–strength relations. Secondly, no equivalence between the Mohr-Coulomb and Drucker-Prager formulas can be found, i.e. no general relation between (c, φ) and (k, α), as expressed for example in (3.14), leads to a common expression of H_T/σ_0.

3.5 Consideration of Interface Friction

Frictionless contact implies that:

$$\frac{F_V}{F_H} = \tan\theta \Longleftrightarrow \frac{H_T}{H_V} = 1 \tag{3.52}$$

where we recall that $H_T = F_T/(wd)$ and $H_V = F_V/(wd\tan\theta)$ represent the mean pressures generated by the scratch force and the vertical force over the respective load bearing areas. When H_T/H_V departs from unity, the presence of interface friction needs to be considered; for instance, in the form of Amontons-Coulomb law of friction (3.27):

$$|\sigma_t| + \mu_i\sigma_n \leqslant 0 \tag{3.53}$$

We recall that inequality (3.53) is saturated when there is sliding between the material and the blade and is strict when no relative movement occurs (adhesion of the material to the blade). Taking the frictionless configuration as a reference, we model the effect of (Amontonian) friction as an additional degree of freedom θ', as depicted on figure 3-4, which represents the rotation of the principal directions of the stress tensor in

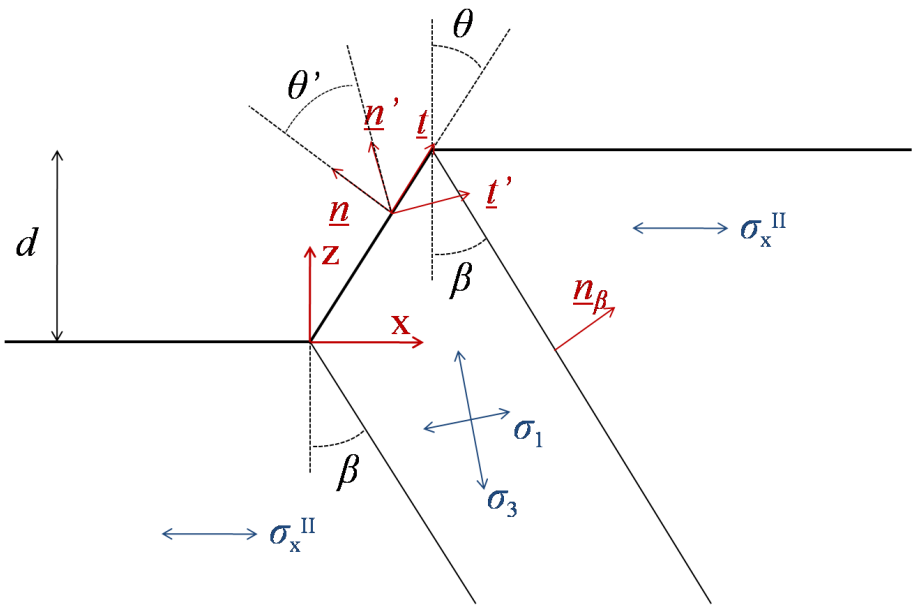

Figure 3-4: Geometry and stress fields in the frictional case

zone I. The eigenvectors of $\underline{\underline{\sigma}}^I$ are oriented by $\underline{n}'$, $\underline{t}'$, and $\underline{e}_y$:

$$\underline{\underline{\sigma}}^I = \sigma_1 \underline{t}' \otimes \underline{t}' + \sigma_2 \underline{e}_y \otimes \underline{e}_y - \sigma_3 \underline{n}' \otimes \underline{n}' \tag{3.54}$$

The boundary condition on $\partial\Omega_I$ gives a first relation between the principal stresses σ_1 and σ_3 and the tangential hardness H_T:

$$H_T = \sigma_1 \sin^2\theta' - \sigma_3 \cos^2\theta' - \tan\theta \cos\theta' \sin\theta' \,(\sigma_1 - \sigma_3) \tag{3.55}$$

The interface condition $\underline{\underline{\sigma}}^I \cdot \underline{n}_\beta = \underline{\underline{\sigma}}^{II} \cdot \underline{n}_\beta$ (with $\underline{n}_\beta = \sin(\theta+\theta'+\beta)\underline{t}' - \cos(\theta+\theta'+\beta)\underline{n}'$) yields:

$$\sigma_3 = \sigma_1 \frac{\tan(\theta + \theta' + \beta)}{\tan(\theta + \theta')} \tag{3.56}$$

and:

$$\sigma_1 \sin(\theta + \theta' + \beta) \sin(\theta + \theta') + \sigma_3 \cos(\theta + \theta' + \beta) \cos(\theta + \theta') = \sigma_x^{II} \cos\beta \tag{3.57}$$

Combining equations (3.55) and (3.56) gives the principal stresses σ_1 and σ_3 as functions of H_T,θ,θ', and β:

$$\sigma_1 = -H_T \frac{\tan(\theta+\theta')}{\cos^2\theta' \tan(\theta+\theta'+\beta) - \sin^2\theta' - \tan\theta\cos\theta'\sin\theta'(\tan(\theta+\theta'+\beta) - \tan(\theta+\theta')} \tag{3.58}$$

$$\sigma_3 = -H_T \frac{\tan(\theta+\theta'+\beta)}{\cos^2\theta' \tan(\theta+\theta'+\beta) - \sin^2\theta' - \tan\theta\cos\theta'\sin\theta'(\tan(\theta+\theta'+\beta) - \tan(\theta+\theta')} \tag{3.59}$$

3.5.1 Cohesive Materials With Interface Friction

To illustrate the effect of friction, consider first the cohesive material case described by the Tresca or Von Mises criteria (Table 3.1). The solution of the optimization problem is achieved for $f(\underline{\underline{\sigma}}^I) = f(\underline{\underline{\sigma}}^{II}) = 0$, which entails for the Tresca criterion:

$$H_T = 2c\left(\sin(\theta+\theta') + \frac{\cos\theta'\cos(\theta+\theta')}{\cos\theta}\right) \text{ with: } \beta = \frac{\pi}{4} - \frac{\theta+\theta'}{2} \tag{3.60}$$

This expression remains valid for the Von Mises criterion provided one replaces the Tresca cohesion c by the Von Mises shear strength k. The goal is now to find the optimum value of the θ' angle, which yields the highest scratch hardness value. This angle is constrained by the friction at the interface between the blade and the sample. Using the value of β as set forth by (3.60), we can define a set of admissible values for θ' that depends on the back-rake angle θ and interface friction coefficient μ_i:

$$\mathcal{T}(\theta,\mu_i) = \left\{\theta' \left| \left|\frac{\tan\theta'}{\sin(\theta+\theta')}\right| - \mu_i\left(\frac{1}{\cos^2\theta'} + \frac{1}{\sin(\theta+\theta')}\right) \leqslant 0\right.\right\} \tag{3.61}$$

The following non-linear optimization problem for purely cohesive materials thus needs to be solved:

$$H_S \geqslant \max_{\theta'\in\mathcal{T}} H_T = 2c\left(\sin(\theta+\theta') + \frac{\cos\theta'\cos(\theta+\theta')}{\cos\theta}\right) \tag{3.62}$$

The high non-linearity of the function makes it difficult to find an analytical solution for (3.62), and calls for the use of numerical solutions. Figure 3-5 shows the depen-

dence of H_T on θ' for three different values of the back-rake angle θ.For each value of θ, there exists an optimum value θ'_{opt} for θ' that maximizes the hardness H_T in the sense of the lower-bound optimization problem (3.62). Furthermore, we identify a critical angle $\sin\theta_{cr} = \left(\sqrt{5}-1\right)/2$ (i.e. $\theta_{cr} \approx 38.17°$) that separates two domains: for $\theta < \theta_{cr}$, a positive value $\theta' > 0$ is required to increase the hardness to its maximum value; for $\theta > \theta_{cr}$ the inverse holds. At $\theta = \theta_{cr}$ the effect of interface friction on the scratch hardness annihilates: the maximum value of the hardness is obtained with $\theta' = 0$, which corresponds to the frictionless case $\sigma_t = 0$.

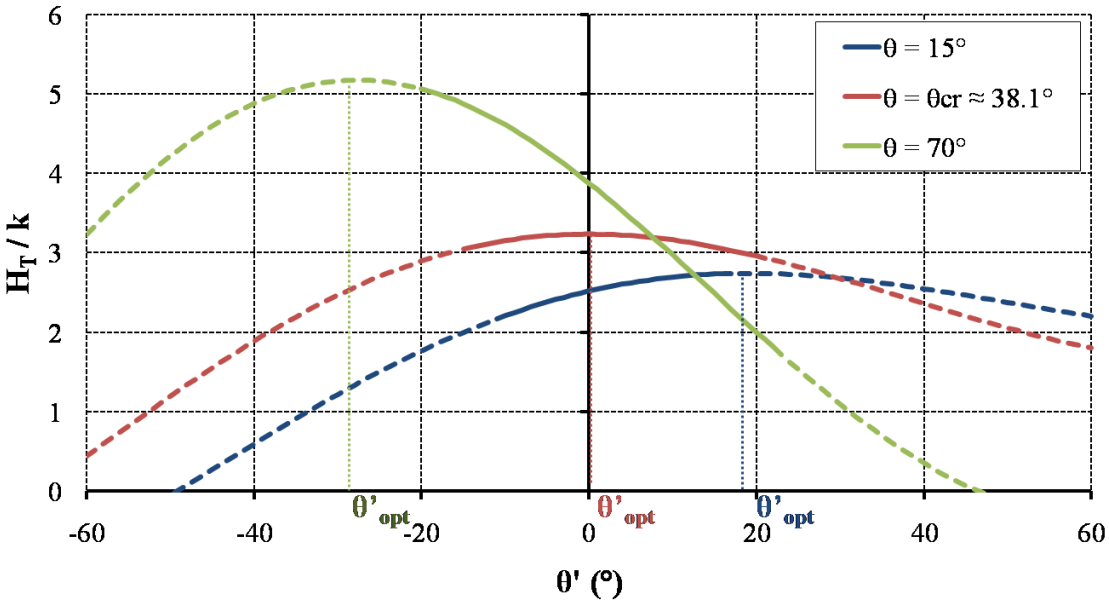

Figure 3-5: Effect of interface friction on scratch hardness: H_T/k vs. θ' for a cohesive material. The line is solid (respectively dashed) for values of θ' compatible (respectively not compatible) with the friction law for $\mu_i = 0.2$.

On the other hand, the optimum angle θ'_{opt} must lie within the set of admissible angles $\mathcal{T}(\theta, \mu_i)$ as defined by (3.60), and depicted in figure 3-6 for different values of friction coefficient μ_i. The analysis suggests the existence of a critical friction coefficient $\mu_i^{crit} = \mu_i^{crit}(\theta)$ for a given back-rake angle θ: for $\mu_i < \mu_i^{crit}(\theta)$, the friction condition is saturated, i.e. $|\sigma_t| + \mu_i\sigma_n = 0$; while $\theta'_{opt}(\theta) \notin \mathcal{T}(\theta, \mu_i)$. In return, for $\mu_i > \mu_i^{crit}(\theta)$, a higher friction coefficient than the critical one does not increase the hardness, meaning that $\theta'_{opt}(\theta) \in \mathcal{T}(\theta, \mu_i)$. In this regime Amontons-Coulomb law is

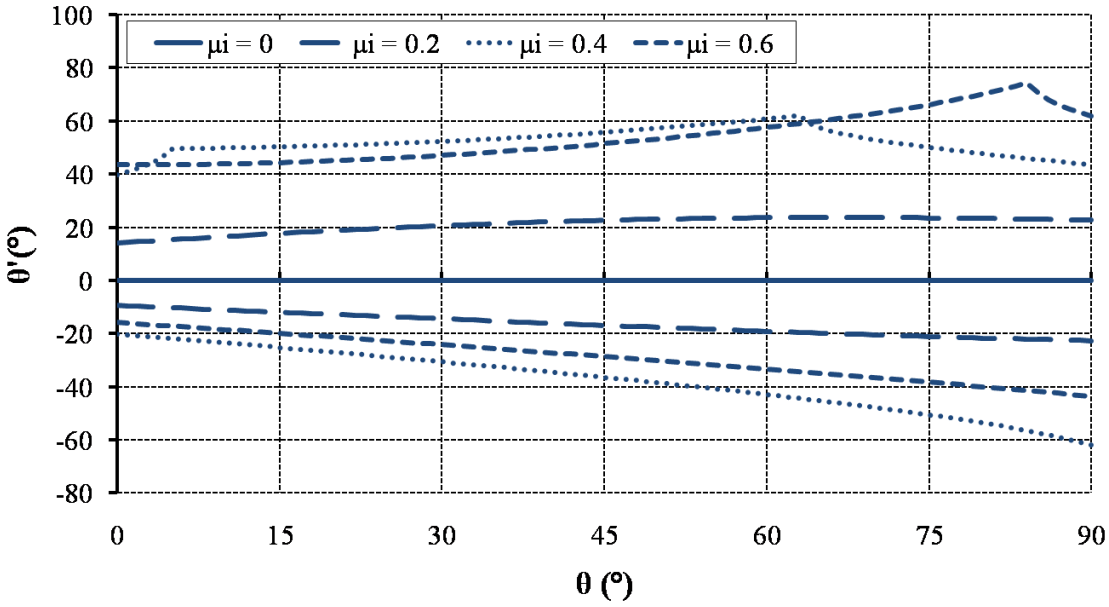

Figure 3-6: Admissible values of θ' vs. back-rake angle θ for different values of μ_i. $\mathcal{T}(\theta, \mu_i)$ is the domain contained between the two curves corresponding to the min. and max. values of θ'.

not saturated; this condition implies that there is static friction between the tested material and the blade. These two regimes are illustrated in figure 3-7, in form the of a hardness–friction coefficient plot for different back-rake angles.

An overall trend thus emerges. For cohesive materials, interface friction enhances the maximum value of the scratch hardness, up to a maximum value of $\mu_i^{crit}(\theta)$. For the Tresca and Von-Mises case, this critical friction coefficient is displayed in figure 3-8 (Curve labeled VM-TR). For $\mu_i^{crit}(\theta) < \mu_i^{crit}(\theta_{cr})$, the critical interface friction coefficient depends linearly on the back-rake angle.

3.5.2 Cohesive–Frictional Materials with Interface Friction

The trends found for purely cohesive materials are confirmed for materials exhibiting internal friction (Mohr-Coulomb and Drucker-Prager), namely (Fig.3-8):

- The existence of a critical back-rake angle θ_{cr}, for which interface friction μ_i does not affect the scratch hardness. This critical angle is a function of the internal friction as represented by φ (Mohr-Coulomb) or α (Drucker-Prager).

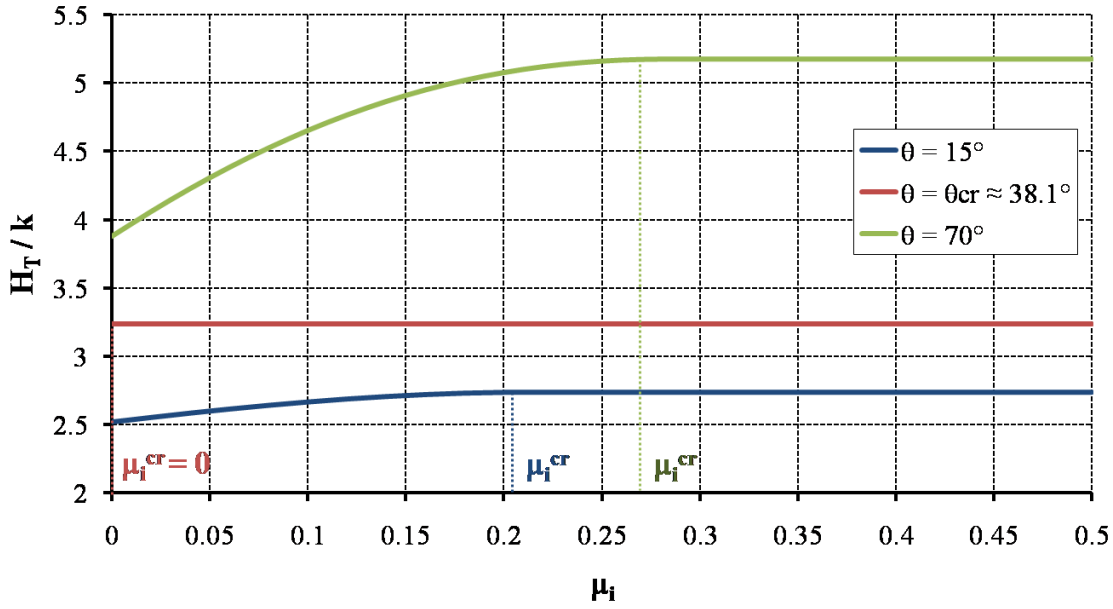

Figure 3-7: Hardness vs. interface friction coefficient for different back-rake angles θ (cohesive material).

- The existence of a critical interface friction coefficient μ_i^{crit}, below which the interface friction coefficient is saturated, while higher interface friction does not enhance the scratch hardness. This critical interface friction depends not only on the back-rake angle but on the internal friction as well.

- For frictional materials, there exists a back-rake angle $\theta \approx 74.5°$, for which $\mu_i^{crit} \approx 0.32$, independent of the internal friction of the materials.

3.6 Chapter Summary

The application of the principle of maximum plastic work to the problem of the rectangular scratch test yields a lower bound estimate of the tangential hardness. The proposition of a simple piecewise-constant stress field led us to the formulation of explicit relations between hardness and strength properties of cohesive-frictional materials. Both the hardness–to–cohesion ratio and the hardness–to–UCS ratio increase with higher internal friction. This dependence contradicts the idea of direct correlation between hardness and UCS. Moreover, the similarity of the hardness–to–cohesion

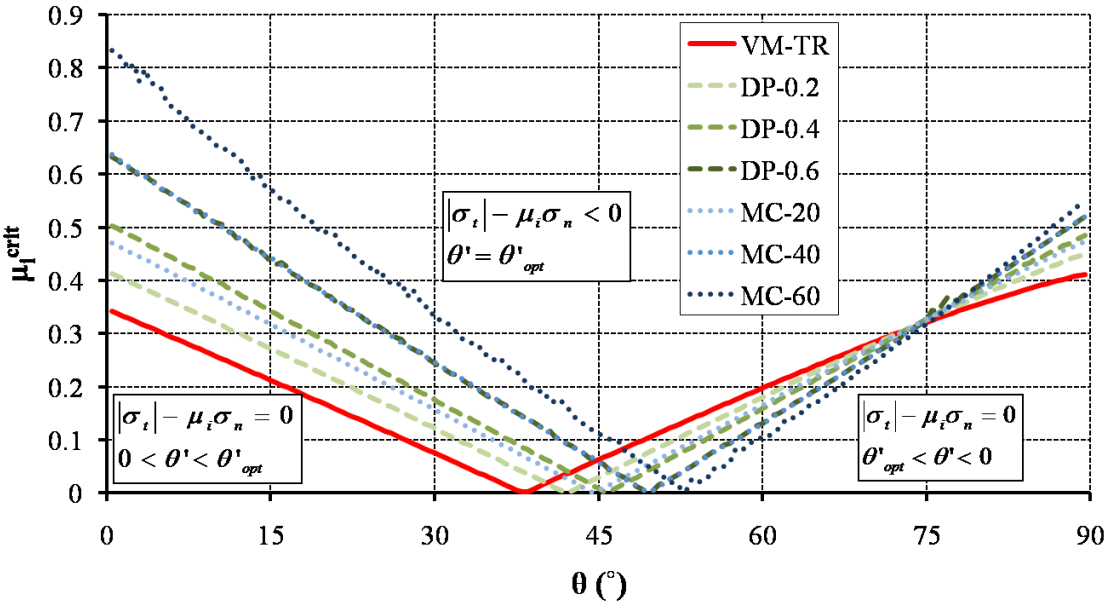

Figure 3-8: Critical friction coefficient μ_i^{crit} as a function of the back-rake angle θ for different materials: VM = Von Mises, TR=Tresca, DP-α = Drucker-Prager (with α the DP friction coefficient), MC-φ = Mohr-Coulomb (with φ the MC angle of internal friction).

formula in the Tresca and Von Mises cases may indicate that cohesion is a more relevant strength property than the UCS in the context of the scratch test. In order to be applicable, this model must now be validated through the comparison of the results obtained with different approaches, which is the focus of the next chapter.

Chapter 4

Validation

The litmus test for any yield design solution is the comparison of the lower bound with an upper bound solution. In this regard, we develop a model based on the complementary approach of yield design theory which yields an upper bound for the scratch hardness. In addition, an original upper bound solution and elastoplastic finite element solutions are also presented to validate the closed form solution obtained with the analytical model.

4.1 Comparison With an Upper Bound Solution

4.1.1 Theoretical Background: Upper Bound Limit Theorem

In contrast to the lower bound theorem (see Section 3.1), the upper bound theorem approaches the actual dissipation capacity at plastic collapse through kinematically and plastically admissible velocity fields. These are velocity fields $\underline{U}'$ which

- satisfy the velocity boundary conditions:

$$\underline{U}' \in \mathcal{K} \Leftrightarrow \underline{U}' = \underline{U}^d \text{ on } \partial\Omega_U \tag{4.1}$$

- are compatible with the plastic flow rule of the material at collapse:

$$\begin{cases} \underline{\underline{d}}' = \dot{\lambda}\frac{\partial f}{\partial \underline{\underline{\sigma}}} \; ; \; \dot{\lambda} \geqslant 0 \; ; \; f \leqslant 0 \; ; \; \dot{\lambda} f = 0 \\ [\![\underline{U}']\!] = \dot{\lambda}\frac{\partial f}{\partial \underline{T}} \; ; \; \dot{\lambda} \geqslant 0 \; ; \; f \leqslant 0 \; ; \; \dot{\lambda} f = 0 \end{cases} \tag{4.2}$$

Where $\underline{\underline{d}}' = \frac{1}{2}\left(\nabla \underline{U}' + (\nabla \underline{U}')^T\right)$ is the plastic strain rate tensor, $[\![\underline{U}']\!]$ is the velocity jump along a surface of discontinuity Γ, $\underline{T} = \underline{\underline{\sigma}} \cdot \underline{n}$ is the stress vector, and f is the strength function.

It can be shown, through application of the principle of maximum plastic work (see [61] Chapter 9 for a more detailed presentation), that any kinematically and plastically admissible velocity field provides an upper bound for the actual dissipation capacity, that is:

$$\underline{Q}^{lim} \cdot \underline{q} \leqslant \int_\Omega \underline{\underline{\sigma}} : \underline{\underline{d}}'' \, d\Omega + \int_\Gamma \underline{T} \cdot [\![\underline{U}']\!] \, d\Gamma \tag{4.3}$$

For a given yield surface, the flow rule (4.2) establishes a unique relation between the stress tensor $\underline{\underline{\sigma}}$ (respectively stress vector $\underline{T}$) and the strain rate tensor $\underline{\underline{d}}'$ (respectively velocity jump $[\![\underline{U}']\!]$). It can be shown that, for a given $\underline{\underline{d}}'$ kinematically admissible, the stress tensor $\underline{\underline{\sigma}}$ which satisfies this flow rule yields a maximum for the dissipation capacity:

$$\underline{\underline{\sigma}} \text{ satisfies (4.2)} \; \Leftrightarrow \underline{\underline{\sigma}} : \underline{\underline{d}}' = \sup_{\underline{\underline{\sigma}}' \in \mathcal{G}} \underline{\underline{\sigma}}' : \underline{\underline{d}}' \tag{4.4}$$

This leads to the definition of support functions, that express the maximum capacity of the material to dissipate the externally supplied energy at plastic collapse into heat for a given velocity field $\underline{U}'$:

$$\begin{cases} \pi(\underline{\underline{d}}') = \sup_{\underline{\underline{\sigma}}' \in \mathcal{G}} \underline{\underline{\sigma}}' : \underline{\underline{d}}' \\ \pi([\![\underline{U}']\!], \underline{n}) = \sup_{\underline{\underline{\sigma}}' \in \mathcal{G}} \underline{n} \cdot \underline{\underline{\sigma}}' \cdot [\![\underline{U}']\!] \end{cases} \tag{4.5}$$

Inserting (4.5) into the right-hand-side of (4.3) yields the maximum dissipation capacity of the whole system, referred to as the power function, which depends only on

the velocity field $\underline{U}'$:

$$P(\underline{U}') = \int_\Omega \pi(\underline{\underline{d}}')\ d\Omega + \int_\Gamma \pi(\llbracket \underline{U}' \rrbracket, \underline{n})\ d\Gamma \tag{4.6}$$

We can now formulate the upper bound limit theorem:

Theorem 2 *Any kinematically velocity field $\underline{U}'$ delivers an upper bound $P(\underline{U}')$ to the actual dissipation rate the limit load $\underline{Q}^{lim}$ realizes along the actual velocity field $\underline{q}$:*

$$\underline{Q}^{lim} \cdot \underline{q} = \min_{\underline{U}' \in \mathcal{K}} P(\underline{U}') \tag{4.7}$$

The dissipation rate $P(\underline{U}')$ is the maximum dissipation the material can afford, dissipating energy in the material bulk and along surfaces of discontinuity into heat form.

4.1.2 Upper Bound Model

Application of the upper bound limit theorem The first step of the upper bound approach consists in formulating the external plastic work rate $\underline{Q}^{lim} \cdot \underline{q}$. As this approach is applied to the same problem as the lower bound approach developed in chapter 3, the external plastic work rate supplied to the system remains expressed by (3.17). The application of the upper bound limit theorem yields:

$$H_S = H_T^{lim} \leqslant \frac{P(\underline{U}')}{Vwd}\ ;\ \forall\, \underline{U}' \text{ kinematically admissible} \tag{4.8}$$

We consider a frictionless contact between the blade and the material. It translates kinematically into an unconstrained tangential velocity along the blade. Combined with the non-penetration of the blade into the material, this condition leads to the formulation of the kinematic boundary condition that a velocity field has to satisfy to be k.a., thus defining the set $\mathcal{K}$ of kinematically admissible velocity fields:

$$\mathcal{K} = \left\{ \underline{U} \;\middle|\; \begin{array}{cc} \underline{U}(\underline{x}) \cdot \underline{n} = \underline{V} \cdot \underline{n} = -V \cos\theta & \forall \underline{x} \in \overline{OA} \\ \underline{U}(\underline{x}) = \underline{0} & \text{for } |\underline{x}| \to \infty \end{array} \right\} \tag{4.9}$$

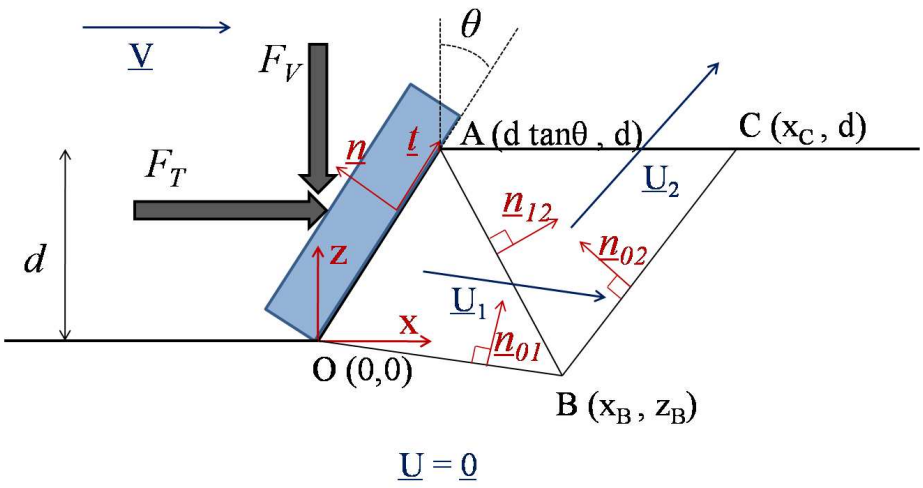

Figure 4-1: Rigid blocks failure mechanism.

The upper bound approach consists now in finding a velocity field $\underline{U} \in \mathcal{K}$ that minimizes the power function $P(\underline{U})$ to find the best estimation of the tangential hardness.

Choice of velocity field We propose a rigid blocks failure mechanism as depicted in figure 4-1. The application of the kinematic admissibility (4.9) yields $U_{1n} = \underline{U}_1 \cdot \underline{n} = -V\cos\theta$, thus reducing the proposed family of velocity fields to a 6-dimensional subset of $\mathcal{K}$, the 6 degrees of freedom being: U_{1t},U_{2x},U_{2z}, x_B, z_B, and x_C, where $U_{1t} = \underline{U}_1 \cdot \underline{t}$ is the tangential component of the velocity at the interface between the blade and the material. In this failure mechanism, energy is dissipated only at the surfaces of velocity discontinuity $\overline{OB}$, $\overline{AB}$, and $\overline{BC}$. It is indeed trivial to check that $\underline{\underline{d}} = \underline{\underline{0}}$ in Ω. As we assume that the contact between the blade and the material is frictionless, there is no dissipation along $\overline{OA}$. The total dissipation capacity $P(\underline{U})$ reads then:

$$P(\underline{U}) = \int_{\overline{OB}} \pi(\underline{x}, \underline{n}_{01}, \underline{U}_1) dS + \int_{\overline{BC}} \pi(\underline{x}, \underline{n}_{02}, \underline{U}_2) dS + \int_{\overline{AB}} \pi(\underline{x}, \underline{n}_{12}, \underline{U}_2 - \underline{U}_1) dS \quad (4.10)$$

Cohesive materials: Von Mises and Tresca criteria We start by considering purely cohesive materials, as expressed by the Tresca or the Von Mises criterion (Table 3.1). It can be shown [53] that the support function for velocity discontinuities is, for

the Tresca criterion:

$$\pi(\underline{n}, [\![\underline{U}]\!]) = \begin{cases} +\infty & \text{if } [\![\underline{U}]\!] \cdot \underline{n} \neq 0 \\ c \times |[\![\underline{U}]\!]| & \text{if } [\![\underline{U}]\!] \cdot \underline{n} = 0 \end{cases} \tag{4.11}$$

This expression remains valid for a Von Mises material, provided that the cohesion c is replaced by the shear strength k. The consideration of constant velocities in the three different rigid blocks allows us to express $P(\underline{U})$ in terms of the different degrees of freedom:

$$P(\underline{U}) = c \times (|\underline{U}_1| \, |\underline{OB}| + |\underline{U}_2| \, |\underline{BC}| + |\underline{U}_2 - \underline{U}_1| \, |\underline{AB}|) \tag{4.12}$$

with the constraint:

$$\underline{U}_1 \cdot \underline{n}_{01} = \underline{U}_2 \cdot \underline{n}_{02} = (\underline{U}_2 - \underline{U}_1) \cdot \underline{n}_{12} = 0 \tag{4.13}$$

These three kinematic conditions are imposed by the shape of the power function (4.11) and reduce by three the number of degrees of freedom. Developing them leads to the expression of the three unknown velocity components U_{1t}, U_{2x}, and U_{2z} as functions of the geometric parameters x_B, z_B, and z_C:

$$\begin{cases} U_{1t} = V \times \frac{z_B}{x_B \cos\theta - z_B \sin\theta} & \text{(a)} \\ U_{2x} = V \times \frac{x_B - x_C}{(z_B - 1)(x_C - d\tan\theta)} & \text{(b)} \\ U_{2z} = V \times \frac{d}{x_C - d\tan\theta} & \text{(c)} \end{cases} \tag{4.14}$$

Inserting these expressions into equation (4.12) yields:

$$P(\underline{U}) = c \times V \times d \times \tilde{P}(\tilde{x}_B, \tilde{z}_B, \tilde{x}_C) \tag{4.15}$$

where $\tilde{P}$ is a dimensionless rational function of order 2 depending on the three dimensionless parameters $\tilde{x}_B = x_B/d$, $\tilde{z}_B = z_B/d$, and $\tilde{x}_C = x_C/d$. Applying the upper

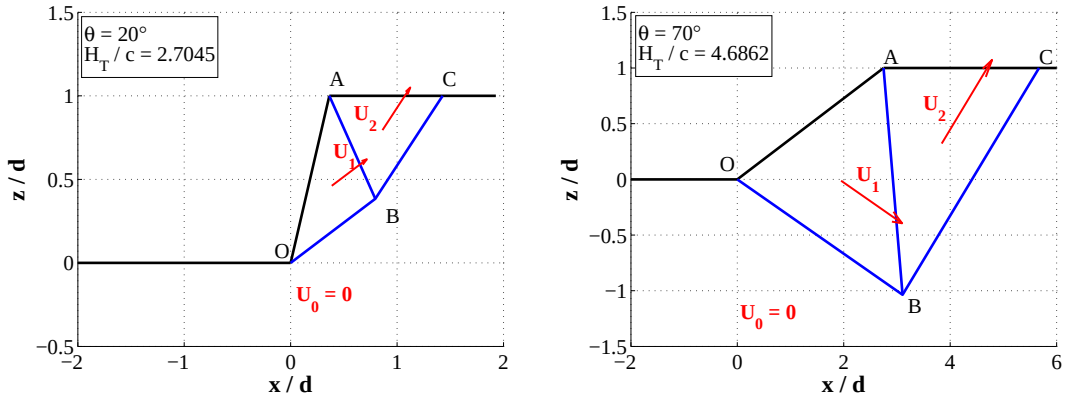

(a) (b)

Figure 4-2: Result of the upper-bound model optimization for a cohesive material for (a) $\theta = 20°$ and (b) $\theta = 70°$.

bound limit theorem (4.8) hence yields in the cohesive case:

$$H_S \leqslant H_T(\tilde{x}_B, \tilde{z}_B, \tilde{x}_C) = c \times \tilde{P}(\tilde{x}_B, \tilde{z}_B, \tilde{x}_C) \ \forall \text{ admissible } \tilde{x}_B, \tilde{z}_B, \tilde{x}_C \tag{4.16}$$

With kinematic admissibility satisfied by the choice of the shape of the velocity fields, the term 'admissible' refers here to obvious geometric considerations and can be expressed in the following way:

$$\begin{cases} \tilde{x}_B > \tilde{z}_B \tan\theta & \overline{AB} \text{ is in the material} \quad \text{(a)} \\ \tilde{x}_C > \tan\theta & \text{C is at the right of A} \quad \text{(b)} \end{cases} \tag{4.17}$$

We carry out the minimization of $\tilde{P}$ numerically with Matlab, using the `fmincon` function based on a Newton-type algorithm. The initial value fed to the function is by default $[\tilde{x}_B, \tilde{z}_B, \tilde{x}_C] = [1, 0, 1 + \tan\theta]$, but can be adjusted if necessary to help convergence. Results of the optimization are shown in figure 4-2 for angles $\theta = 20°$ and $\theta = 70°$. Figure (4-3) represents the hardness–to–cohesion ratio versus the back-rake angle θ for various materials, including Von Mises and Tresca (labeled VM).

Cohesive-frictional materials: Drucker-Prager and Mohr-Coulomb criteria We now implement the Mohr-Coulomb and Drucker-Prager criteria to model frictonal-cohesive materials. It can be shown [53] that the power functions of these criteria for velocity discontinuities are:

$$\pi(\underline{n}, [\![\underline{U}]\!]) = \begin{cases} +\infty & \text{if } [\![\underline{U}]\!] \cdot \underline{n} < |[\![\underline{U}]\!]| \sin\varphi \\ \frac{c}{\tan\varphi} \times [\![\underline{U}]\!] \cdot \underline{n} & \text{if } [\![\underline{U}]\!] \cdot \underline{n} \geqslant |[\![\underline{U}]\!]| \sin\varphi \end{cases} \tag{4.18}$$

$$\pi(\underline{n}, [\![\underline{U}]\!]) = \begin{cases} +\infty & \text{if } [\![\underline{U}]\!] \cdot \underline{n} < |[\![\underline{U}]\!]| \sqrt{\frac{\alpha^2}{1-\alpha^2/3}} \\ \frac{k}{\alpha} \times [\![\underline{U}]\!] \cdot \underline{n} & \text{if } [\![\underline{U}]\!] \cdot \underline{n} \geqslant |[\![\underline{U}]\!]| \sqrt{\frac{\alpha^2}{1-\alpha^2/3}} \end{cases} \tag{4.19}$$

Unlike in the Tresca and Von Mises cases, the condition for the power function to be finite is not an equality but a non-linear inequality, which accounts for the dilation of frictional materials at plastic collapse. Direct relationships between geometric parameters x_B, z_B, x_C, and velocity parameters U_{1t}, U_{2x}, U_{2z} could hence not be found, which calls for the use of a numerical optimization procedure on the 6 parameters with non-linear constraints. Once again this is performed with the Matlab function `fmincon`.

Figure 4-3 shows that the addition of an internal friction coefficient increases the scratch hardness by a factor, which itself increases with the angle θ.

Extension to 3D For the Von Mises and Tresca criteria, this model can easily be extended to a three-dimensional problem by adding a width w to the blade and the two rigid blocks in motion at plastic collapse. As a result, two new surfaces of tangential velocity discontinuity are added: triangles OAB and ABC, using the same nomenclature as in figure (4-1). The expression of the dissipation function becomes then:

$$P(\underline{U}) = c \times \left[w \times \left(|\underline{U}_1| \, |\underline{OB}| + |\underline{U}_2| \, |\underline{BC}| + |\underline{U}_2 - \underline{U}_1| \, |\underline{AB}| \right) + 2 \left(\langle OAB \rangle \, |\underline{U}_1| + \langle ABC \rangle \, |\underline{U}_2| \right) \right] \tag{4.20}$$

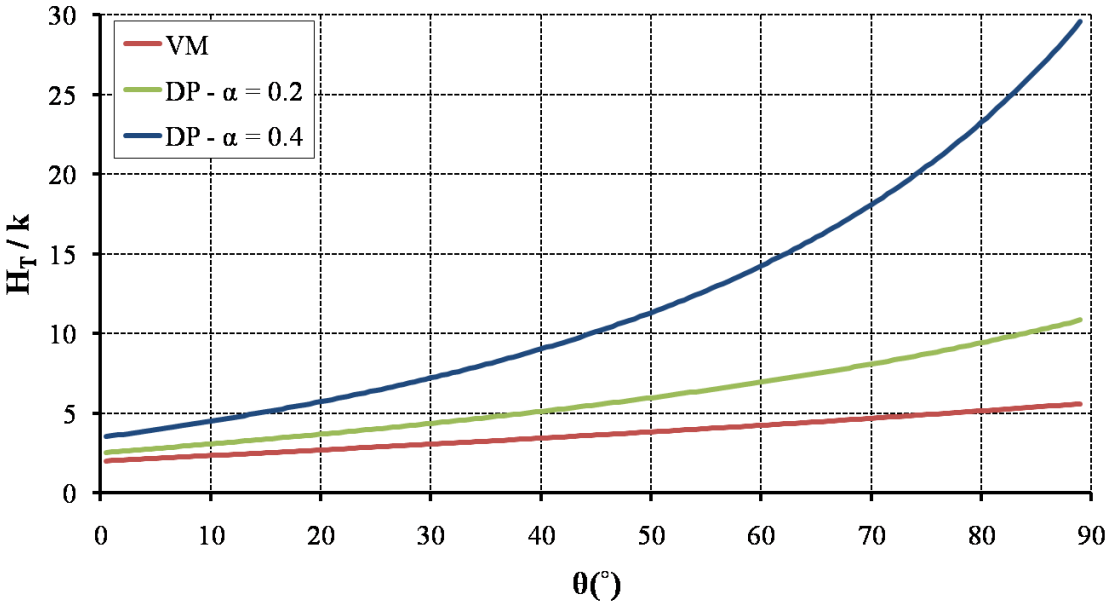

Figure 4-3: Hardness–to–shear strength ratio vs. back-rake angle θ for Drucker-Prager materials with different internal friction coefficients.

where $\langle\rangle$ stands for the area of the triangle. Dimensionally speaking, we see that the terms already appearing in the 2D model are of the order of dw, while the side terms are of the order of d^2. This extension to 3D will then converge to the 2D model when $w/d \to +\infty$. Apart from these new terms, the details of the optimization are similar to the 2D case. This 3D model makes it possible to study the influence of the depth–to–width ratio d/w, as shown on figure 4-4. For width–to–depth ratios smaller than 100, the effect of the third dimension is not negligible and must be accounted for.

Summary The application of the upper bound limit theorem to the scratch test problem led us to develop a simple model based on a 6-parameter velocity field. An upper bound for the hardness is obtained for cohesive and frictional-cohesive materials by numerical optimization. The comparison of these results with the lower bound approach will serve as a validation for the closed form solutions obtained in chapter 3.

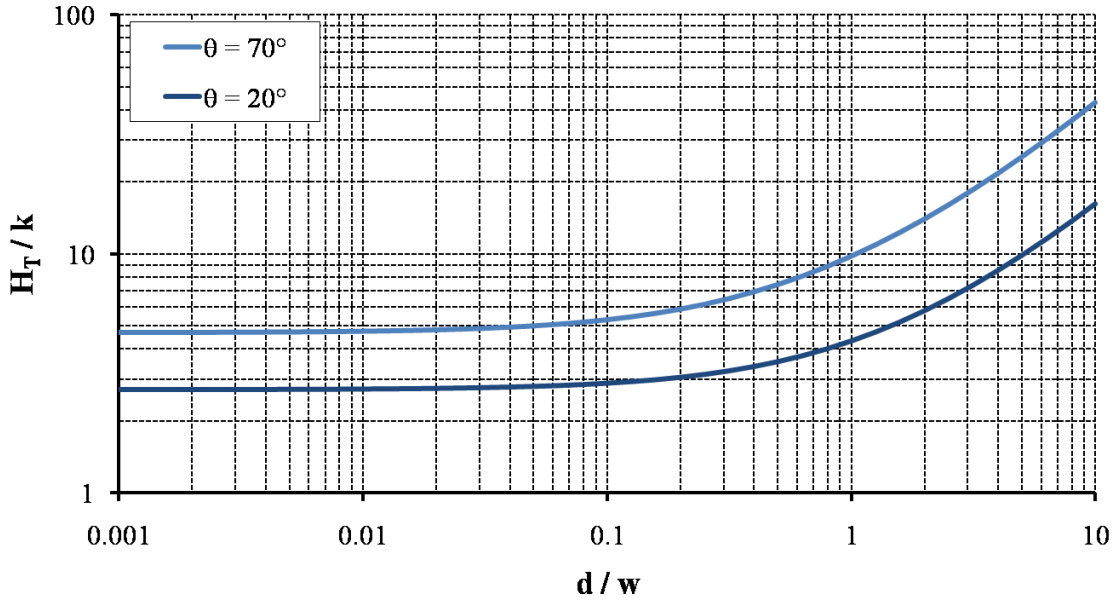

Figure 4-4: Influence of the depth–to–width ratio in the upper-bound model for the scratch test

4.1.3 Influence of the Back-Rake Angle θ

We first compare the influence of the back-rake angle θ. Figure 4-5 shows the hardness H_T versus the back-rake angle θ for both the upper bound and the lower bound solutions. The 3D upper-bound solutions diverge for large back-rake angles $\theta > 85°$. This limit being set, the upper bound solution is very close to the lower bound. This result shows that the actual solution for H_S is found for back-rake angles smaller than 45° and w/d ratio smaller than 100 with an accuracy of less than 8% (Figure 4-6). Typical scratch tests on rocks have a width–to–depth ratio between 10 and 100 [51]. In such a case, the yield design theory models predict with a 10% accuracy for angles θ smaller than 30°.

4.1.4 Influence of the Internal Friction (α or φ)

The correlation between the upper bound and lower bound models are good for cohesive materials modeled by Von Mises or Tresca criteria, especially at small θ angles. Given the extensive application of this thesis to the fields of soil mechanics or cementi-

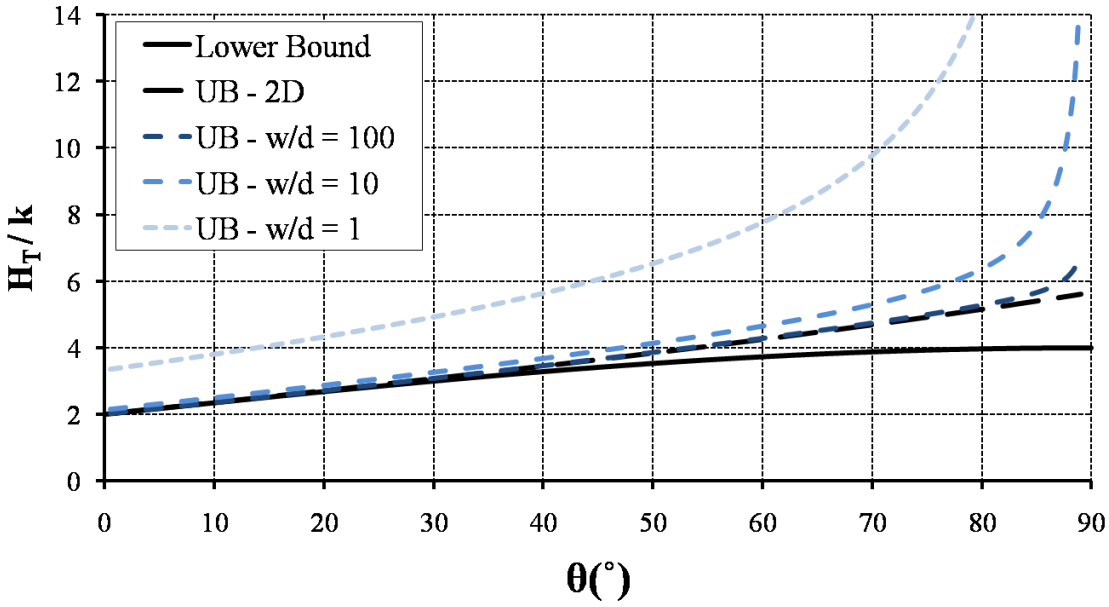

Figure 4-5: Hardness–to–shear strength ratio vs. Back-rake angle θ for a Von Mises material. Comparison to lower bound and upper-bound solutions for different w/d ratios.

tious materials, the ability of the models to predict the behavior of pressure-sensitive materials is of utmost importance. Figure 4-7 plots the hardness–to–shear strength ratio obtained with lower bound and upper bound models versus the internal friction coefficient α for a Drucker-Prager material for three different back-rake angles $\theta = 20, 50, 70°$. These curves show a very strong correlation for the smallest angle θ for almost all the range of α authorized ($\alpha < \sqrt{3/4} \approx 0.86$). Figure 4-8 displays the relative difference between the upper bound value and the lower bound value. For $\theta = 20°$ the upper bound is less than 5% higher than the lower bound for $\alpha < 0.67$, which encompasses most of the cohesive-frictional materials that can be modeled with a Drucker-Prager coefficient. The tendency of the difference increasing for greater θ angles already observed in the previous paragraph is observed again in the frictional case and is amplified by internal friction. Indeed, for $\theta = 70°$, the upper bound is twice as large as the lower bound from $\alpha = 0.52$ onward and more than three times as large for $\alpha > 0.62$.

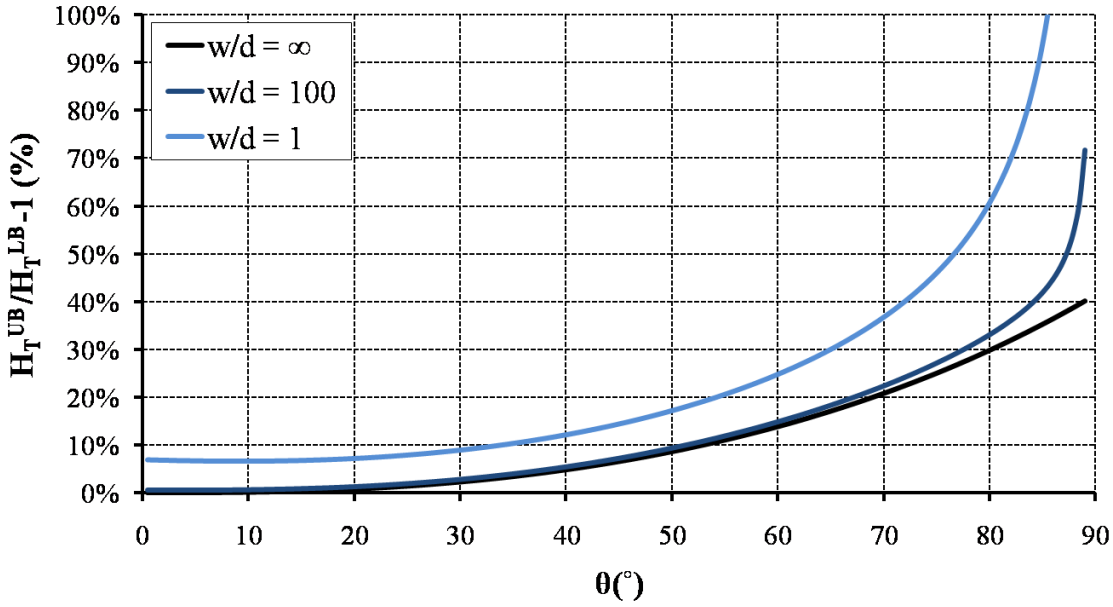

Figure 4-6: Relative variation of the upper bound solution compared with the lower bound solution vs. back-rake angle θ for a Von Mises material for various values of the w/d ratio.

4.2 Comparison With an Original Limit Analysis Solution

4.2.1 Presentation of the Solver

We here employ the computational yield design analysis solver developed by Borges et al. [8],[46],[9]. The algorithm aims at directly finding a numerical estimate of the stress and velocity fields which are a solution of the limit analysis problem. In fact, the approach employs both stresses and velocities as degrees of freedom, and subjects them to the following conditions:

1. The stress field $\underline{\underline{\Sigma}}$ satisfies the weak form of the equilibrium condition ($\underline{\text{div}}\ \underline{\underline{\Sigma}} = \underline{0}$). For the scratch test, this condition reads[1]:

$$H_T(wd)V = \int_\Omega \underline{\underline{\Sigma}} : \underline{\underline{D}}'\, d\Omega \tag{4.21}$$

[1] no discontinuities are considered in the model

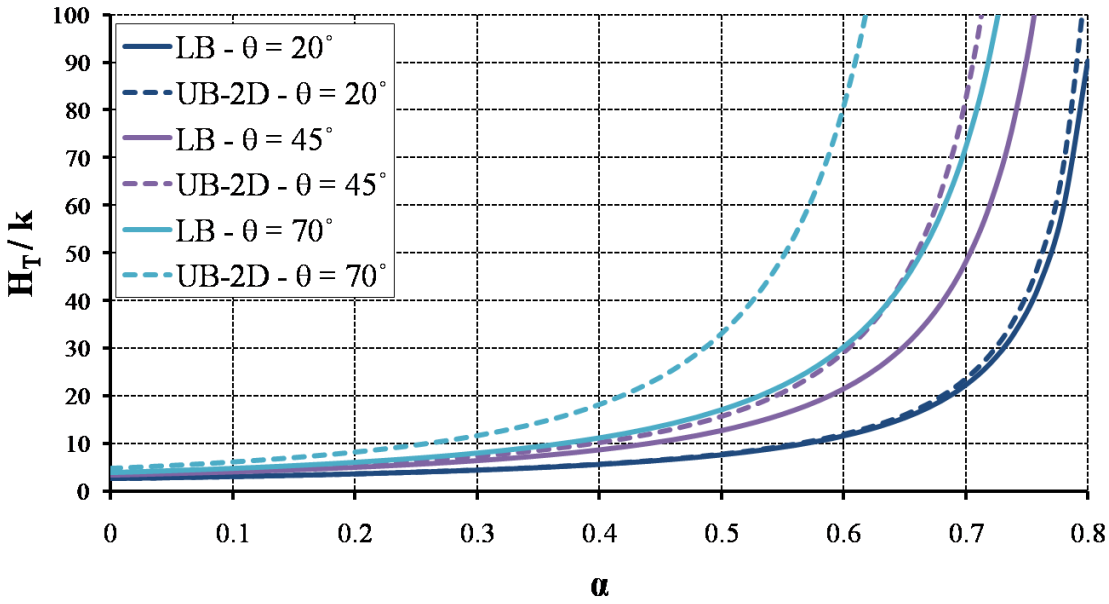

Figure 4-7: Hardness–to–shear strength ratio vs. Drucker-Prager friction coefficient α. Comparison of lower bound and upper-bound solutions for different back-rake angles θ.

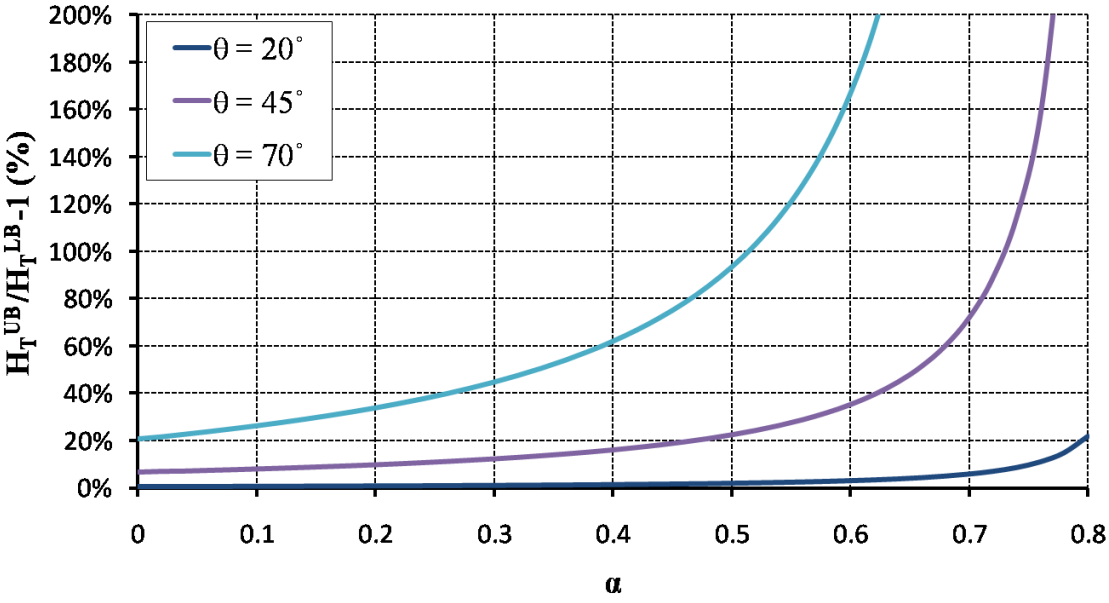

Figure 4-8: Relative variation of the upper bound solution compared with the lower bound solution vs. Drucker-Prager coefficient α for different back-rake angles θ.

where $\underline{\underline{D}}'$ is the plastic strain rate tensor derived from the velocity field $\underline{U}'$ kinematically admissible in the sense of (4.9).

2. The stress field satisfies the strength criterion:

$$f(\underline{\underline{\Sigma}}) \leqslant 0 \tag{4.22}$$

Among the classic strength criteria, Von Mises and Drucker-Prager are implemented in the solver.

3. The strain rate $\underline{\underline{D}}'$ obeys an associated flow rule as defined by (4.2).

The implementation of the approach requires on the one side the discretization of the domain Ω, and on the other hand an efficient formulation to solve the constraint conditions. The first condition is achieved by using the classical procedures of finite element analysis (see e.g. [6]). The infinite half-space Ω is replaced by a finite domain Ω' discretized by finite elements (See figure 4-9). The kinematic condition at infinity $\underline{U}' = \underline{0}$ for $|\underline{x}| \to +\infty$ is replaced by the following zero-velocity conditions:

$$\begin{cases} U'_x = 0 \text{ for } x = x_{min} \text{ and } x = x_{max} \\ U'_z = 0 \text{ for } z = z_{min} \end{cases} \tag{4.23}$$

The second objective is achieved by using a complex algorithm presented in details in [8].

All the simulations are carried out in 2D with the plane strain rate assumption for a single back-rake angle $\theta = 20°$. For a given material, the solver yields the hardness–to–cohesion ratio H_T/k, along with the kinematically admissible and strength compatible velocity field. Unlike in the classic upper bound approach, both Σ and $\underline{U}'$ are used as degrees of freedom for the optimization. However one can see that the difference lies only in the formulation of the strength compatibility: while in the classic upper bound approach the energy dissipation rate $P(\underline{U}')$ is computed using the support function $\pi(\underline{\underline{D}}')$, it is calculated in the solver using the strength compatible stress tensor $\underline{\underline{\Sigma}}$, constrained by the associated flow rule (4.2). As stated in the presentation of the

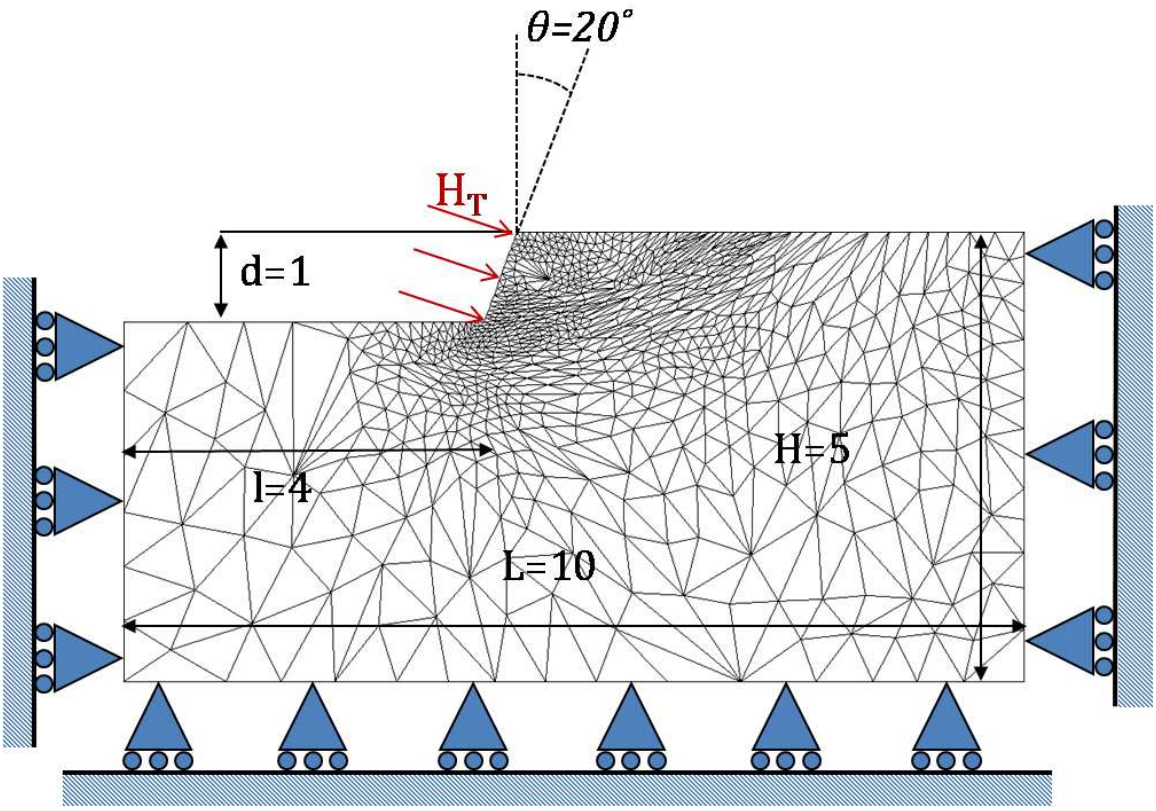

Figure 4-9: Geometry, mesh (1,416 6-node triangle elements) and loading conditions of the upper bound solver.

upper bound limit theorem, such a stress tensor is unique and $\pi(\underline{\underline{D}}') = \underline{\underline{\Sigma}} : \underline{\underline{D}}'$. As a result, while the implementation is different, this solver also yields an upper bound value for the dissipation capacity, and hence for the hardness.

4.2.2 Comparison of the Results

For a Von-Mises material, the limit analysis solver with the finest mesh available (7,622 elements) predicts a tangential hardness –to–cohesion ratio of $H_T/k = 2.72$. This value is just 1.5% greater than the value provided with the closed form solution (3.45) for the considered back-rake angle of $\theta = 20°$:

$$2\,(1 + \sin\theta) = 2.684 \leqslant \frac{H_S}{k} \leqslant 2.72 \tag{4.24}$$

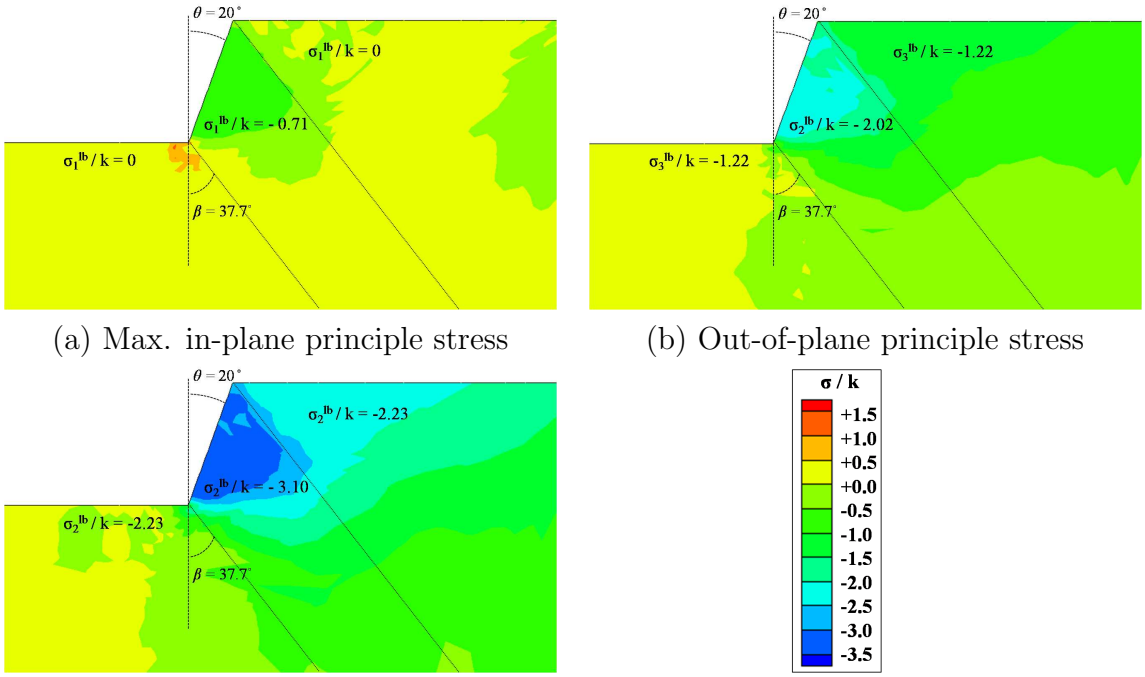

(a) Max. in-plane principle stress

(b) Out-of-plane principle stress

(c) Min. in-plane principle stress

Figure 4-10: Principle stresses computed by the yield design software for a Drucker-Prager material ($\alpha = 0.1$) with $\theta = 20°$, and normalized by the shear strength k. The values expected with the lower bound solution are superimposed.

It is also 0.6% greater than the value obtained with the upper bound model based on velocity discontinuities ($H_T^{UB}/k = 2.705$). On the one hand, the relatively good agreement of this model and the lower bound solution can be attributed to the accuracy of the constant stress assumption field under the blade, which represents the main restriction of the lower bound solution. In the current case this fits well with what is seen in more complex simulations in which the stress field can vary. The hardness is determined by the state of stress at the blade–material interface. The upper bound model predicts the development of a plastic zone under the blade where the stress field is constant (Figure 4-10), much like in the lower bound model.

On the other hand, the good agreement with the upper bound solution based on velocity discontinuities presented in this thesis can be attributed to the accurate approximation of the velocity field and dissipation pattern developed in the material, as shown by the superposition of the upper bound solutions on the solver's solutions (Figure 4-11).

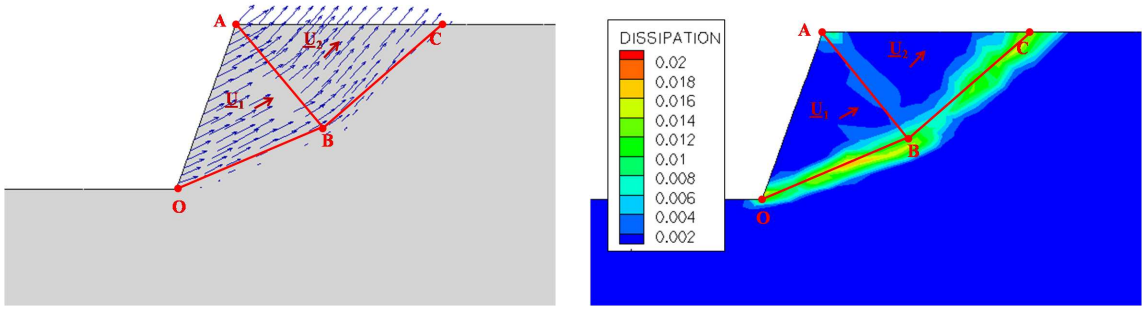

(a) Velocity field (b) Plastic Dissipation

Figure 4-11: Correlation between the upper bound optimization solution (superimposed in red) and the solver's solution for a Drucker-Prager criterion ($\alpha = 0.1$) and $\theta = 20°$.

A similar confrontation of lower and upper bound solutions is carried out for scratch tests onto a Drucker-Prager material, with the objective to validate the closed form expressions. This comparison is displayed in figure 4-12. Convergence of the upper-bound limit analysis solver could only be achieved for $\alpha \leqslant 0.12$. In this range, the upper bound solver's solution differs from the lower bound solution by only 4%, which confirms the accuracy of the proposed lower bound solutions for frictional materials with small internal friction coefficients.

4.3 Comparison with Elastoplastic Finite Element Solutions

Finally, an independent comparison is made with elastoplastic finite element solutions. A first order comparison can be made with published FE-solutions of the scratch test: Lee et al. [35] modeled the scratching of an elastic perfectly plastic material by a rigid spherical indenter and obtained hardness–to–yield strength ratios ranging from 2 to 3.5. Bellemare et al. [7] modeled the frictional sliding (with interface friction $\mu_i = 0.15$) of a conical indenter (half-cone angle 70.3°) on an elastic plastic material including hardening and obtained a hardness–to–yield strength ratio of 2.8 in the case of very small hardening. While both results were obtained with other scratch

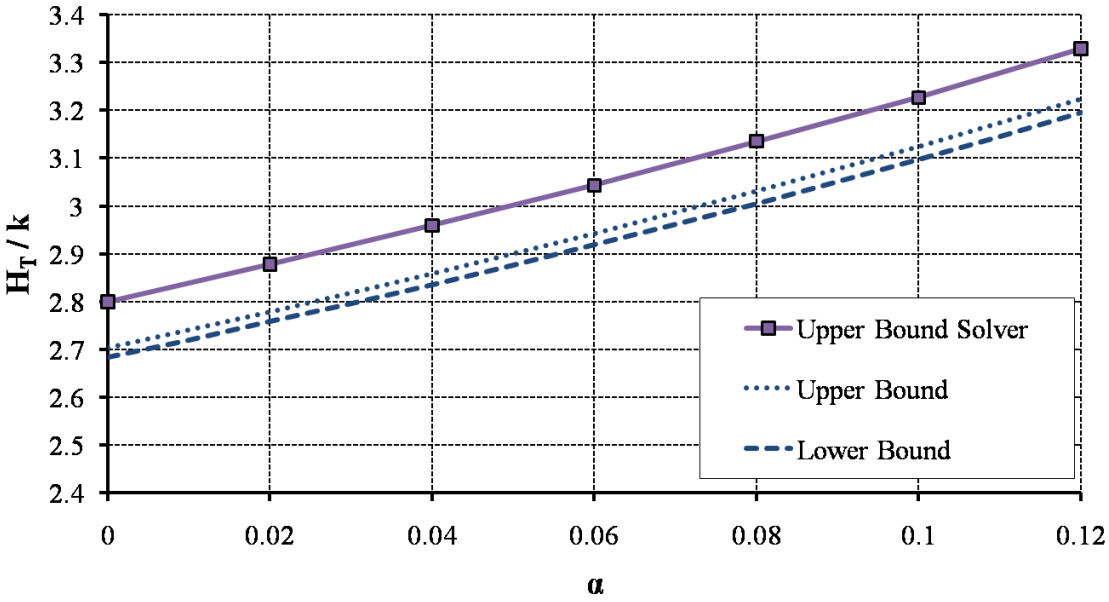

Figure 4-12: Yield design solutions compared to upper bound solver (1,416 elements) for Hardness-to-cohesion ratio for a Drucker-Prager material with back-rake angle $\theta = 20°$.

geometries than the straight scratch test considered in our approach, the values agree reasonably well with the hardness–to–yield strength ratios for the pure Von Mises material cohesive case obtained with the lower-bound approach. In fact, considering a high back-rake angle $\theta = 70.3°$ yields a hardness–to–yield strength ratio of 2.3 in the frictionless interface case, and a value of 2.85 for the frictional interface case. The upper bound model gives a hardness–to–yield strength ratio of 2.71 without considering friction at the interface. The good agreement with the FE results hints toward a minor influence of the scratch geometry on the hardness–strength relation.

4.3.1 Finite Element Model

A more refined comparison is made here with finite element simulations for the cohesive-frictional case considering our straight scratch test geometry. In the FE simulations we consider the actual contact between the rigid blade and the deformable material sample. In these simulations the material parameters were chosen so as to

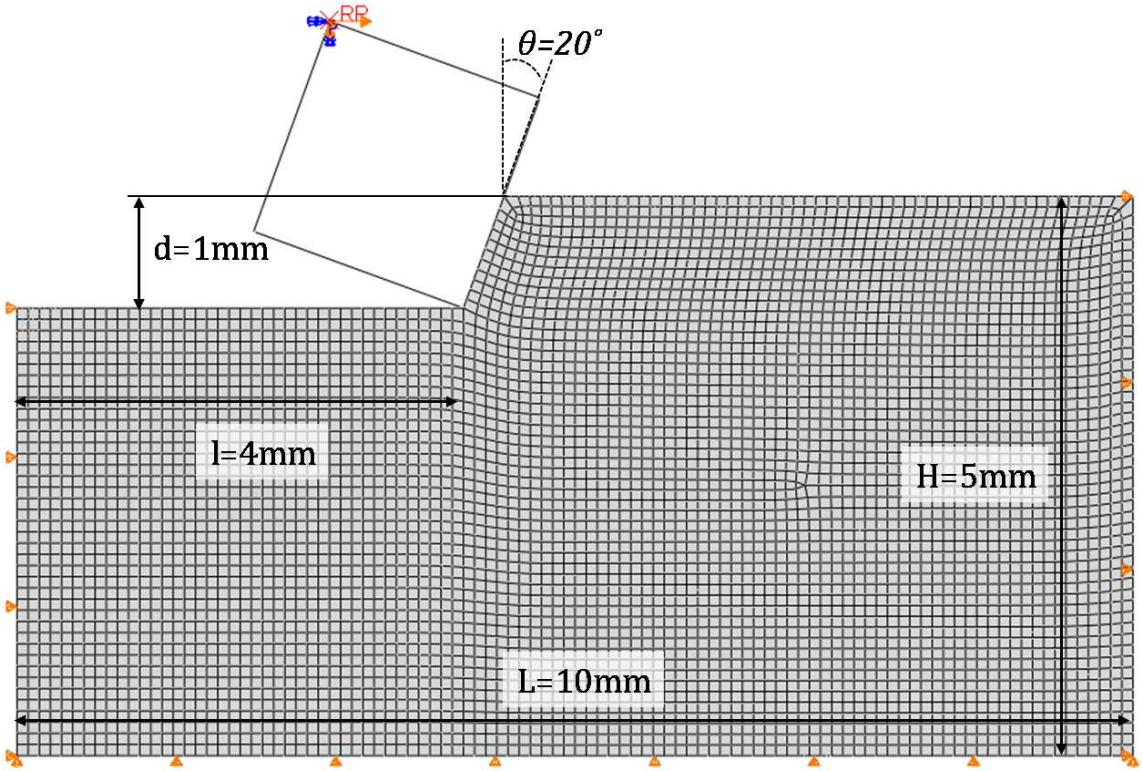

Figure 4-13: Geometry and loading conditions of the Abaqus finite element model for $\theta = 20^{\circ}$ (14,526 nodes and 4,742 plane strain quadratic elements).

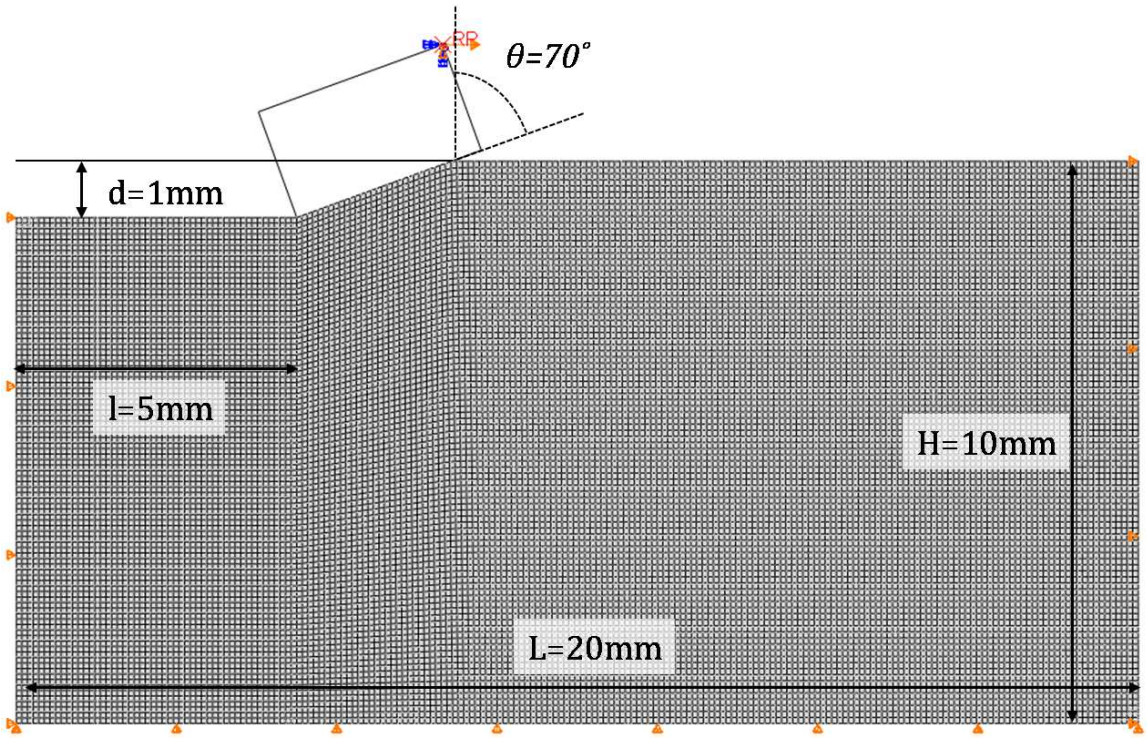

Figure 4-14: Geometry and loading conditions of the Abaqus finite element model for $\theta = 70°$ (56,063 nodes and 18,492 plane strain quadratic elements).

approximate as closely as possible, by means of elastoplastic[2] simulations, the rigid plastic case, namely a shear-strength –to– Young's modulus ratio of $k/E = 5.8 \times 10^{-4}$. Plane strain quadratic elements were used (CPEG8R, 10 mm thickness) with reduced integration, and large deformations were allowed. Two geometries were used (Figures 4-13 and 4-14, corresponding to back-rake angles $\theta = 20°$ and $\theta = 70°$, for a common depth of scratch $d = 1mm$. For both geometries the typical size of an element was 0.1mm, to be compared with the size of the systems: $L \times H = 10\text{mm} \times 5\text{mm}$ for $\theta = 20°$, and $L \times H = 20\text{mm} \times 10\text{mm}$ for $\theta = 70°$. The displacement of the blade was chosen such that plasticity would be activated. For the $\theta = 20°$ simulations fully plastic behavior occurred with very little geometrical hardening for a displacement of 0.02mm as shown in typical Force–Displacement curves depicted in Figure 4-15. In

[2]In Abaqus, the built-in Drucker-Prager material are defined as follows:

$k = d/\sqrt{3}$ where d is the yield stress defined in Abaqus in shear mode

$\alpha = \tan\beta/\sqrt{3}$ where β is the friction angle defined in Abaqus. The dilation angle is set equal to β.

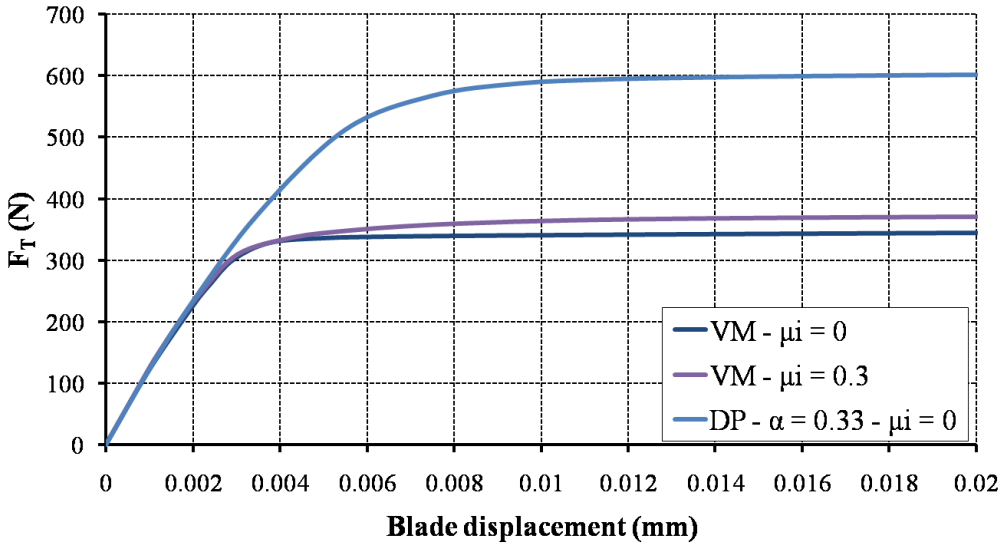

Figure 4-15: Typical Force–Displacement curves obtained with the FE simulations for $\theta = 20°$.

the $\theta = 70°$ case, geometric hardening is more significant (Figure 4-16). In this latter case, hardness is measured at a displacement of 0.2mm. This order of magnitude difference between the displacements needed to activate plasticity can be explained by the horizontal strain sustained by the material under the blade. It can indeed be inferred that $\epsilon_{xx} \propto u^{\theta}_{blade}/(d \tan\theta)$. Given that $\tan(70°) \approx 7.5 \tan(20°)$ and d equals 1mm in both geometries, getting approximately the same horizontal strain will require increasing the displacement of the blade by a factor close to 7.5. We chose to use the value $u^{70°}_{blade} = 0.2$mm but the presence of non-negligible hardening must be kept in mind when interpreting the results.

In both cases, the value of the hardness–to–shear strength ratio is calculated by dividing the force recorded (in N) by $k \times w \times d = 11.5MPa \times 10mm \times d_f$, d_f being the actual height of the contact between the blade and the material measured at the end of the step. This value d_f is less than 2% off the initial value $d = 1mm$ in the frictionless cases but can be more than 10% higher in the presence of interface friction for the 70° geometry. A first general observation is that elastoplastic solutions predict higher values than the lower bound yield design solutions. This hints toward a role of the elastic energy stored in front of the interface into the material. This energy

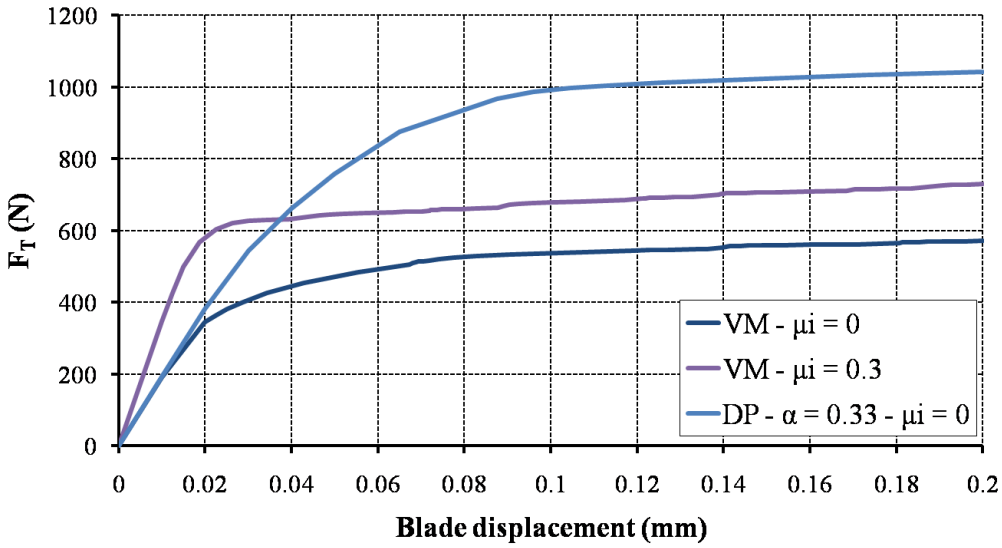

Figure 4-16: Typical Force–Displacement curves obtained with the FE simulations for $\theta = 70°$.

θ	E (GPa)	ν	k (MPa)	α	μ_i	d (mm)	Blade displ. (mm)	El. size (mm)
20°	20	0.4	11.55	$[0, 0.4]$	$[0, 0.5]$	1	0.02	0.1
70°	20	0.4	11.55	[0.0.4]	$[0, 0.5]$	1	0.2	0.1

Table 4.1: Finite Element Model parameters

storage entails an increase of the resistance to scratching similar to plastic hardening. The effects of the elasticity parameters (E and ν) are nevertheless not significant as long as the plastic regime is reached (see table 4.2). In the next paragraphs we show

Simulation	E (GPa)	ν	Reaction Force (N)	H_T/k	Variation
1 (Ref)	20	0.4	470.9	4.08	–
2	20	0	469.4	4.06	−0.32%
3	20	0.2	470.3	4.07	−0.13%
4	20	0.49	472.2	4.09	+0.28%
5	200	0.4	473.0	4.10	+0.44%

Table 4.2: Influence of the elasticity coefficients in the FE simulation results ($\theta = 20°$, $\alpha = 0.21$)

an investigation of the correlation between the FE simulation and the yield design models for two different back-rake angles $\theta = 20°$ and $\theta = 70°$.

4.3.2 Influence of the Drucker-Prager Internal Friction Coefficient

The comparison of the FE results with the yield design solutions for a Drucker-Prager material (Fig. 4-17) yields two contrasting conclusions. On the one hand the results of the finite element simulation for $\theta = 20°$ show a great deal of consistency with the closed form solutions based on the lower bound solution, and with the upper bound solutions (which were shown to be less than 5% higher), given that the FEM results are 10% greater than the lower bound solutions over the range of internal friction coefficient α. This difference can be reduced by finer meshing. The proximity of the lower and upper bound does not allow us to use FE simulation to validate one over the other. On the other hand, the results of the FE simulations for $\theta = 70°$ are not showing the same increase rate of H_T w.r.t. α. This lack of consistency can be explained by the geometric hardening observed with this geometry. Indeed, the increase of the friction coefficient α increases the yield strength of the material and, as a consequence, delays the activation of plasticity. The choice of measuring the hardness at a fixed value of the displacement of the blade can lead to

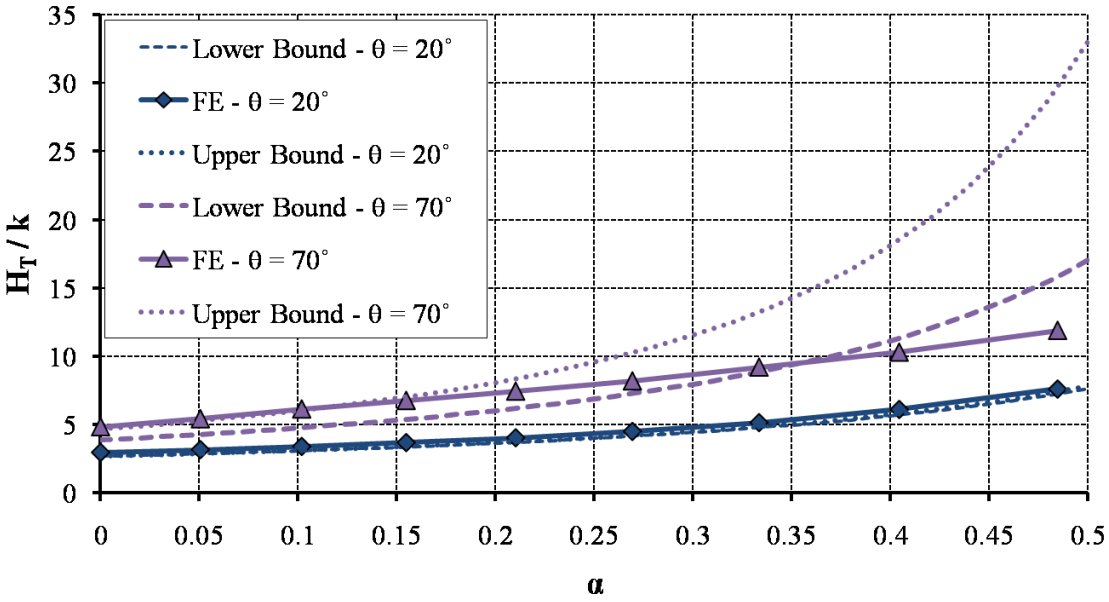

Figure 4-17: Hardness–to–shear strength ratio vs. Drucker-Prager friction coefficient α. Comparison of lower bound, upper-bound, and FE solutions for $\theta = 20°, 70°$.

an underestimation of the hardness for greater values of α. Here again, it is impossible to refine the models to a better accuracy for the lower or upper bound solutions since these FE results are consistent with neither solution.

4.3.3 Influence of the Blade–Material Interface Friction

The Amonton type law of friction can be implemented in Abaqus. The FE model can help us in validating the values obtained when friction is taken into consideration. Once again, there is a very good correlation between the lower bound approximation and the FE simulation as shown on Figure 4-18 for a Von Mises material. The existence of a critical $\mu_i^{cr}(\theta)$ above which increasing the friction coefficient does not affect the tangential hardness is clearly apparent, but its value differs from the one obtained with the lower bound approximation ($\mu_i^{cr,FE}(\theta = 20°) \approx \mu_i^{cr,FE}(\theta = 70°) \approx 0.2$ while $\mu_i^{cr,LB}(\theta = 20°) = 0.167$ and $\mu_i^{cr,LB}(\theta = 70°) = 0.282$).

In actual scratch tests, both F_T and F_V are measured. While the frictionless assumption imposes that $F_V/F_T = \tan\theta$ whatever the scratched material, the consideration of interface friction allows this ratio to depart from this value of $\tan\theta$ in a

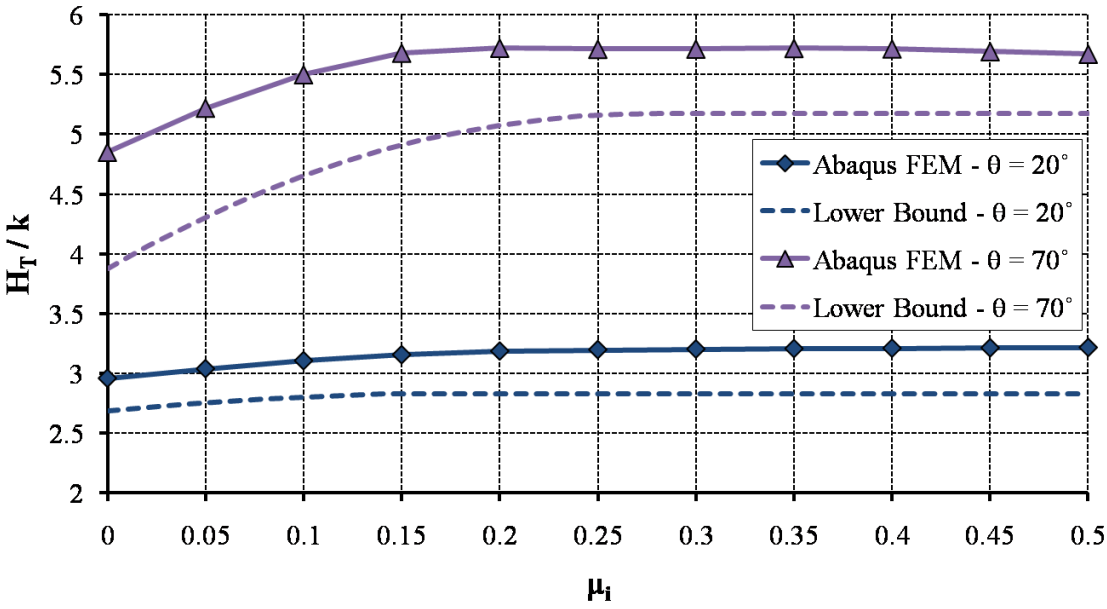

Figure 4-18: Hardness–to–shear strength ratio vs. interface friction coefficient μ_i for a Von Mises material. Comparison of lower bound and FE solutions for $\theta = 20°, 70°$.

material-dependent way. Both the lower bound model and the FE simulation predict two separate regimes for this ratio F_T/F_V as shown on figure 4-19:

- for $\mu_i < \mu_i^{cr}$, sliding occurs at the interface and the friction law is saturated: $|\sigma_t| = -\mu_i \sigma_n$. By means of geometric consideration, a direct relationship between the force ratio and the friction coefficient can be inferred in the framework of the lower bound model:

$$\frac{F_V}{F_T} = \frac{\sin\theta + \mu_i \cos\theta}{\cos\theta - \mu_i \sin\theta} \Leftrightarrow \mu_i = \frac{\cos\theta \, \frac{F_V}{F_T} - \sin\theta}{\cos\theta + \sin\theta \, \frac{F_V}{F_T}} \tag{4.25}$$

  Measuring the ratio F_V/F_T in this regime gives access to the friction coefficient μ_i.

- for $\mu_i > \mu_i^{cr}$, static friction takes place, meaning that there is adhesion of the material to the blade. In this case, relationship 4.5 cannot be used and the measurement of F_V/F_T does not bring more information than the fact that $\mu_i > \mu_i^{cr}$.

Relationship 4.5 is *a priori* purely geometric and the fact that the FE simulation is

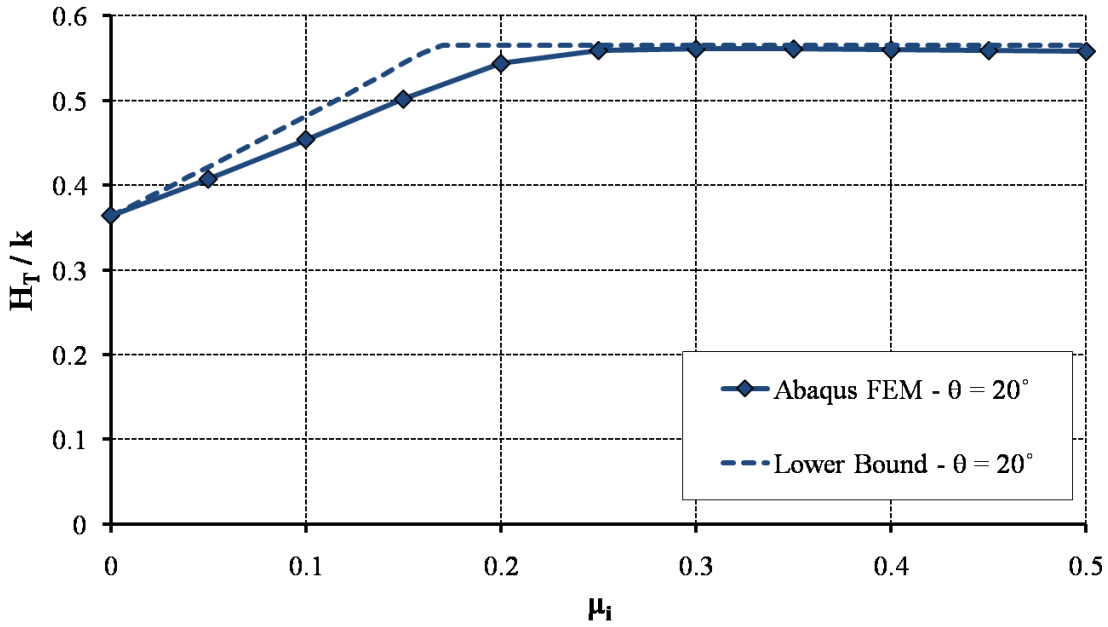

Figure 4-19: F_V/F_T ratio vs. interface friction coefficient μ_i for a Von Mises material. Comparison of lower bound and FE solutions for $\theta = 20°$.

not perfectly correlated hints toward the existence of a mixed-regime in which the contact area is divided in a region of adhesion and a region of sliding. The fraction of adhesive area progresses from 0 to 1 with the increase of μ_i, whereas it is an on/off phenomenon (at $\mu_i = \mu_i^{cr}$ in the lower bound model in which stress field is constant under the blade).

4.3.4 Qualitative Comparisons of the Solutions

The overall good agreement between the lower bound and the FEM solutions is attributable to the form of the stress field that develops in the immediate surrounding of the blade–material interface (Figure 4-20), which appears to be well approximated by the rough but accurate stress fields (3.19) considered in our lower bound approach. The measured hardness depends only on the state of stress at the blade–material interface, thus the ability of the model to approximate the stress field in this particular location is key to the good prediction of the hardness.

For the $\theta = 20°$ geometry, the upper bound also shows a very good correlation with the FE results. The upper bound is based on the plastic dissipation of energy that

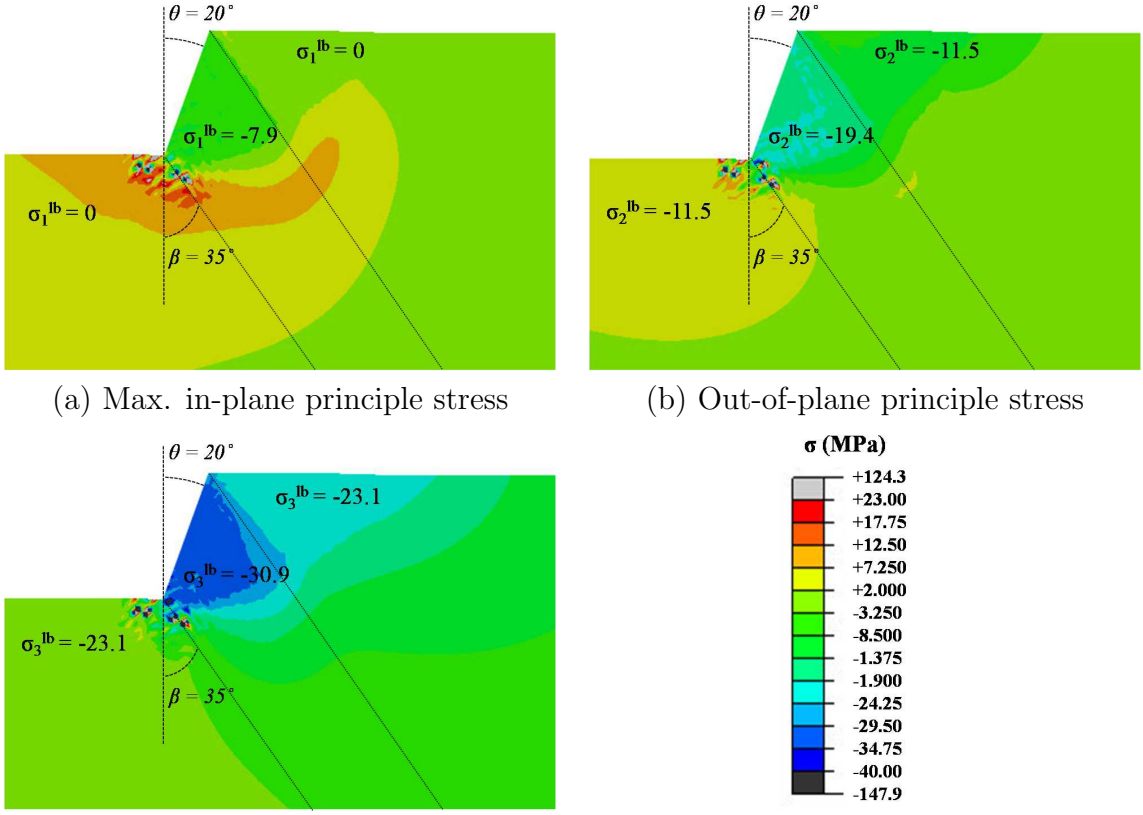

(a) Max. in-plane principle stress

(b) Out-of-plane principle stress

(c) Min. in-plane principle stress

Figure 4-20: Principle stresses of the FE simulation for a Von Mises material with $\theta = 20°$ and $k = 11.5$MPa. The values expected with the lower bound solution are superimposed.

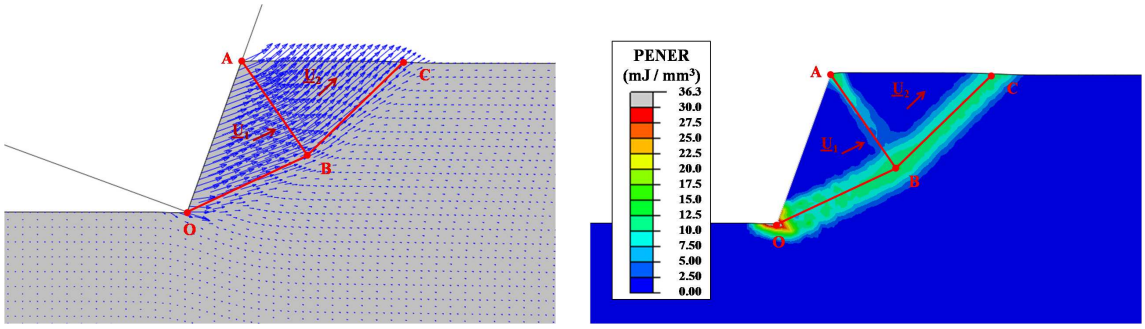

(a) Displacement field (b) Plastic Dissipation

Figure 4-21: Correlation between the upper bound optimization solution (superimposed in red) and the FE simulation for a Von Mises criterion and $\theta = 20°$.

occurs on the surfaces of discontinuity represented on figure 4-1. The good correlation of this model with the FE result may be explained by the proximity of the solution of these surfaces of discontinuity with the dissipation pattern observed in the FE simulation. Though continuous, the displacement field in the FE simulations is actually well approximated by surfaces of discontinuity as used in the upper bound model. Figure 4-21 shows indeed that the dissipation and velocity patterns are close to the yield design approximation.

In the $\theta = 70°$ case, the qualitative correlation is not as good, as shown on figure 4-22. For this geometry, the Von Mises solution of the upper bound approximation is however very close to the FE solution, whereas the velocity and dissipation patterns are not very well approximated by the simple discontinuities proposed in the upper bound model.

4.4 Chapter Summary

In this chapter we have compared the hardness–cohesion–friction solutions obtained with the lower bound approach to three different approaches: a simple upper-bound approach based on velocity discontinuities, an advanced upper bound limit analysis solver, and elastoplastic finite element simulations carried out for two geometries with Abaqus. The correlation with the lower bound solutions and the other approaches is very good, especially for small angles θ, for which the solution for the frictionless 2D

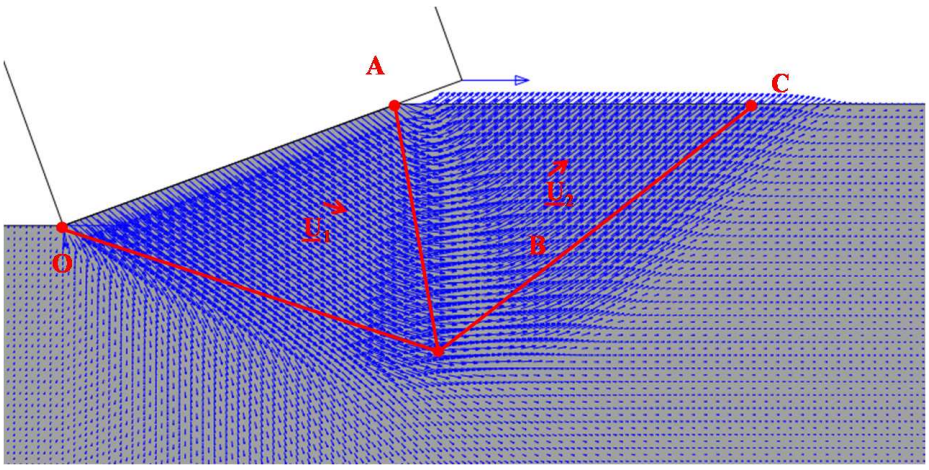

(a) Displacement field

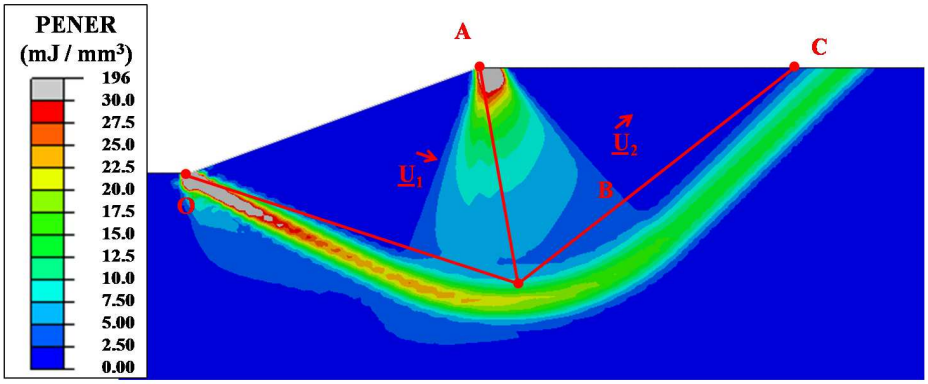

(b) Plastic Dissipation

Figure 4-22: Correlation between the upper bound optimization solution (superimposed in red) and the FE simulation for a Von Mises criterion and $\theta = 70°$.

problem is found with an accuracy of 1%. It proves then that the relations found with the lower bound approach are correct, provided the intial hypotheses are verified. A comparison to experimental values is now required to test the hypotheses. This is the focus of the next part of this thesis.

Part III

Extension and Application of the Strength Model

Chapter 5

Porous Materials

The striking feature of the lower bound model developed in Chapter 3 for cohesive-frictional materials and validated by two upper bound models and elastoplastic finite element simulations in Chapter 4, is its simplicity. In this chapter, we take advantage of this simplicity to extend its fields of application to more complex materials. Most geomaterials are porous [38], which must be accounted for in the modeling of their behaviors. We use here the strength criterion for porous cohesive-frictional materials developed by Ortega, Gathier and Ulm [43]. Carrying out the lower bound analysis with this new strength criterion leads us to relations between hardness, porosity and strength properties of the material similar to the relations recently derived for indentation hardness [16],[25],[44].

5.1 Strength Criterion

We consider the porosity through the use of the strength criterion developed by Ortega, Gathier, and Ulm [43] based on the Linear Comparison Composite theory [17] to upscale strength properties from the mesoscopic to the macroscopic level. In this paragraph we define the parameters entering the homogenization procedure. For a detailed development of the strength homogenization procedure, the reader is referred to Ref. [43] and [26]. Consider a material whose macroscopic representative elementary volume (*rev*) is a heterogeneous material composed of a solid phase and

pores (Figure 5-1). The volume fraction of the solid phase $\eta = V_s/V$ is called the packing density. It is related to the porosity (volume fraction of the pores) $\phi = V_p/V$ by the simple relation:

$$\eta = 1 - \phi \tag{5.1}$$

To apply continuum mechanics theory at the macroscale, a homogeneous equivalent to this heterogeneous rev must be found. The two input parameters for this specific case of strength homogenization are:

- the strength criterion of the solid phase $f(\underline{\underline{\sigma}}) \leqslant 0$.
- the morphology of the rev. Two microstructures are considered (Figure 5-1). The first one relates to a solid matrix–pore inclusion morphology. The homogenization scheme that represents it best is the so-called Mori-Tanaka scheme [40]. This matrix–inclusion composite can develop a mechanical response for the entire range of solid concentrations ($\eta \in [0, 1]$). The second case relates to a highly disordered composite, in which no phase can play the role of matrix or inclusion. This morphology is captured by the self-consistent scheme, which originated independently from Hershey [30] and Kroener [34]. When applied to a two-phase composite made of a solid phase and pores, it is characterized by a percolation threshold η_0 which is the solid concentration under which the composite material shows no strength at all and therefore cannot produce any mechanical response to loading.

The solid phase is chosen to be a cohesive-frictional material represented by the Drucker-Prager criterion:

$$f(\underline{\underline{\sigma}}) = \sqrt{\sigma_d} + \alpha\sigma_m - k_s \leqslant 0 \tag{5.2}$$

where $\sigma_m = \frac{1}{3}\mathrm{tr}\underline{\underline{\sigma}} = \frac{\sigma_I+\sigma_{II}+\sigma_{III}}{3}$ is the mean stress while $\sigma_d = \sqrt{\frac{1}{2}\underline{\underline{s}} : \underline{\underline{s}}}$ is the deviatoric stress, and $\underline{\underline{s}} = \underline{\underline{\sigma}} - \sigma_m\underline{\underline{1}}$. The application of the homogenization procedure requires a strictly convex strength domain. This is not the case of the Drucker-Prager strength criterion (5.2), which in addition exhibits a point of singularity ($\sigma_m = k_s/\alpha$, $\sigma_d = 0$).

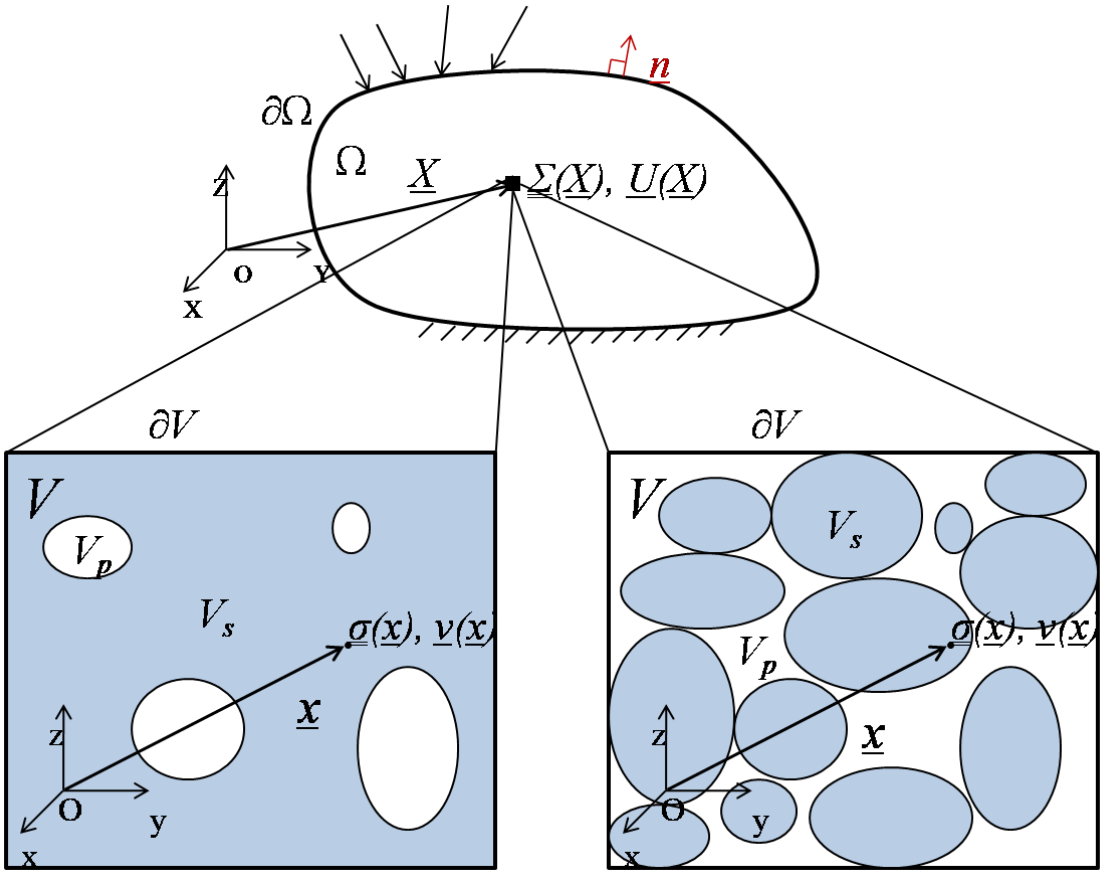

Figure 5-1: Formalism and nomenclature used for a porous material. The rev of the macroscopic problem (top) is itself heterogeneous (bottom) as it is constituted of a solid phase and pores. Left: schematic of the matrix–pore morphology; Right: disordered granular material morphology.

A family of regular hyperbolic criteria is used to circumvent this drawback:

$$f(\underline{\underline{\sigma}}) = 1 - \frac{(\sigma_m - \sigma_0)^2}{A} + \frac{\sigma_d^2}{B} \leqslant 0 \tag{5.3}$$

This criterion tends to the Drucker-Prager criterion when:

$$\begin{cases} B = \alpha^2 A \\ \sigma_0 = \frac{k_s}{\alpha} \\ A \to 0 \end{cases} \tag{5.4}$$

The homogenization procedure yields the following dissipation function for the Drucker-Prager case in consideration:

$$\Pi^{hom}(\underline{\underline{D}}) = \Sigma_0^{hom} D_v + \text{sign}\,(\mathcal{B}) \sqrt{\mathcal{A} D_v^2 + 4\mathcal{B} D_d^2} \tag{5.5}$$

$$\text{with } \mathcal{A} D_v^2 + 4\mathcal{B} D_d^2 \geqslant 0 \tag{5.6}$$

where $D_v = \text{tr}\ \underline{\underline{D}}$ and $D_d = \sqrt{\frac{1}{2}\underline{\underline{\Delta}} : \underline{\underline{\Delta}}}$ are the first two invariants of the strain rate tensor and $\underline{\underline{\Delta}} = \underline{\underline{D}} - \frac{1}{3} D_v \underline{\underline{1}}$, and with:

$$\frac{\mathcal{A}}{k_s^2} = \frac{\eta^2 \mathcal{K} \left(\eta - \alpha^2 \mathcal{K}\right)}{\left(\eta - 2\alpha^2 \mathcal{K}\right)^2} \ ; \ \frac{\mathcal{B}}{k_s^2} = \frac{\eta \mathcal{M} \left(\eta - \alpha^2 \mathcal{K}\right)}{\eta - 2\alpha^2 \mathcal{K}} \ ; \ \frac{\Sigma^{hom}}{k_s} = \frac{\eta \alpha \mathcal{K}}{2\alpha^2 \mathcal{K} - \eta} \tag{5.7}$$

where $\mathcal{K}$ and $\mathcal{M}$ are the morphology factors whose estimations in the Mori-Tanaka (5.8) and Self-Consistent (5.9) schemes read as:

$$\mathcal{K}^{MT} = \frac{4\eta}{3(1-\eta) + 4\alpha^2} \ ; \ \mathcal{M}^{MT} = \frac{\eta(9 + 8\alpha^2)}{15 - 6\eta + (20 - 12\eta)\alpha^2} \tag{5.8}$$

$$\begin{aligned} &\mathcal{K}^{SC} = \tfrac{4\eta \mathcal{M}^{SC}}{4\alpha^2 \mathcal{M}^{SC} + 3(1-\eta)} \ ; \\ &\mathcal{M}^{SC} = \tfrac{1}{2} - \tfrac{5}{4}(1-\eta) - \tfrac{3}{16\alpha^2}(2+\eta) \\ &\quad + \tfrac{1}{16\alpha^2} \sqrt{144(\alpha^4 - \alpha^2) - 480\alpha^4\eta + 400\alpha^4\eta^2 + 408\alpha^2\eta - 120\alpha^2\eta^2 + 9(2+\eta)^2} \end{aligned} \tag{5.9}$$

The existence of a percolation threshold in the self-consistent case is contained in relations (5.9): for $\eta \to 0.5, \eta > 0.5$, $\mathcal{K}^{SC}, \mathcal{M}^{SC} \to 0$. This yields a material with no strength for packing densities smaller than $\eta_0 = 0.5$. In contrast, the matrix–pore morphology yields an actual strength for any packing density greater than $\eta_0 = 0$.

Finally, we use the yield design definition that links stresses to the dissipation function at yield:

$$\underline{\underline{\Sigma}} = \frac{\partial \Pi^{hom}}{\partial \underline{\underline{D}}};\ \Sigma_m = \frac{1}{3}\mathrm{tr}\ \underline{\underline{\Sigma}} = \frac{\partial \Pi^{hom}}{\partial D_v};\ \Sigma_d = \sqrt{\frac{1}{2}\underline{\underline{S}} : \underline{\underline{S}}} = \frac{1}{2}\frac{\partial \Pi^{hom}}{\partial D_d} \tag{5.10}$$

where $\underline{\underline{S}} = \underline{\underline{\Sigma}} - \Sigma_m \underline{\underline{1}}$ is the macroscopic deviatoric stress tensor. The application of (5.10) to (5.5) yields the relation defining the boundary of the strength domain G^{hom}:

$$\underline{\underline{\Sigma}} \in \partial G^{hom} \Leftrightarrow \frac{\left(\Sigma_m - \Sigma_0^{hom}\right)^2}{\mathcal{A}} + \frac{\Sigma_d^2}{\mathcal{B}} = 1 \tag{5.11}$$

It is recognized that the sign of $\mathcal{B}$ determines whether the homogenized strength criterion is an elliptical ($\mathcal{B} > 0$) or a hyperbolic criterion ($\mathcal{B} < 0$) (Figure 5-3). The strength domain is thus represented by the function $\mathcal{F}$ defined as:

$$\boxed{\mathcal{F}(\underline{\underline{\Sigma}}) = \mathrm{sign}(\mathcal{B}) \left(\frac{\left(\Sigma_m - \Sigma_0^{hom}\right)^2}{\mathcal{A}} + \frac{\Sigma_d^2}{\mathcal{B}} - 1 \right) \leqslant 0} \tag{5.12}$$

For a given internal friction coefficient α of the solid phase there exists a critical packing density η_{cr} bellow which $\mathcal{B} < 0$ and above which $\mathcal{B} > 0$. This critical packing density depends on the homogenization scheme (MT or SC):

$$0 \leqslant \eta_{cr}^{MT} = 1 - \frac{4}{3}\alpha^2 \leqslant 1 \tag{5.13}$$

$$\frac{2}{3} \leqslant \eta_{cr}^{SC} = 1 - \frac{\sqrt{1216\alpha^4 + 432\alpha^2 + 81} - (16\alpha^2 + 9)}{2(20\alpha^2 + 3)} \leqslant 1 \tag{5.14}$$

It is worthwhile to note that condition (5.6) is the translation of the compatibility of the velocity field with the flow rule (4.2). It is always satisfied in the elliptical regime for which $(\mathcal{A}, \mathcal{B}) > 0$, but must be imposed in the hyperbolic case and leads

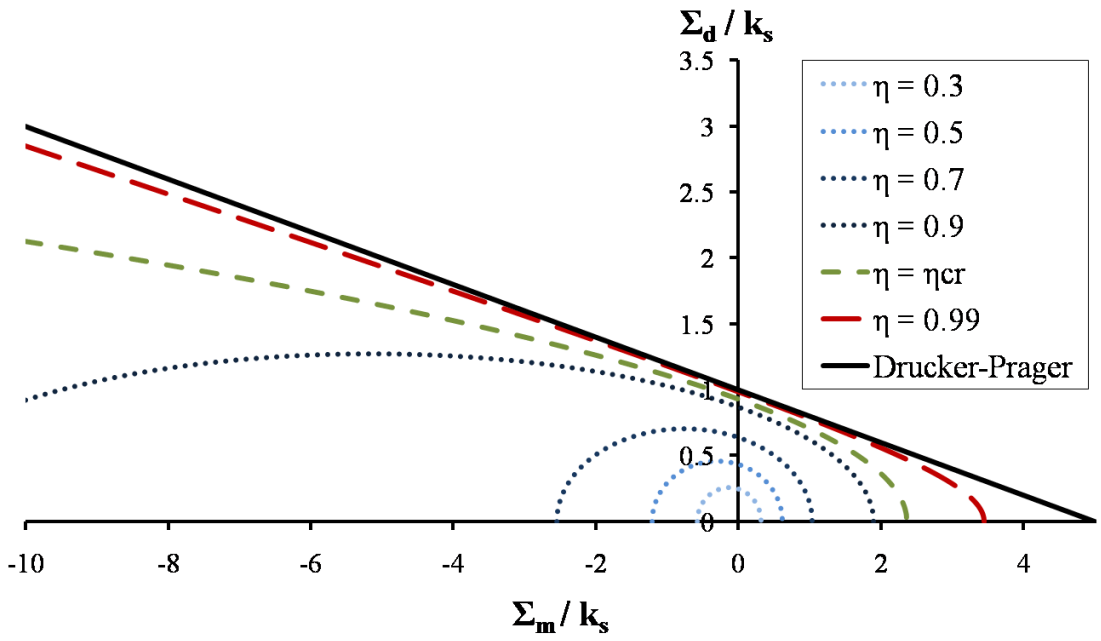

Figure 5-2: Homogenized strength criterion for $\alpha_s = 0.2$. It is elliptical for $\eta < \eta_{cr}$, parabolic for $\eta = \eta_{cr}$, and hyperbolic for $\eta > \eta_{cr}$.

to convergence difficulties when implemented in an optimization algorithm.

For $\eta \to 1$ the hyperbolic criterion tends toward the Drucker-Prager criterion of the solid phase, which of course is necessary for the consistency of the model. This is illustrated on Figure 5-3. In the same way, the homogenized support function $\Pi^{hom}(\underline{\underline{\Sigma}})$ (5.5) and its flow rule compatibility condition (5.5) tend toward the expression of the power function of the Drucker-Prager criterion (4.19)[53].

Our upper bound model relies on velocity discontinuities. The support function (5.5) needs therefore to be adapted to encompass these discontinuities. Consider a velocity discontinuity $\underline{V}$ along a surface oriented by $\underline{n}$ in a material whose support function is $\Pi^{hom}(\underline{\underline{D}})$. In the local coordinate system of the discontinuity, one can write: $\underline{V} = V_n\ \underline{n} + V_{t1}\ \underline{t}_1 + V_{t2}\ \underline{t}_2$, where $\underline{t}_1$ and $\underline{t}_2$ are two orthonormal vectors in the discontinuity plane. It can be shown [53] that the support function for such a velocity discontinuity is related to the power function for an equivalent bulk strain rate:

$$\Pi^{hom}(\underline{n}, \underline{V}) = \Pi^{hom}\left(\underline{\underline{\hat{D}}}(\underline{n}, \underline{V})\right) \tag{5.15}$$

where $\underline{\underline{\hat{D}}}(\underline{n},\underline{V}) = V_n \underline{n}\otimes\underline{n} + \frac{V_{t1}}{2}\left(\underline{n}\otimes\underline{t}_1 + \underline{t}_1\otimes\underline{n}\right) + \frac{V_{t2}}{2}\left(\underline{n}\otimes\underline{t}_2 + \underline{t}_2\otimes\underline{n}\right)$ is the equivalent strain rate tensor. Its invariants are:

$$\hat{D}_v = V_n = \underline{V}\cdot\underline{n}\ ;\ \hat{D}_d = \frac{1}{2}\sqrt{|\underline{V}|^2 + \frac{1}{3}V_n^2} = \frac{1}{2}\sqrt{\underline{V}\cdot\underline{V} + \frac{1}{3}(\underline{V}\cdot\underline{n})^2} \tag{5.16}$$

which yields the support function for a velocity discontinuity:

$$\boxed{\Pi^{hom}\left(\underline{n},\underline{V}\right) = \Sigma_0^{hom}\underline{V}\cdot\underline{n} + \text{sign}\left(\mathcal{B}\right)\sqrt{\left(\mathcal{A}+\tfrac{1}{3}\mathcal{B}\right)\left(\underline{V}\cdot\underline{n}\right)^2 + \mathcal{B}\underline{V}\cdot\underline{V}}} \tag{5.17}$$

$$\text{with}\ \left(\mathcal{A}+\frac{1}{3}\mathcal{B}\right)\left(\underline{V}\cdot\underline{n}\right)^2 + \mathcal{B}\underline{V}\cdot\underline{V} \geqslant 0 \tag{5.18}$$

One can easily verify that this expression reduces to $\pi(\underline{n},\underline{V}) = \frac{k_s}{\alpha}\underline{V}\cdot\underline{n}$ with $\left(\underline{V}\cdot\underline{n}\right)^2 \geqslant \underline{V}\cdot\underline{V}\sqrt{\frac{\alpha^2}{1-\alpha^2/3}}$ when $\eta \to 1$, which is the support function expression for the Drucker-Prager criterion (4.19).

5.2 Hardness–to–Shear Strength Relationships

5.2.1 Analytical Development of the Lower Bound Model for Frictionless Interface

We follow the same procedure as in section 3.4 to find analytical expressions of the hardness–to–strength ratio for porous cohesive-frictional materials represented by the homogenized strength criterion (5.12). The static admissibility of the stress field (3.40) is still valid. As a consequence, the extremal principle stresses Σ_I and Σ_{III} depend only on H_T and the angle β. To obtain the maximum hardness reachable with our shape of stress field, we must choose the out-of-plane stress components σ_y and σ_y^{II} of the stress tensors in zones I and II so as to minimize the strength function $\mathcal{F}(\underline{\underline{\sigma}})$. A minimization of $\mathcal{F}(\sigma_I,\sigma_{II},\sigma III)$ yields:

$$\sigma_{II}^0(\Sigma_I,\Sigma_{III}) = \mathcal{C}\frac{\sigma_I+\sigma_{II}}{2} + (1-\mathcal{C})\Sigma_0^{hom} \tag{5.19}$$

where $\mathcal{C} = \frac{3\mathcal{A}-2\mathcal{B}}{3\mathcal{A}+\mathcal{B}}$. Inserting this value in the strength function to get the minimum value of $\mathcal{F}$ for given Σ_I,Σ_{III} yields:

$$\mathcal{F}(\Sigma_I, \Sigma_{II}^0, \Sigma_{III}) = \mathcal{D}\left(\frac{\Sigma_I + \Sigma_{III}}{2} - \frac{\mathcal{E}}{\mathcal{D}}\right)^2 - \frac{\Sigma_I \Sigma_{III}}{\mathcal{B}} - \left(\frac{\mathcal{E}}{\mathcal{D}}\right)^2 - \mathcal{H} \tag{5.20}$$

with $\mathcal{D} = (4-\mathcal{C}^2)\left(\frac{1}{9\mathcal{A}}\right)$, $\mathcal{E} = \left(\frac{1}{9\mathcal{A}} + \frac{1}{3\mathcal{B}}\right)\mathcal{C}\Sigma_0^{hom}(1-\mathcal{C}) + \frac{2\Sigma_0^{hom}}{3\mathcal{A}}$, and $\mathcal{H} = \left(\frac{1}{9\mathcal{A}} + \frac{1}{3\mathcal{B}}\right)(1-\mathcal{C})^2\left(\Sigma_0^{hom}\right)^2 + 1 - \frac{\left(\Sigma_0^{hom}\right)^2}{\mathcal{A}}$.
The optimum angle β is found by letting:

$$\mathcal{F}(\underline{\underline{\Sigma}}^I) = \mathcal{F}(\underline{\underline{\Sigma}}^{II}) \tag{5.21}$$

Letting then the strength function be equal to 0 in both domains yields the maximum hardness. However, the presence of the coupling term $\frac{\Sigma_I \Sigma_{III}}{\mathcal{B}}$ in (5.20) makes (5.21) a fourth order equation of $\tan\beta$ whose general solution cannot be found. As a consequence, like in the case with interface friction, we propose numerical solution as closed-form analytical solutions for the hardness–to–strength relationship of porous cohesive-frictional materials cannot be derived.

5.2.2 Optimization Results

The implementation of the homogenized strength criterion in the optimization code developed for the frictional case (see Appendix A) consists in changes in the non-linear conditions representing the strength compatibility in zones I and II, using the strength criterion (5.12). For the upper bound model, the support function (5.17) is implemented in the calculation of the dissipated energy. In the hyperbolic case ($\eta > \eta_{cr}$), condition (5.18) is applied as a non-linear constraint. We can now predict the hardness–to–shear strength ratio for any angle θ, internal friction coefficient α, porosity $\varphi = 1 - \eta$, morphology (MT or SC), and interface friction μ_i. For $\theta = 20°$, the yield design solver developed by Borges is used as a validation tool but converges only in the elliptical case $\eta < \eta_{cr}$. The upper bound model proposed in this thesis also has convergence problems in the hyperbolic case, for which the initializing of the

optimization parameters needs to be very close to the solution. As a result, the lower bound model can only be validated by the upper bound models in the elliptical case. As displayed on figures 5-3 and 5-4 the correlation between upper bound and lower bound solutions is very good for small packing densities. As expected the solutions converge to the solid Drucker-Prager values when $\eta \to 1$.

5.2.3 Function Fitting for the Frictionless Case

It is possible to derive fitting functions that summarize the discrete simulation results in closed form expressions to be used for data analysis. The format of the scaling relations is chosen in the following form:

$$\frac{H_T}{k_s} = h_s(\theta, \alpha, k_s)\Pi\left(\theta, \alpha, \eta, \eta_0\right) \tag{5.22}$$

where $h_s(\theta, \alpha, k_s)$ is the hardness of the Drucker-Prager solid whose expression was derived analytically in chapter 3 (3.48), and $\Pi\left(\theta, \alpha, \eta, \eta_0\right)$ captures the influence of the porosity and the morphology of the composite material (MT or SC) and must satisfy $\Pi\left(\theta, \alpha, \eta = 1, \eta_0\right) = 1$. For a given packing density and scheme, the Π-function is well approximated by a function of the shape $a\alpha^2 + c$. We hence propose the following decomposition of Π:

$$\Pi(\theta, \alpha, \eta, \eta_0) = \Pi_1(\theta, \eta, \eta_0) + \alpha^2\Pi_2(\theta, \eta, \eta_0) \tag{5.23}$$

Due to the complexity of the optimization, we fit functions for given geometries only and do not propose any general dependence on θ for Π_1 and Π_2. To illustrate the procedure, we fit functions for two geometries: $\theta = 15^\circ$ and $\theta = 70^\circ$. $\theta = 15^\circ$ is a geometry commonly used for the testing of rocks [50]. $\theta = 70^\circ$ is the typical back-rake angle obtained when using other geometries such as spherical indenter [7] [35] and is used to show the relevance of the shape functions.

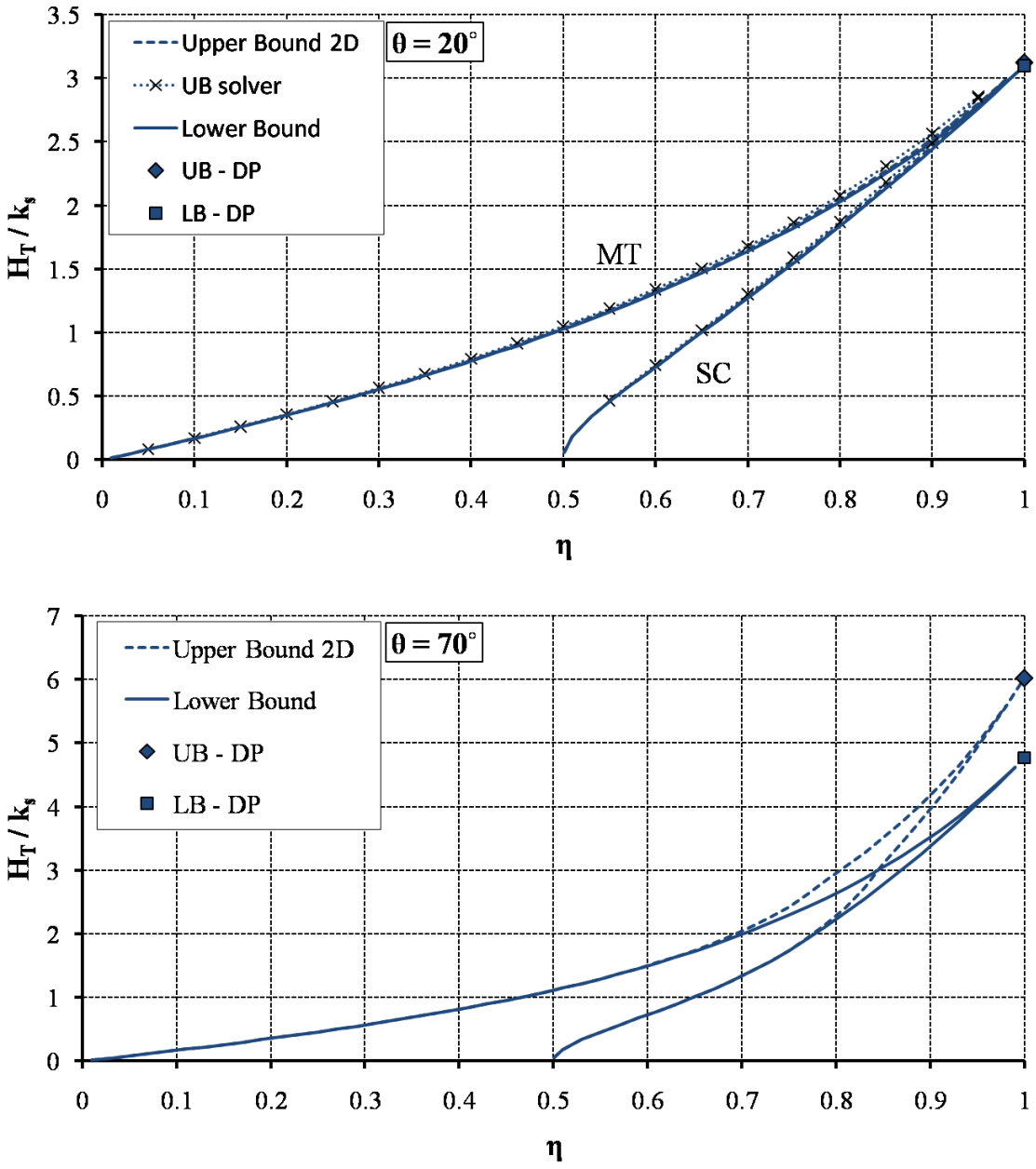

Figure 5-3: Hardness normalized by solid shear strength versus packing density η for $\alpha = 0.1$.

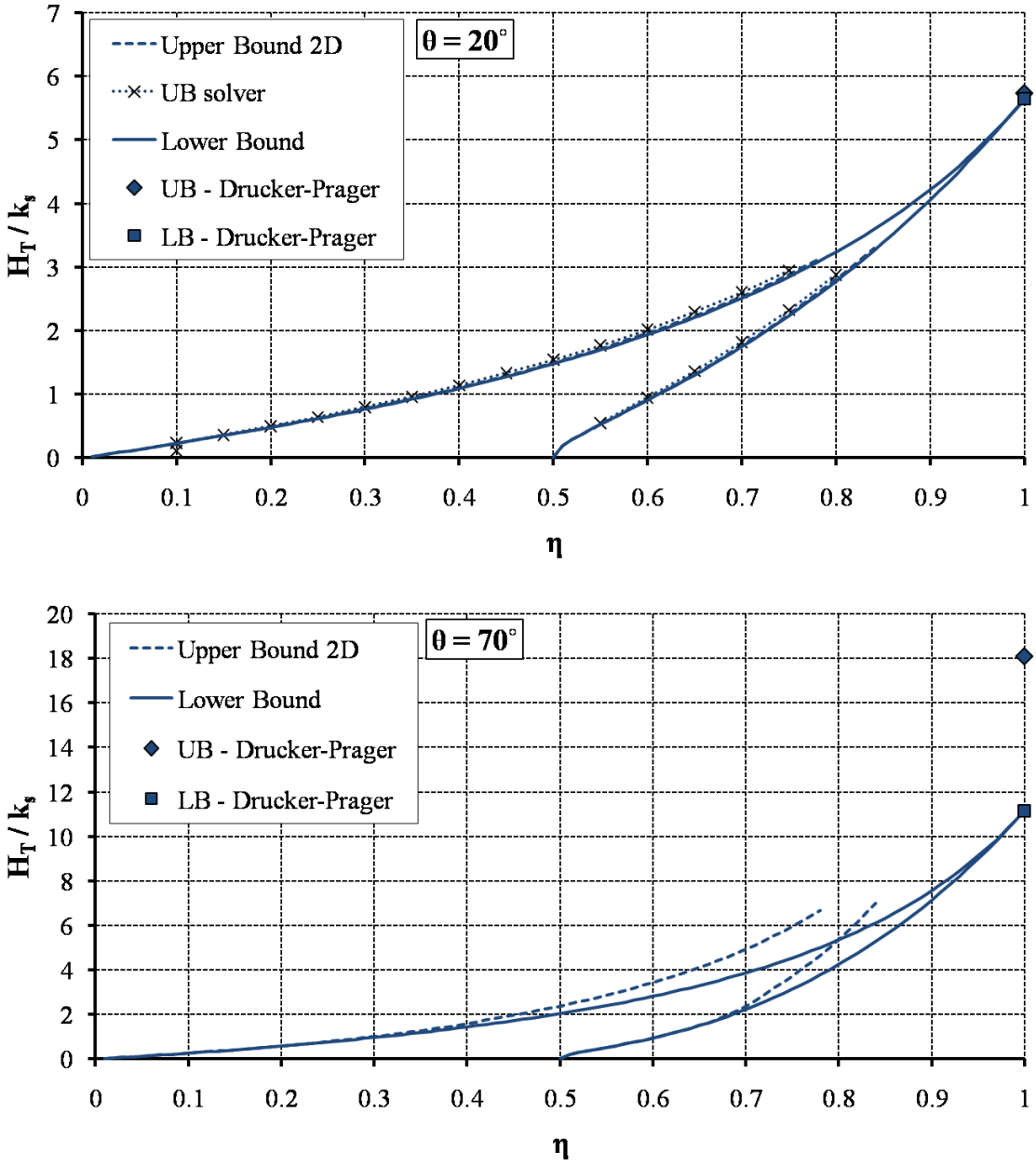

Figure 5-4: Hardness normalized by solid shear strength versus packing density η for $\alpha = 0.4$. The upper bound solutions fail to converge for $\eta > \eta_{cr}$ ($\eta_{cr}^{MT} = 0.787$, $\eta_{cr}^{SC} = 0.847$)

.

- For the Mori-Tanaka case, we use the following 8-parameter function:

$$\begin{cases} \Pi_{1,\theta}^{MT}(\eta) = \eta\,(1 + a_\theta(1-\eta) + b_\theta(1-\eta)^2 + c_\theta(1-\eta)^3) \\ \Pi_{2,\theta}^{MT}(\eta) = \eta(1-\eta)\,(d_\theta + e_\theta(1-\eta) + f_\theta(1-\eta)^2 + g_\theta(1-\eta)^3 + h_\theta(1-\eta)^4) \end{cases} \tag{5.24}$$

An application of the method of least squares on 808 discrete values of H_T/h_s ($\alpha = 0, 0.1, ..., 0.7$, $\eta = 0, 0.01, ..., 1$) for $\theta = 15^\circ, 70^\circ$ yields the parameters $a, b, ..., h$:

$$\text{MT}, \theta = 15^\circ \begin{cases} a_{15^\circ} = -0.9062 & e_{15^\circ} = 14.8919 \\ b_{15^\circ} = 0.8711 & f_{15^\circ} = -11.4005 \\ c_{15^\circ} = -0.4089 & g_{15^\circ} = -5.9572 \\ d_{15^\circ} = -6.2702 & h_{15^\circ} = 8.3834 \end{cases} \tag{5.25}$$

$$\text{MT}, \theta = 70^\circ \begin{cases} a_{70^\circ} = -1.9405 & e_{70^\circ} = 21.1757 \\ b_{70^\circ} = 2.4411 & f_{70^\circ} = -19.1115 \\ c_{70^\circ} = -1.1720 & g_{70^\circ} = -8.9584 \\ d_{70^\circ} = -7.0391 & h_{70^\circ} = 14.2613 \end{cases} \tag{5.26}$$

- For the self-consistent scheme, representing perfectly disordered granular material, we use a 7-parameter function:

$$\begin{cases} \Pi_{1,\theta}^{MT}(\eta) = \sqrt{2\eta - 1}\,(1 + a_\theta(1-\eta) + b_\theta(1-\eta)^2 + c_\theta(1-\eta)^3) \\ \Pi_{2,\theta}^{MT}(\eta) = \sqrt{2\eta - 1}(1-\eta)\,(d_\theta + e_\theta(1-\eta) + f_\theta(1-\eta)^2 + g_\theta(1-\eta)^3) \end{cases} \tag{5.27}$$

The method of least squares applied to 408 discrete values ($\alpha = 0, 0.1, ..., 0.7$, $\eta = 0.50, 0.51, ..., 1$) for $\theta = 15^\circ, 70^\circ$ yields the parameters $a, b, ..., g$:

$$\text{SC}, \theta = 15^\circ \begin{cases} a_{15^\circ} = -0.9246 & d_{15^\circ} = -6.0780 \\ b_{15^\circ} = -0.1948 & e_{15^\circ} = 4.9562 \\ c_{15^\circ} = -0.0612 & f_{15^\circ} = 3.1910 \\ & g_{15^\circ} = 1.5310 \end{cases} \tag{5.28}$$

$$\mathrm{SC}, \theta = 70^\circ \begin{cases} a_{70^\circ} = -2.1914 & d_{70^\circ} = -4.8556 \\ b_{70^\circ} = 1.2477 & e_{70^\circ} = 2.9409 \\ c_{70^\circ} = 0.8978 & f_{70^\circ} = 1.9639 \\ & g_{70^\circ} = 0.9572 \end{cases} \tag{5.29}$$

With relationships between packing density, cohesive-frictional strength parameters, and scratch hardness in place and well approximated by smooth, closed-form fitting functions, an inverse approach to analysis of scratch results is possible.

5.3 Chapter Summary

In this chapter, we implemented a homogenized strength criterion for cohesive-frictional porous materials in the lower bound model. The results given by the lower bound model are validated in the elliptical regime of the strength criterion by our upper bound model and Borges' model. A simple optimization procedure written for Matlab gives access to the prediction of the tangential hardness for any angle θ, solid properties (k_s, α), porosity ($\phi = 1 - \eta$), and interfacial friction coefficient μ_i. While it was not possible to obtain closed form relations between hardness and material properties like in the case of classical strength criteria, we were able to fit regular functions predicting the hardness in the frictionless case and for a fixed angle θ. These relations represent a first step towards the implementation of a reverse analysis procedure aimed at determining the mechanical properties of porous cohesive-frictional materials from scratch tests measurements.

Chapter 6

Application

This chapter illustrates how strength properties of a material can be inferred from experimental scratch data through the use of the hardness–strength relations given by the lower bound model. A set of force recordings of scratch tests carried out at different widths and depths on cement paste was provided by Schlumberger, along with the experimental value of the uniaxial compressive strength σ_0. Through the formulation of different hypotheses, we deduce the strength properties of the tested material.

6.1 Experimental Data

The overall satisfying comparison of the lower bound solutions with upper bound and finite-element solutions suggests that the simple closed-form solutions provide an accurate means to determine strength parameters from a scratch test. This is illustrated here for scratch results on cement pastes, the hydraulic binding phase of concrete materials. The material is a cement paste prepared at a water–to–cement mass ratio of 0.44. The uniaxial compressive strength (UCS) measured is $\sigma_0^{\text{exp}} = 43 \pm 2\text{MPa}$.

We here analyze three series of 20 scratch tests carried out on this cement paste material. The tests consist of cutting a groove of width w on the surface of a sample with a Polycrystalline Diamond Composites cubic cutter under controlled depth of

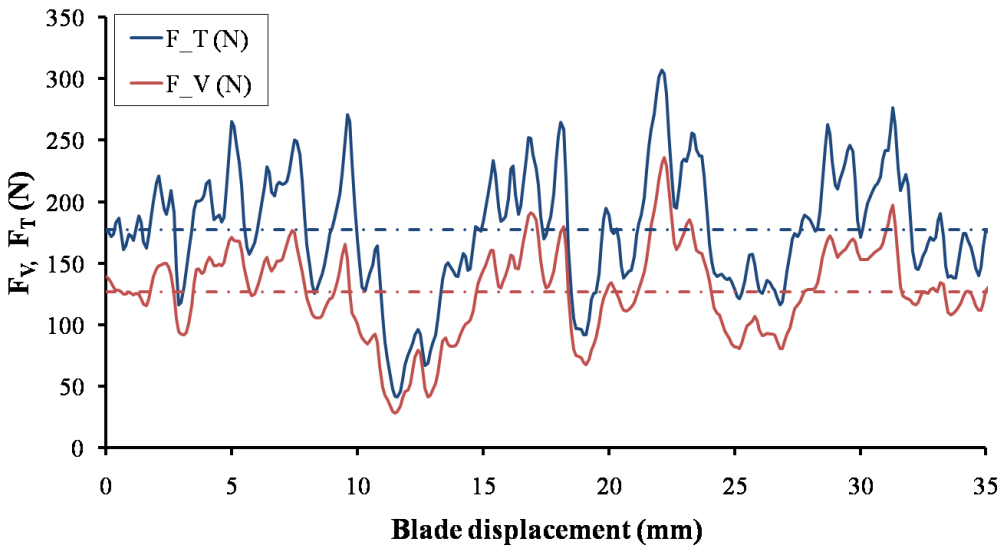

Figure 6-1: Example of scratch test result: measured vertical and normal forces along the scratch path [Test on cement paste, width $w = 10$ mm, depth $d = 0.5$ mm; tests carried out by Epslog Engineering (Belgium); data courtesy of Schlumberger].

cut d varying between 0.1 mm and 0.6 mm, and constant velocity. The back-rake angle in all tests was $\theta = 15°$. The three test series differ in the scratch width, $w = 2.5$ mm, 5 mm and 10 mm. In each scratch test, the mean tangential and vertical force is determined as the arithmetic mean of the forces recorded along the scratch path (Figure 6-1).

Figure 6-2 displays the range of mean tangential and vertical force values in all tests as a function of the projected contact area, $A_{LB} = wd$. The curved shape means that the scratch hardness in the sense of Eq. (1.1) is not a constant, but changes with the projected contact area. Such a dependency is indicative of size effects that cannot be explained by strength of materials theory. On the other hand, considering the hardness as the mean contact pressure, by analogy with classical mechanics-of-materials stress definition, one can define the scratch hardness asymptotically from the initial slope of the $F_T - A_{LB}$ curve:

$$H_S = \lim_{A_{LB}\to 0} \frac{F_T}{A_{LB}} = \left.\frac{\mathrm{d}F_T}{\mathrm{d}A_{LB}}\right|_{A_{LB}=0} \tag{6.1}$$

We thus fit the $F_T - A_{LB}$ curve with a 2nd order polynomial, to derive a scratch

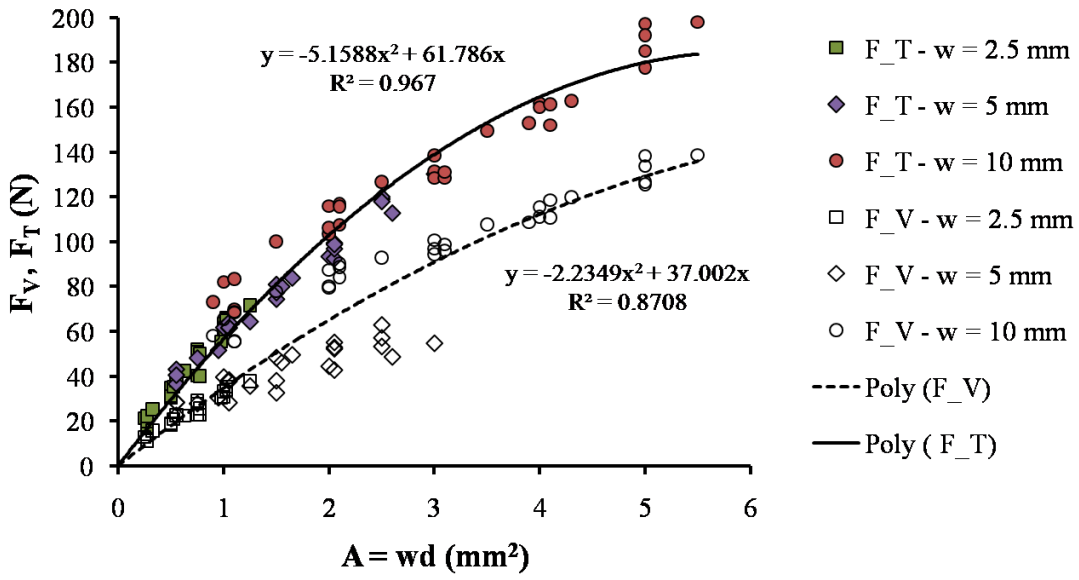

Figure 6-2: Tangential force F_T and vertical force F_V vs. Projected contact area $A = wd$ for scratch tests of different width w and depth d [Tests on cement paste; tests carried out by Epslog Engineering (Belgium); data courtesy of Schlumberger].

hardness of $H_S = 62$ MPa.

6.2 Characterization of the Material With the Lower Bound Model

We now want to link this scratch hardness to strength properties. We will here consider different cases, ranging from the simplest materials used in the model to the more advanced porous material presented in chapter 6.

6.2.1 Cohesive Material and Frictionless Contact

Let us assume that the material is a cohesive material of either the Tresca or the Von-Mises type. Assuming in addition frictionless interface conditions, a straightforward application of relations (3.45) for $\theta = 15^\circ$ yields a H_S/σ_0 ratio of 1.26 for the Tresca material and 1.45 for the Von Mises material. The corresponding compressive strengths are $\sigma_0 = 49$ MPa and $\sigma_0 = 43$ MPa, for the Tresca and Von Mises

Measurements		Mohr-Coulomb model		Drucker-Prager model	
UCS (MPa)	Hardness (MPa)	c (MPa)	φ	k (MPa)	α
41	62	12.0	29.4°	22.9	0.055
42	62	13.0	26.6°	23.9	0.022
43	62	14.1	23.5°	–	–
44	62	15.3	20.3°	–	–
45	62	16.7	16.9°	–	–

Table 6.1: Determination of the cohesion (resp. the shear strength) and the friction angle (resp. the friction coefficient) of the scratched material modeled by a Mohr-Coulomb (resp. Drucker-Prager) criterion.

case, respectively. Both values are not far off the experimental value of $\sigma_0^{\text{exp}} = 43 \pm 2$ MPa. However, the assumption of a purely cohesive material can be questioned, given that cement-based materials are known to exhibit an asymmetric strength behavior in tension and compression, indicative of a pronounced pressure sensitive strength behavior.

6.2.2 Cohesive-Frictional Material and Frictionless Contact

The material is a cohesive-frictional material of either the Mohr-Coulomb or the Drucker-Prager type. Assuming frictionless interface conditions, application of the closed-form solutions (3.46) and (3.48) require as input the scratch hardness-to-strength solution; that is: $H_S/\sigma_0^{\text{exp}} = 1.44 \pm 0.07$. Table 6.1 lists the values obtained by application of (3.46) and (3.48), showing a pronounced frictional behavior in the Mohr-Coulomb case and a low-to-zero pressure sensitivity for the Drucker-Prager case. Note that the Drucker-Prager characterization can be applied only for $H_S/\sigma_0 > 1.45$, which corresponds to the $\alpha = 0$ case (Von Mises).

6.2.3 Cohesive-frictional Material With Interface Friction

In both cases considered above, interface friction was neglected, which can be debated, given that the experimental force ratio $\lim_{A_{LB}\to 0} F_V/F_T = 0.60$ (Figure 6-2) is greater than $\tan(\theta = 15°) = 0.27$ expected in the frictionless case (see Eq. (3.52)). We thus shall assume interface friction following Amonton's Laws. If we assume that

Amonton's law (3.53) was saturated, such that $F_t = \mu_i F_n$, the tangential and vertical forces are related by (4.1), which is recalled here:

$$\frac{F_V}{F_T} = \frac{\sin\theta + \mu_i \cos\theta}{\cos\theta - \mu_i \sin\theta} \Leftrightarrow \mu_i = \frac{\cos\theta \, \frac{F_V}{F_T} - \sin\theta}{\cos\theta + \sin\theta \, \frac{F_V}{F_T}} \tag{6.2}$$

We thus obtain an interface friction coefficient $\mu_i = 0.285$. We then distinguish:

1. In the case of a Mohr-Coulomb criterion with interface friction, an application of the algorithm gives $c = 19.5$ MPa, and $\varphi = 5.5°$. We then determine the critical interface friction from (3.61), that is $\mu_i^{crit}(\varphi = 5.5°) = 0.24$, which is not far off the interface interface friction coefficient $\mu_i = 0.286$. This means that the interface criterion is at or close to saturation, as assumed in the determination of the interface friction coefficient (6.2).

2. In contrast, in the case of a Drucker-Prager material, the lowest value for the hardness-to-strength ratio predicted by the cohesive-frictional model for $\theta = 15°$ and $\mu_i = 0.286$ is $H_T/\sigma_0 = 1.56$, which is obtained for zero internal friction $\alpha = 0$. This predicted value is greater than the experimental value $H_S/\sigma_0^{\exp} = 1.44 \pm 0.07$; meaning that the Drucker-Prager model cannot explain the experimental observations.

6.2.4 Cohesive-Frictional Porous Material With Interface Friction

We have so far modeled the material as a homogeneous cohesive-frictional material. The model developed by Ortega, Gathier, and Ulm and presented in chapter 6 allows us to consider the porosity of the cement paste and have access to the properties of the solid phase. Comparing the density of the cement paste to the density of water and hydrated cement gives access to the porosity of the tested cement paste: $\phi = 0.33$, which is in close agreement with the value obtained from Mercury Intrusion Porosimetry (MIP) carried out on the same material [52]. The problem is hence to find a configuration (k_s, α, morphology) such that $H_T/\sigma_0 = 1.44$, $\sigma_0 = 43$ MPa,

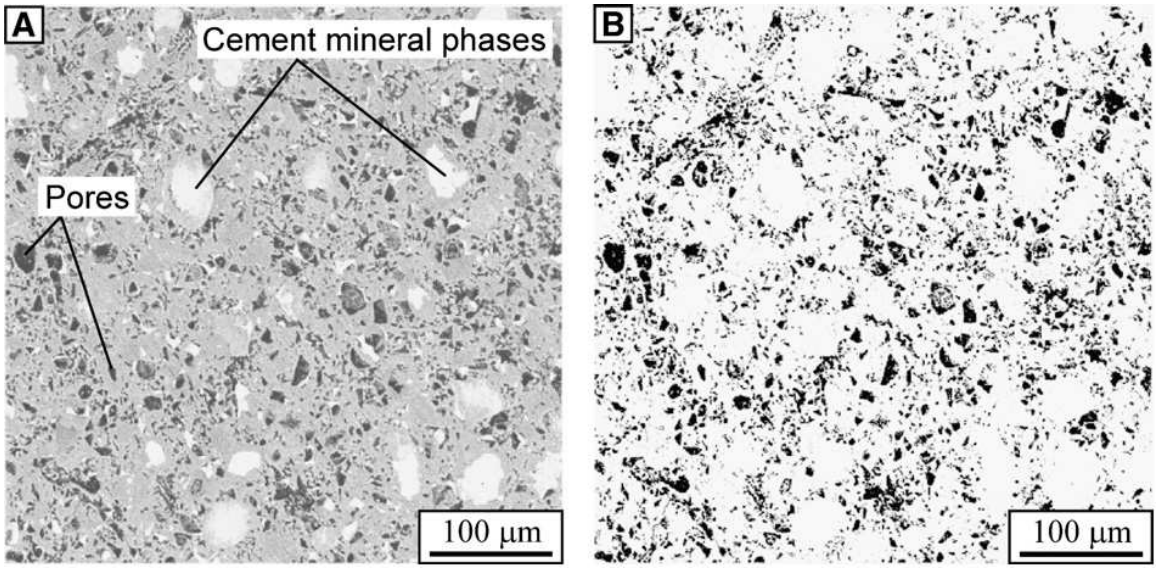

Figure 6-3: SEM-BSE image of Portland cement (A) and binarization of the initial grey-level BSE image (B) using the threshold tool of the image software. From [52].

$\eta = 1 - \phi = 0.67$, and $F_V/F_T = 0.60$. It is impossible to satisfy all these conditions with the model, mainly because the critical friction coefficient μ_i^{crit} is smaller than 0.285 in this configuration. As a result, F_V/F_T never reaches 0.60 in our model. One way of dealing with it is to assume that there is actually sliding at the interface. If we force the saturation of the law of friction, we reach $F_V/F_T = 0.60$ for $\mu_i = 0.286$, using relation (6.2). In such a case we can propose two different materials:

- Matrix–inclusion microstructure (Mori-Tanaka scheme): $k_s = 38$MPa, $\alpha = 0.195$.

- Granular microstructure (Self-Consistent scheme): $k_s = 43$Mpa, $\alpha = 0.452$.

Figure 6-3 shows an SEM image of the cement on which were carried the tests. At this scale the material exhibits a matrix–inclusion microstructure and would hence be best represented with the Mori-Tanaka scheme. However the matrix is not a homogeneous material. Its representation with a Drucker-Prager criterion can thus be argued.

6.3 Chapter Summary

The overall trend which emerges is that cement paste's pressure sensitive strength behavior is better captured by the Mohr-Coulomb criterion than by the Drucker-Prager criterion. The use of a material model including porosity gives access to the properties of the solid phase of a porous material, provided that its microstructure is known. This approach represents a way of acquiring micro-properties with an easy and relatively cheap macroscopic test. In addition, the approach is able to identify the presence of friction at the blade-material interface, for which (6.2) provides a first-order estimate, which could (and should) be refined by e.g. separate measurement of the interface friction. As such, the lower bound scratch hardness-strength solution with interface friction provides an upper bound estimate for the cohesion, and no-doubt a lower bound estimate of the internal friction.

Part IV

From a Strength to a Fracture Model

Chapter 7

Limits of Validity of the Strength Model

We have so far regarded the scratch test as a pure strength problem: neither elasticity nor fracture were considered. While finite element simulations hint toward a minor influence of the former, the latter has not been studied and is the subject of this chapter. We show here the limits of the strength interpretation by means of incompatible scale effects observed on experimental data. A finite element investigation of the possible influence of fracture is then presented to account for these scale effects.

7.1 Scale Effects

The tests on cement paste presented in chapter 6 exhibit a trend that cannot be explained by the strength model. Indeed, as depicted on figure 6-2, the tangential force F_T required to pull the blade through the material is not a linear function of the load-bearing contact area $A^{LB} = wd$. Yet, according to the dimensional analysis carried out in chapter 2, one should expect that $H_T = F_T/A^{LB}$ depends on the geometry only through dimensionless quantities θ and d/w (Eq. 2.9):

$$H_T = \sigma_0 \tilde{\Pi} \left(\frac{d}{w}, \theta, \alpha, \mu_i \right) \tag{7.1}$$

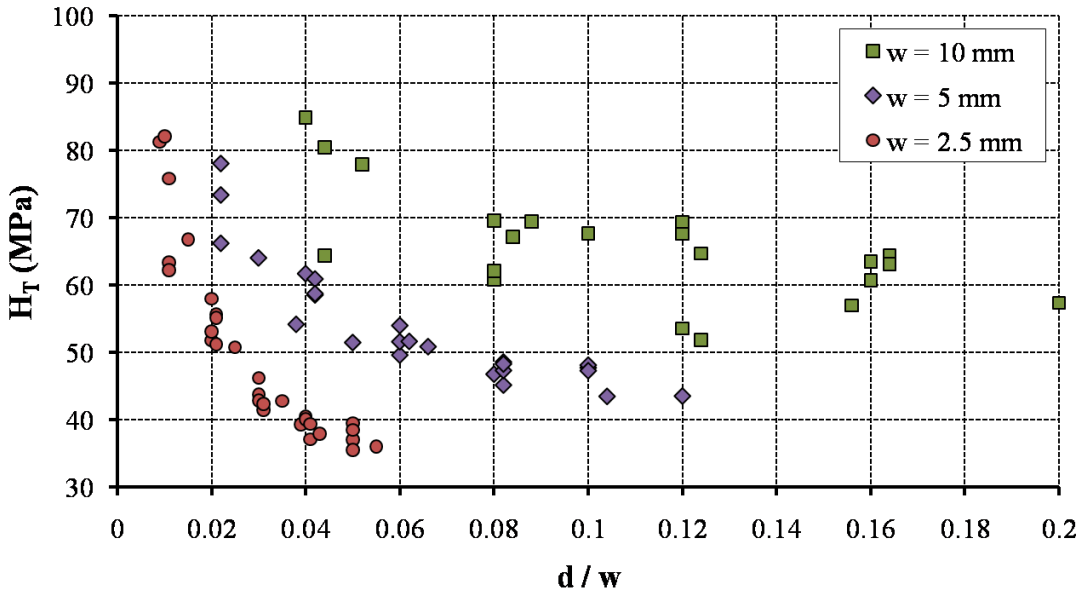

Figure 7-1: Tangential hardness H_T vs. depth–to–width ratio d/w [Test on cement paste; tests carried out by Epslog Engineering (Belgium); data courtesy of Schlumberger].

Figure 7-1 displays the tangential hardness $H_T = F_T/(wd)$ as a function of the ratio d/w for the tests on cement paste. If relationship (7.1) was satisfied, all the points would collapse on a single curve, irrespectively of the width w of the cutter. This is obviously not the case since one can identify three curves, corresponding to the three different blade widths. Another series of tests with different depths of scratch and blade width has been carried out on Vosges Sandstone by a research team of University of Minnesota [50] [51] [21]. The results are displayed in figure 7-2. While the trend is somewhat different from the one observed on cement paste, a dependence on the width is observed: the two smaller widths tested ($w = 2.56$mm and $w = 5$mm) show a different behavior than the two larger with an increase of the hardness H_T when the depth of scratch is increased. Once again, a pure strength model cannot account for this geometric effect.

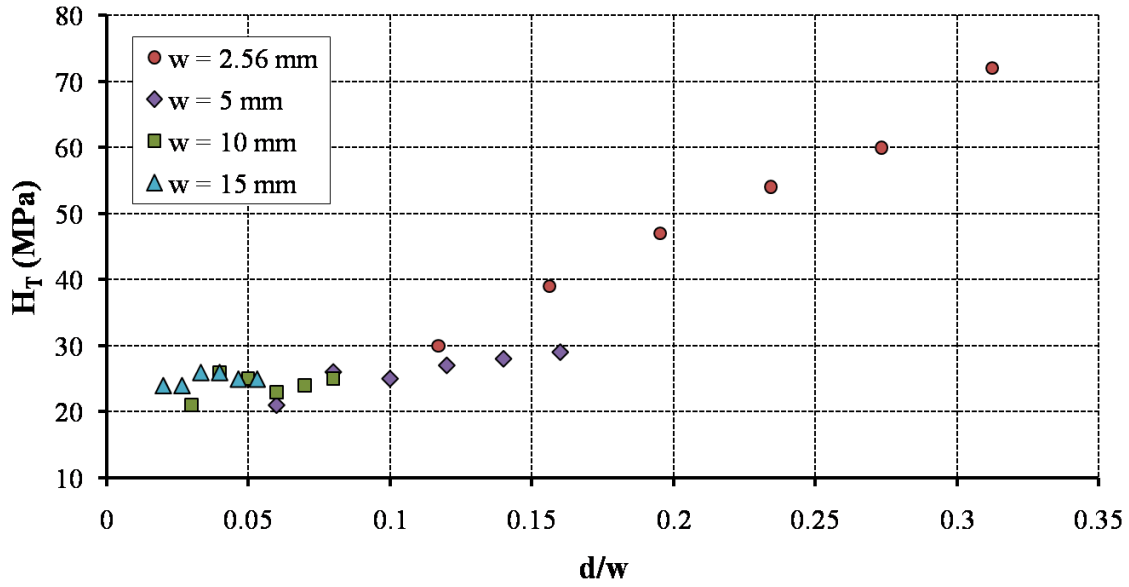

Figure 7-2: Tangential hardness H_T vs. depth–to–width ratio d/w [Test on Vosges Sandstones [51]].

7.2 From Strength to Fracture

Scale effects are typically associated with fracture processes in which free energy stored in the bulk of the material is dissipated during the crack propagation through the creation of free surfaces. Pictures of the tests performed on Vosges sandstones are displayed in figure 7-3. It depicts two different modes of failure:

- The so-called ductile mode (a), which takes place at small depths of scratch (typically $d \leqslant 1$mm) on the sandstone. It is characterized by a pile-up of failed material being pushed by the blade.

- The fracture mode (b), taking place at depths $d > 1$mm, in which chips of material are removed in front of the cutter with the propagation of a macroscopic crack.

All the data presented in the previous paragraph were measured in the ductile mode. However the appearance of macroscopic cracks for values of d of the same order might indicate the formation of microcracks even in the ductile mode, which could explain the actual scaling not expected in a pure strength configuration. The idea is not new:

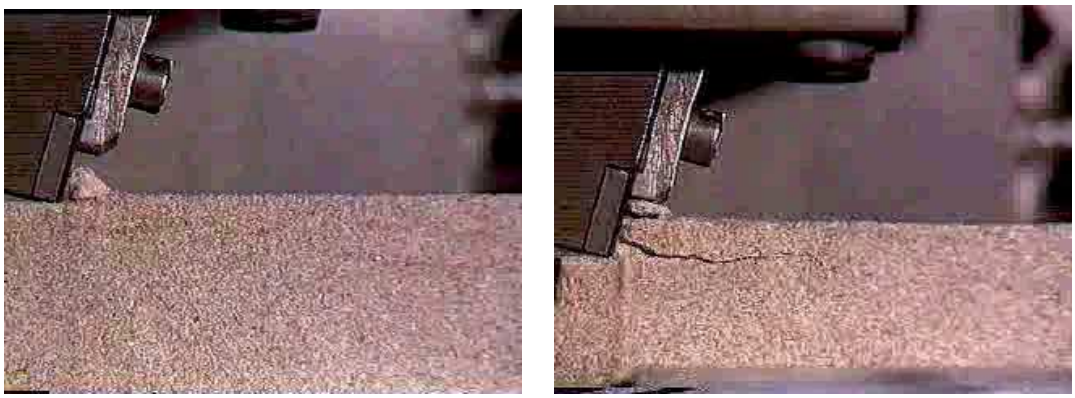

(a) (b)

Figure 7-3: Scratch tests on Vosges Sandstone with a rectangular indenter: (a) ductile mode; (b) fracture mode.

in 2004, Atkins proposed a way of determining fracture toughness of ductile materials through a cutting process [3].

7.3 Fracture Approach

A new dimensional analysis in which linear elastic fracture mechanisms [68] are predominant over plasticity is now performed. In equation (2.7), we now consider the case $\mathcal{I} = \frac{d}{(K_{Ic}/\sigma_0)^2} \to \infty$, removing the influence of the strength parameters σ_0, α, n. This yields a new dimensionless relation for the hardness:

$$H_T = \frac{K_{Ic}}{\sqrt{w}} \tilde{\Pi}^f \left(\frac{d}{w}, \theta, \frac{E\sqrt{w}}{K_{Ic}}, \nu, \mu_i \right) \tag{7.2}$$

where K_{Ic} (expressed in MPa$\cdot\sqrt{\text{m}}$) is the fracture toughness and can be linked to the fracture energy of the material $G_f = \frac{K_{Ic}^2}{E'}$ where $E' \propto E$ depends on the configuration of the problem (e.g. $E' = E/(1-\nu^2)$ in plane strain)[1].

Considering relation 7.2 the actual quantity of interest is no longer the scratch hard-

[1] G_f is used in the classic crack propagation law based on Griffith's work [29]:

$$(G - G_f) \leqslant 0 \; ; \; \dot{\Gamma} \geqslant 0 \; ; \; (G - G_f)\dot{\Gamma} = 0$$

where Γ is the crack surface, $\dot{\Gamma}$ the crack surface growth rate, and $G = -\frac{\partial E_{pot}}{\partial \Gamma}$ the energy release rate.

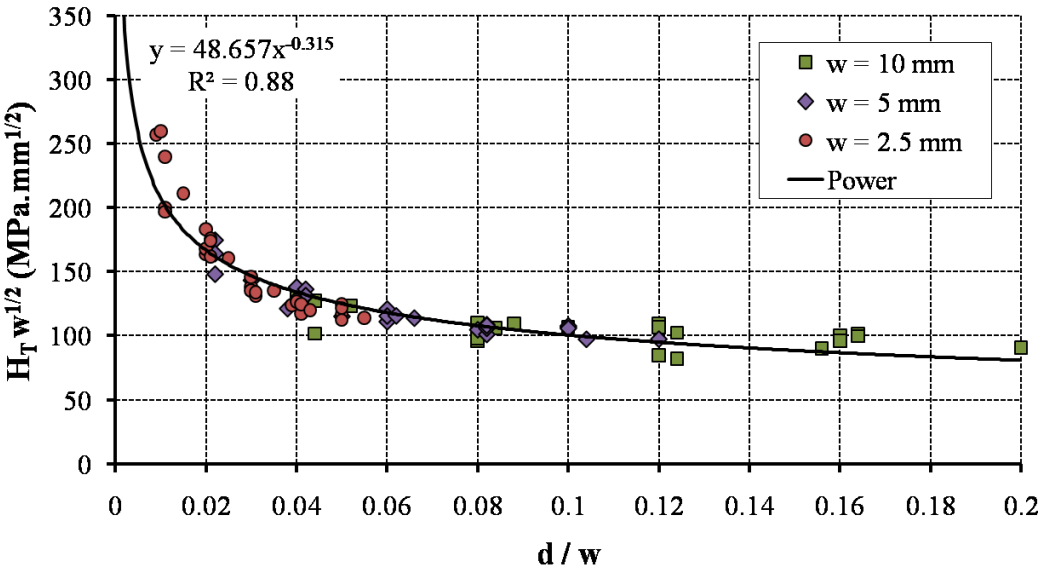

Figure 7-4: $H_T\sqrt{w}$ vs. depth–to–width ratio d/w [Test on cement paste; tests carried out by Epslog Engineering (Belgium); data courtesy of Schlumberger].

ness H_T itself but $H_T\sqrt{w}$ (or $H_T\sqrt{d}$), which should be proportional to the fracture toughness K_{Ic} of the material. Figure 7-4 backs up the fracture interpretation since the data from the three different widths collapse on a single curve. Fitting a power function, an experimental relation for the hardness can be found:

$$H_T \propto K_{Ic} w^{-0.185} d^{-0.315} \tag{7.3}$$

Figure 7-5 does not show the same collapse of the data from different widths on a single curve. However, despite some scattering, the power function (7.3) seems to fit the overall trend for $w = 5, 10, 15$ mm. The $w = 2.56$ mm case exhibits a behavior that neither the strength model, nor the fracture model can explain.

7.4 Finite Element Simulations

Relation (7.3) relies on dimensional analysis and results from experimental data. In this paragraph we investigate the scaling relations between hardness, energy release rate, and geometry by means of finite element simulations.

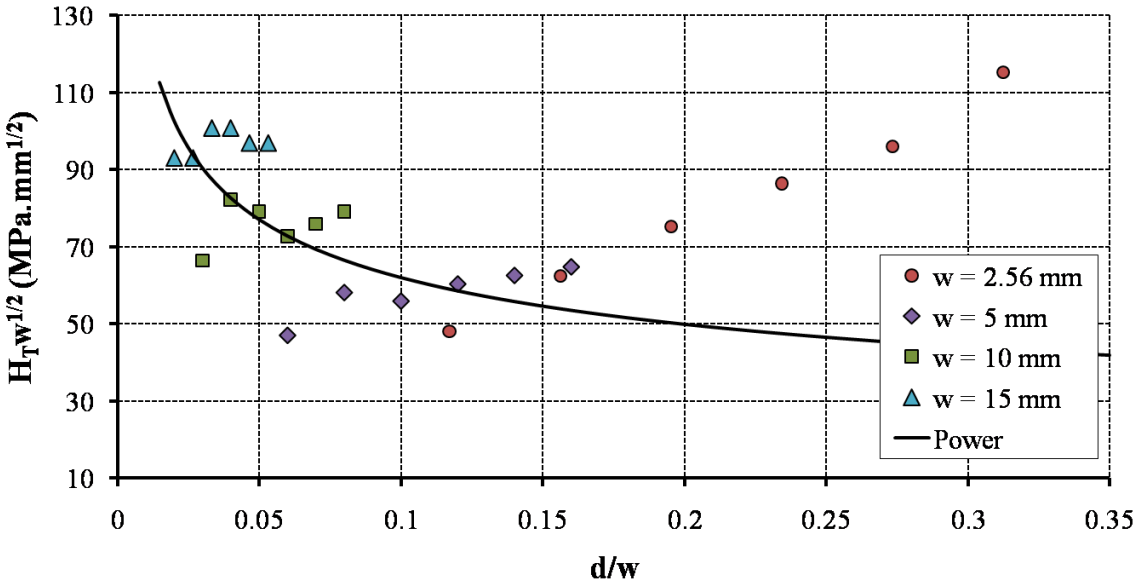

Figure 7-5: $H_T\sqrt{w}$ vs. depth–to–width ratio d/w [Test on Vosges Sandstones [51]].

7.4.1 Principle

Our approach is based on the energy and compliance method developed initially by Watwood [65]. In the LEFM framework the only source of dissipation is the crack growth. Based on this premise, the energy and compliance method consists in comparing the energy stored in the material before and after crack propagation. Let us call a the crack length. The compliance of the system is:

$$C(a) = \frac{u}{F_T}(a) \tag{7.4}$$

where u is the horizontal displacement of the point of application of F_T. The potential energy for an imposed displacement u is:

$$E_{pot} = \frac{1}{2}\frac{u^2}{C} \tag{7.5}$$

Inserting this relation in the definition of the energy release rate yields:

$$G \overset{def}{=} -\frac{\partial E_{pot}}{\partial \Gamma} = \frac{1}{2}\frac{\partial C}{\partial \Gamma}F_T^2 \tag{7.6}$$

where $\Gamma = (2d/w + 1)wa$ is the crack area.

Finally we consider that in actual scratch tests the crack propagation is equal to the displacement of the blade, which is true on-average and seems a reasonable assumption when the development of microcracks causes the failure of the material. As a consequence, in reaction to the displacement of the blade, the material will release energy at the rate defined by the law of crack propagation:

$$G = G_f \text{ for } \dot{\Gamma} > 0 \tag{7.7}$$

Combining (7.6) and (7.7) yields the expected tangential force:

$$F_T = \sqrt{2G_f} \left(\frac{\partial C}{\partial \Gamma} \right)^{-1/2} \tag{7.8}$$

We actually do not need to know G_f. Indeed, we are only interested in the scaling relations of the force F_T with the geometric parameters w and d. We hence normalize all the values by a reference configuration: d_0, w_0, and $F_{T0} = \sqrt{2G_f} \left(\frac{\partial C}{\partial \Gamma} \right)^{-1/2} \Big|_{w=w_0, d=d_0}$. The change in compliance $\frac{\partial C}{\partial \Gamma}$ is found by using two finite element calculations: one with a crack length a (crack surface $\Gamma = (2d/w + 1)wa$), the other with a crack length $a + \Delta a$ ($\Gamma + \Delta\Gamma = (2d/w + 1)w(a + \Delta a)$). We use the classic discretization approximation:

$$\frac{\partial C}{\partial \Gamma} \approx \frac{C(a + \Delta a) - C(a)}{(2d/w + 1)w\Delta a} \tag{7.9}$$

7.4.2 Presentation of the Simulations

We use a 3D Abaqus model for our simulations. Tests are performed on nine different geometries: three values of width and three values of depth (see Table 7.1), spanning a depth–to–width ratio d/w from 10^{-2} to 1. A unique back-rake angle is considered, $\theta = 15°$. To obtain comparable results, the meshing of the part must be similar in all the different geometries. However, while fine mesh is required in the smallest case ($w = 1$mm, $d = 0.1$mm), CPU time becomes a limit for larger geometries. We hence chose to mesh the material in three distinct zones: the 'chip' part is in contact with

the blade and constitutes the most critical zone in terms of stresses. It is meshed with 8-node linear hexahedra of size 0.02 mm (blue on figure 7-6b). It is tied to the 'core' part, which makes the transition to the surrounding material with a 4-node tetrahedron linear element mesh whose sizes varies from 0.02 mm on the surface of contact with the 'core' part (node-to-node tie) to 0.2 mm on the surface of contact with the surrounding material, which is itself meshed with 8-node linear hexahedra of size 0.5 mm. This mesh allows us to apply the no-displacement boundary conditions far from the scratch zone, have reasonable accuracy and limited mesh size dependence in the scratch zone, with a tractable number of elements in all cases (from 36,283 to 102,245). We use a purely elastic material with Young's modulus $E = 20$ GPa and Poisson's ratio $\nu = 0.4$. A displacement of 0.01 mm is imposed to the blade, which is in frictionless contact with the material. The tangential force is recorded and the compliance is extracted using formula (7.4). Finally, a crack is open by removing the tie constraint between nodes of the 'chip' part and nodes of the 'core' part. For each geometry, three simulations are performed corresponding to $a = 0$ (no crack), $a = 0.1$ mm, and $a = 0.2$ mm.

width (mm)	depth (mm)	crack length (mm)
1,3,10	0.1,0.5,1	0, 0.1, 0.2

Table 7.1: Summary of the different FE calculations.

7.4.3 Results

We choose ($d_0 = 1$ mm, $w_0 = 10$ mm) as a the reference configuration. The 27 simulations yields expected values of F_T for two crack growths: from 0 to 0.1 mm, and from 0.1 to 0.2 mm. Slight differences are observed for the calculation of the tangential force F_T for these two different crack growths. A complementary analysis of the influence of the mesh size and crack growth increment leads us to consider only the crack growth from 0.1 to 0.2 mm for quantitative comparisons between geometries. Indeed, the calculation of the derivative of the compliance is affected by the size of the growth increments when starting from no crack, while it remains constant for the

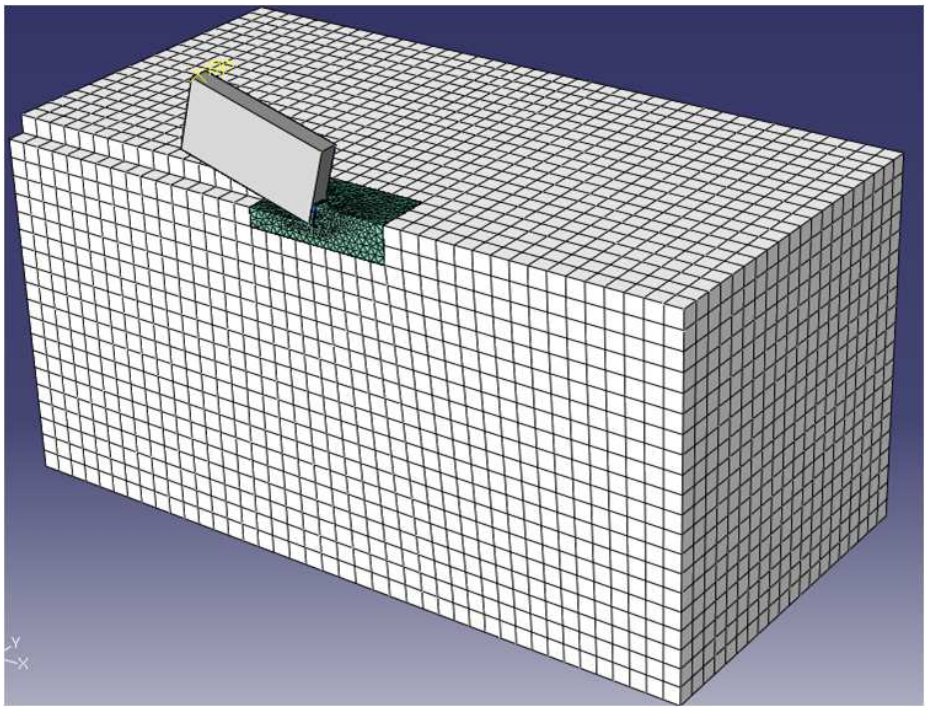

(a)

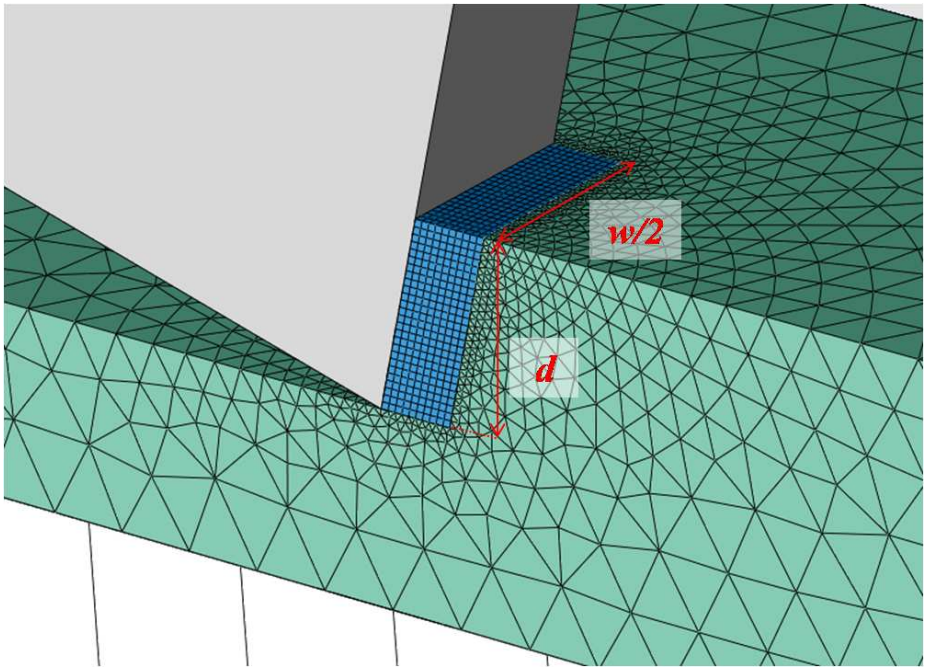

(b)

Figure 7-6: Finite element geometry and mesh: (a) overall view; (b) close-up on the crack zone [model presented: $w = 1$mm, $d = 0.5$mm, mesh size in the crack zone: 0.02mm].

growth of pre-existing cracks (Figure 7-7). Using the method of least square on the 9 computed values of F_T/F_{T0} to fit this ratio as a power function of w/w_0 and d/d_0 yields:

$$\frac{F_T}{F_{T0}} = 1.018 \left(\frac{w}{w_0}\right)^{0.8603} \left(\frac{d}{d_0}\right)^{0.4701} \tag{7.10}$$

Figure 7-8 shows that this fitted function fits well the finite element data. In terms of tangential hardness, (7.10) reads:

$$\frac{H_T}{H_{T0}} = 1.018 \left(\frac{w}{w_0}\right)^{-0.1397} \left(\frac{d}{d_0}\right)^{-0.5297} \tag{7.11}$$

This expression is in relatively good correlation with the experimental data of scratch tests on cement paste (7.3). However, the FE results depart from the shape expected when using dimensional analysis (7.2): for given elastic constants and back-rake angle, the product $H_T\sqrt{w}$ cannot be written as a function depending only on the ratio d/w.

7.4.4 Discussion: Validity of the Approach

The validation of the fracture model (7.2) by the finite element simulations can be disputed. To improve the accuracy of the method and obtain reliable scaling relations, a comprehensive study of the effect of the simulation parameters was performed. For example, Figure 7-7 shows that the calculation of $\frac{\partial C}{\partial \Gamma}$ on which the method is based is dependent of the choice of the crack growth increment for $a = 0$. To compare geometries to each other requires to find a normalized crack growth increment. However, no such scaling backed up by analytical reason could be found. We reach here the main problem of the simulations: meshing and crack modeling add length scales to the problem (Table 7.2). While this is not always a problem (the compliance method was successfully implemented in several finite element analyses, see e.g. [45]), it here interferes with the goal of finding scaling relations to understand the role of the different length scales of the problem, which makes the use of the compliance method disputable for this particular problem.

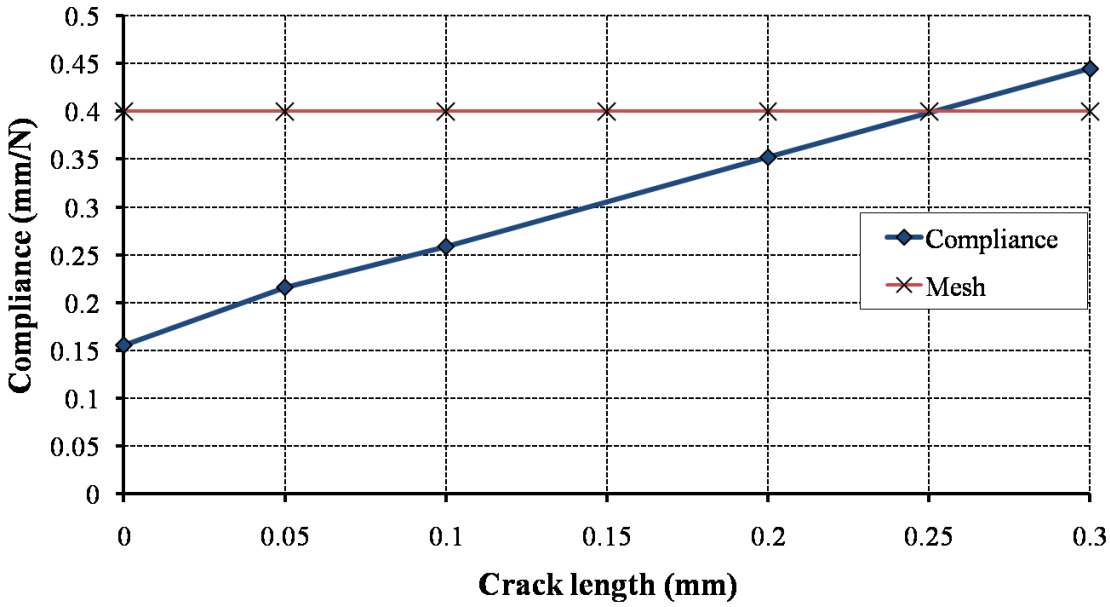

(a) Mesh size: 0.05 mm

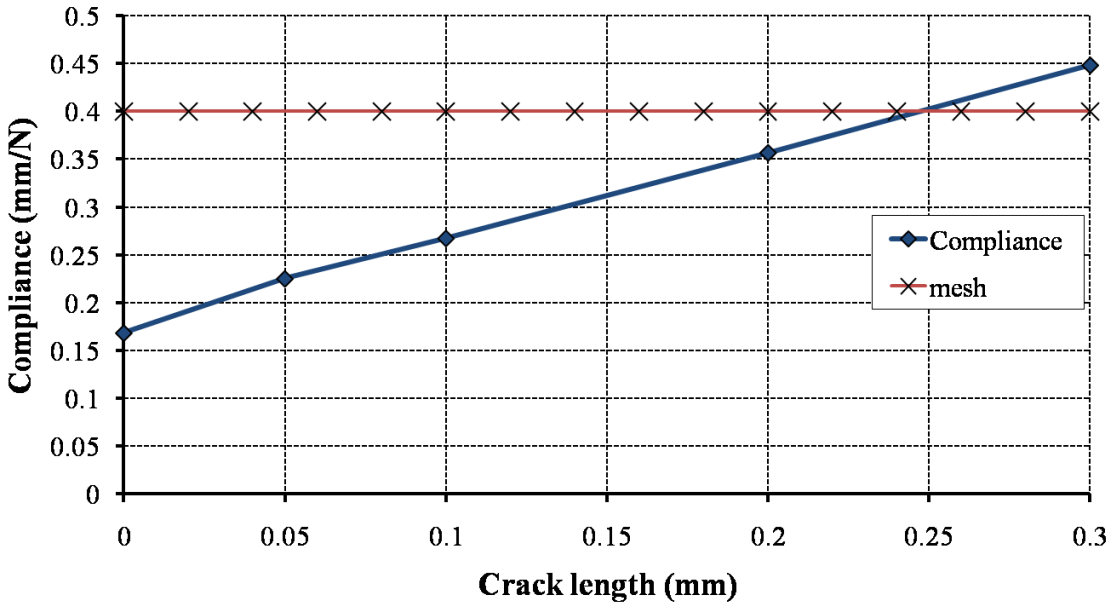

(b) Mesh size: 0.02 mm

Figure 7-7: Computed compliance vs. crack length for $w = 1$ mm and $d = 0.1$ mm and two mesh sizes.

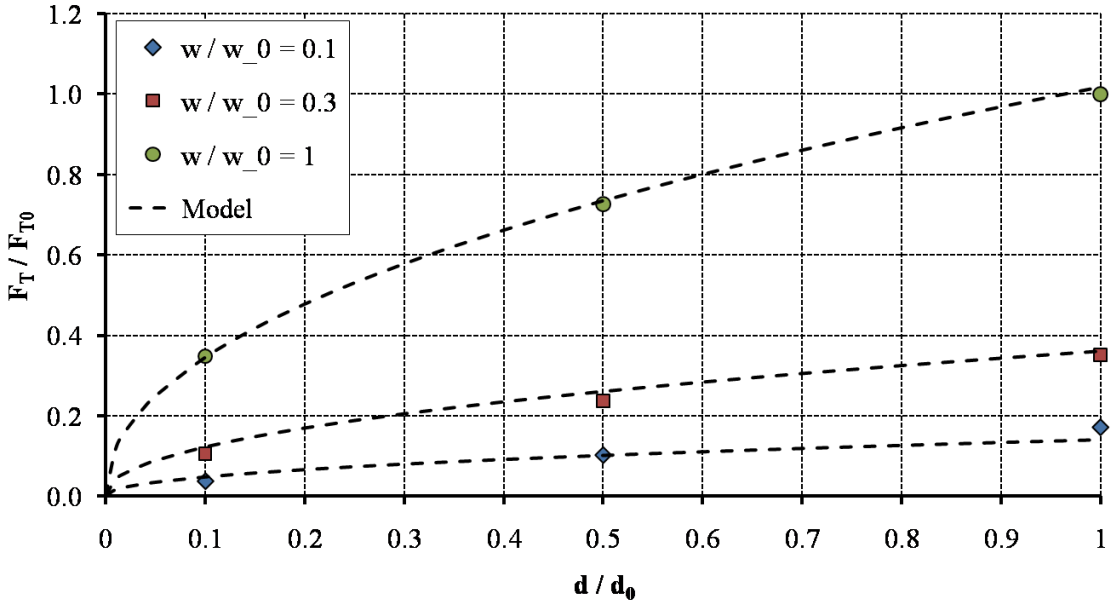

(a) F_T/F_{T0} vs. normalized depth d/d_0 for crack propagation $0.1 \rightarrow 0.2$ mm.

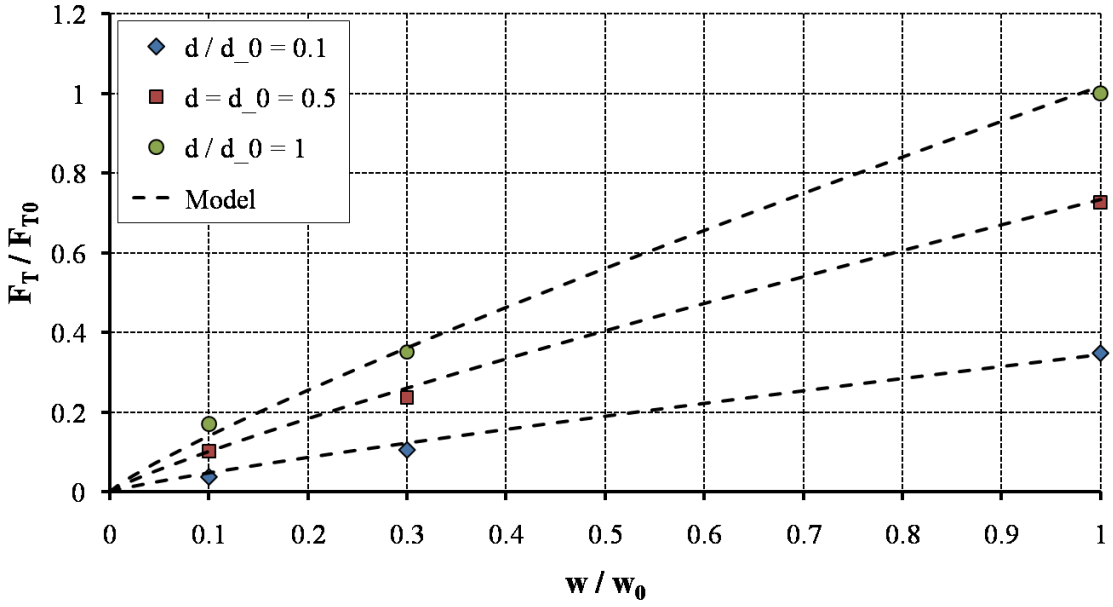

(b) F_T/F_{T0} vs. normalized width w/w_0 for crack propagation $0.1 \rightarrow 0.2$ mm.

Figure 7-8: Comparison of the FE simulations discrete values and the fitted power function (7.11).

Actual problem	Numerical simulations
width w	width w
depth d	depth d
	mesh size
	crack growth increments Δa

Table 7.2: Artificial length scales inherent to the numerical simulations

7.5 Chapter Summary

In this chapter we showed that geometric scaling relations of experimental data are in contradiction with the assumption that the scratch test is a pure strength problem. A first investigation of the scratch test as a fracture problem partly accounts for the scaling for the tests on cement paste. However, the correlation with sandstones data is not as good. The finite element simulations based on the compliance method yields scaling relations close to the ones found on experimental data on cement paste. However, the method does not seem adapted to the problem due to the creation of artificial length scales. A better understanding of the fracture phenomena will surely involve a robust analytical model.

Chapter 8

Conclusion and Perspectives

The scratch hardness – strength relations given by our model based on yield design theory constitute a step toward a better use of the scratch test in testing cohesive-frictional materials. A similar approach to indentation initiated a decade ago led to the use of nanoindentation as a means to probe complex granular and porous materials. Further developments could allow the scratch test technique to become a complementary tool to measure microproperties of such materials. We here summarize the main contributions and limitations of our work for a better understanding of the scratch test.

8.1 Summary of Main Findings

1. In the application of the lower-bound approach, a simple stress field shape was proposed in response to the problem of the scratch test with rectangular indenter. Its simplicity allowed us to find explicit relations between the scratch hardness and the strength properties of cohesive and cohesive-frictional materials represented by the Tresca, Von Mises, Mohr-Coulomb, and Drucker-Prager criteria.

2. The hardness–to–strength relations given by the model show that there is no direct correlation between the uniaxial compressive strength and the hardness.

The formulas obtained on purely cohesive materials (Tresca and Von Mises) show that a more relevant strength quantity measured in a scratch test is the cohesion (or shear strength).

3. This highly adaptable model allowed us to consider friction at the blade–material interface, and to implement a strength criterion representing porous materials. The results are given in this case by a quick and stable non linear optimization.

4. The lower-bound results are validated against upper-bound and finite element models. The good predictive power of such a rough model is explained by its comparison with the stress field solution of the finite element calculation: the scratch hardness is determined by the stress field in the zone situated just bellow the blade, which is precisely the location where the constant stress field approximation is the closest to the solution.

5. The use of dimensional analysis and the comparison of the prediction of the strength model with experimental results on cement paste and sandstone hints toward the influence of fracture phenomena in scratch tests on rocks or cementitious materials.

8.2 Current Limitations and Future Perspectives

1. The lower-bound model is applicable with good accuracy only to the rectangular indenter case. The presence of tilted free surfaces in the groove for other classical shapes of indenters (spherical, pyramidal, conical) limits the use of piecewise constant stress fields to capture the complex stress fields.

2. The assumption that the scratch test is a pure strength problem limits its application. Although the elastoplastic FE simulations seem to confirm the very small influence of elasticity on the scratch hardness, this consideration may become critical in nanoscale scratch tests for the measurement of the width

and/or depth of indentation in case of non negligible elastic recovery. In cases where fracture is the main phenomenon at work during a scratch test, the strength model is no more relevant. The conditions in which a scratch test can be modeled as a strength or a fracture process are not yet known. The determination of these conditions will require the development of a fracture model, as initiated in the last chapter of the thesis.

3. The model is validated by other approaches but lacks comprehensive comparisons with experimental data. This calls for a future series of experiments with well-known materials (e.g. cement paste) and controlled experimental conditions.

8.3 Conclusion

The model presented in this work was developed in order to give analytical grounds for the empirical correlation between scratch hardness and UCS of rocks found by Detournay et al. [37]. This model, which yields a lower bound for the hardness, predicts a minimum hardness–to–UCS ratio of 1.26 (obtained for the Tresca criterion with $\theta = 15^\circ$), whereas Detournay et al. have found a ratio of the order of 1. This discrepancy shows that macroscopic scratch tests on rocks cannot be explained by strength alone. Instead they most likely involve fracture processes.

The strength model can however prove useful in application to nanoscratch experiments, in which plastic phenomena are most likely to prevail over fracture phenomena.

Appendix A

Optimization Code

In this appendix, we show the commented Matlab code used for the optimization procedure of the lower bound approach. The upper bound approach optimization procedure uses the same architecture.

A.1 User Environment

The hardness is obtained from a single function called `wedge_uni`, whose input parameters are the interface friction coefficient μ_i, the back-rake angle θ, the strength criterion, the initial value used for the optimization, the normalization (cohesion or UCS), and the saturation of the friction law (forced or free):

```
%Input: friction coefficient, back-rake angle (in degrees), criterion, criterion
%parameters (if applicable), initial values, normalization (1 = cohesion, 2
%= UCS), saturation of the friction law (0 = no, 1 = yes)
% Criterion parameters:
%------ TR & VM -> not applicable, leave blank or put any value
%------ DP -> cr1 == alpha (no dimension), cr2 & cr3 not applicable
%------ MC -> cr1 == phi (in degrees), cr2 & cr3 not applicable
%------ MT & SC -> cr1 == alpha (no dimension), cr2 == eta (packing density in
%[0,1])
```

```
%
% Output: H_T, stress components, ratio F_V / F_T, angle beta
function [Ht,sigma,ratio,beta]=wedge_uni(m,th,criterion,cr1,cr2,ini,norm,sat)

% Set the default values of optional innput parameters
if nargin < 8
    sat = 0
end
global saturation
saturation = sat;

if nargin < 7
    norm = 1;
end

global init
if nargin < 6 || length(ini)~=5
    init = [0;-0.8622;0.4978;-.9;-.1];
else
    init = ini;
end

if nargin < 5
    cr2 = 0;
end

if nargin < 4
    cr1 = 0;
end
```

```
% Define the global variables
global sigma
global Jval
global mu
mu = m;
global theta
theta = th;
global crit
crit = criterion;
global alpha
alpha = cr1;
global phi
phi = cr1;
global eta
eta = cr2;

% Call the Optimization code
Optim;

%Process the data
Ht = -Jval;
ratio = (sigma(3) - tand(theta) * sigma(2))/ (tand(theta) * sigma(3) - sigma(1));
if norm == 1
    disp(['Ht / c = ', num2str(Ht)]);
elseif norm == 2
    if crit == 'TR'
        Ht = Ht / 2;
        sigma = sigma / 2;
    elseif crit == 'VM'
        Ht = Ht / sqrt(3);
```

```
        sigma = sigma / sqrt(3);
    elseif crit == 'MC'
        Ht = Ht * (1-sind(phi)) / (2*cosd(phi));
        sigma = sigma * (1-sind(phi)) / (2*cosd(phi));
    elseif crit == 'DP'
        Ht = Ht * (sqrt(3)-alpha) / 3;
        sigma = sigma * (sqrt(3)-alpha) / 3;
    elseif crit == 'MT' | crit == 'SC'
        u = ucs_H1(A2,B2,SIG0);
        Ht = Ht / u;
        sigma = sigma / u;
    end
    disp(['Ht / UCS = ', num2str(Ht)]);
end

%Value of the angle beta
beta = atand(-sigma(3)/sigma(2));
end
```

A.2 Optimization Code

The user function calls for the code `optim`, which is the core of the optimization procedure:

```
%sigma is the vector of stresses: [s_x;s_z;tau;s_y;s_y2]
global sigma
%theta is the angle of the wedge
global theta
t = tand(theta);
%mu is the friction coefficient at the interface indenter-material
```

```
global mu
%init is the initial value for the vector of stresses
global init

%saturation of the friction law
global saturation

%----------- STRENGTH PROPERTIES ----------------------------------------

%Strength properties: cohesion c = 1
global crit % crit is the criterion: 'TR','MC','VM','DP','MT','SC'
global alpha % alpha is the drucker-prager coefficient
global phi % phi is the friction angle for MC criterion
global eta % eta is the packing density for homogeneized criterion

% Homogeneized criterion: additional properties
global eta_cr % eta_cr is the critical packing density
%A2, B2 and SIG0 are the parameters entering the homogenized strength function
global A2
global B2
global SIG0
if crit == 'MT'
    [K,M] = Mori_Tanaka(alpha,eta); %This function returns K^{MT},M^{MT}
    eta_cr = eta_crit(alpha); %This function returns eta_cr
    [A2,B2,SIG0] = Hom(alpha,eta,K,M); %This function returns A2,B2 and SIG0
elseif crit == 'SC'
    [K,M] = Self_consistent(alpha,eta);%This function returns K^{SC},M^{SC}
    [aaa,eta_cr] = eta_crit(alpha);%This function returns eta_cr
    [A2,B2,SIG0] = Hom(alpha,eta,K,M);%This function returns A2,B2 and SIG0
end
```

```
%-------------------------------------------------------------------------

%----------------- OPTIMIZATION ------------------------------------------
% Set the lower and upper bounds for the stress components
lb = [-100;-100;-100;-100;-100];
ub = [100;100;100;100;100];

% Set the linear constraints:
% - A*sigma - b < 0
% - Aeq*Sigma - beq = 0
global A
global b
global Aeq
global beq
if mu == 0
    %1st row: geometric constraint on beta: beta > -theta
    %2nd row: sigma_n < 0 (contact)
    A = [0 t -1 0 0;1 t^2 -2*t 0 0];
    b = [0;0];
    %sigma_t = 0
    Aeq = [t -t (1-t^2) 0 0];
    beq = [0];
elseif mu ~= 0 & saturation == 0
    %1st row: geometric constraint on beta: beta > -theta
    %2nd row: sigma_n < 0 (contact)
    %3rd row: mu*sigma_n < sigma_t
    %4th row: sigma_t < -mu*sigma_n
    A = [0 t -1 0 0;1 t^2 -2*t 0 0;(mu-t),(mu*t+1)*t,(t^2-1-2*mu*t),0,0;(mu+t),(mu
    b = [0;0;0;0];
    Aeq = [];
```

```
    beq = [];
elseif mu ~= 0 & saturation == 1
    %1st row: geometric constraint on beta: beta > -theta
    %2nd row: sigma_n < 0 (contact)
    A = [0 t -1 0 0;1 t^2 -2*t 0 0];
    b = [0;0];
    Aeq = [];
    beq = [];
end

% Options of the minimization function
options = optimset('LargeScale','off','Display','off',...
    'TolFun', 1.0e-7,'TolX', 1.0e-7);

%Minimization function:
% - J is the function being minimized, namely -H_T.
% - nonlcon is the function listing the non-linear constraints
[sigma, Jval] = fmincon(@J,init,A,b,Aeq,beq,lb,ub,@nonlcon,options);
```

A.3 Minimized Function and non-Linear Constraints

The optimization procedure displayed in the previous paragraph calls the fundamental functions `J` and `nonlcon`. `J` is the function which is minimized, which is $-H_T(\underline{\underline{\sigma}})$. `nonlcon` represents the non-linear conditions imposed to the stress tensor $\underline{\underline{\sigma}}$:

```
function f = J(s)
global theta
% -H = s_xx - tan(theta) * s_xy
f = s(1) - tand(theta)*s(3);
end
```

```
%-------------------------------
function [c,ceq] = nonlcon(s)
global saturation
global mu
global theta
c=[C1(s);C2(s)];
if saturation == 0
    ceq=[];
elseif saturation == 1
    ceq = mu*(cosd(theta)^2*s(1) + sind(theta)^2*s(2) - sind(2*theta)*s(3))...
        + abs(cosd(theta)*sind(theta)*(s(2)-s(1))+s(3)*(1-2*cosd(theta)^2));
end
%-------------------------------
% Strength in domain 1 (under the indenter)
% input: s = [s_xx;s_zz;s_xz;s_yy;s_yy2];
function c = C1(s)
global crit
sig = [s(1),0,s(3);0,s(4),0;s(3),0,s(2)];
pr = eig(sig);
if crit == 'TR'
    c = pr(3) - pr(1) - 2;
elseif crit == 'MC'
    global phi
    c = pr(3)*(1 + sind(phi)) - pr(1)*(1-sind(phi)) - 2*cosd(phi);
elseif crit == 'VM'
    dev = sig - trace(sig)/3*eye(3);
    J2 = 0.5 * trace(dev*dev);
    c = J2 - 1;
elseif crit == 'DP'
    global alpha
```

```
    dev = sig - trace(sig)/3*eye(3);
    J2 = 0.5 * trace(dev*dev);
    c = sqrt(J2) + alpha*trace(sig)/3 - 1;
elseif crit == 'MT' | 'SC'
    global alpha
    global A2
    global B2
    global SIG0
    global eta
    global eta_cr

    sm = trace(sig) / 3;
    dev = sig - sm*eye(3);
    J2 = 0.5 * trace(dev*dev);

    if eta < eta_cr
        c = (sm - SIG0)^2 / A2 + J2 / B2 - 1;
    else
        c = -(sm - SIG0)^2 / A2 - J2 / B2 + 1;
    end
end
end
%------------------------------
% Strength in domain 2 (under the free surface)
% input: s = [s_xx;s_zz;s_xz;s_yy;s_yy2];
function c = C2(s)
beta = atan(-s(3)/s(2));
global crit
sig = [s(1) - s(3)^2/s(2),0,0;0,s(5),0;0,0,0];
pr = eig(sig);
```

```
if crit == 'TR'
    c = pr(3) - pr(1) - 2;
elseif crit == 'MC'
    global phi
    c = pr(3)*(1 + sind(phi)) - pr(1)*(1-sind(phi)) - 2*cosd(phi);
elseif crit == 'VM'
    dev = sig - trace(sig)/3*eye(3);
    J2 = 0.5 * trace(dev*dev);
    c = J2 - 1;
elseif crit == 'DP'
    global alpha
    dev = sig - trace(sig)/3*eye(3);
    J2 = 0.5 * trace(dev*dev);
    c = sqrt(J2) + alpha*trace(sig)/3 - 1;
elseif crit == 'MT' | 'SC'
    global alpha
    global A2
    global B2
    global SIG0
    global eta
    global eta_cr

    sm = trace(sig) / 3;
    dev = sig - sm*eye(3);
    J2 = 0.5 * trace(dev*dev);

    if eta < eta_cr
        c = (sm - SIG0)^2 / A2 + J2 / B2 - 1;
    else
        c = -(sm - SIG0)^2 / A2 - J2 / B2 + 1;
```

```
    end
end
end
```

Bibliography

[1] Minasse Abebe and F. C. Appl. Theoretical analysis of the basic mechanics of abrasive processes: Part i: General model. *Wear*, 126(3):251–266, 9/15 1988.

[2] Minasse Abebe and F. C. Appl. Theoretical analysis of the basic mechanics of abrasive processes: Part ii: Model of the ploughing process. *Wear*, 126(3):267–283, 9/15 1988.

[3] A. G. Atkins. Toughness and cutting: a new way of simultaneously determining ductile fracture toughness and strength. *Engineering Fracture Mechanics*, 72(6):849–860, 4 2005.

[4] A. Azarkhin and O. Richmond. A model of ploughing by a pyramidal indenter upper bound method for stress-free surfaces. *Wear*, 157(2):409–418, 9/15 1992.

[5] G. I. Barenblatt. *Scaling, self-similarity, and intermediate asymptotics*. Cambridge University Press, New York, 1996. Uniform Title: Podobie, avtomodelnost, promezhutochnaia asimptotika. English; Grigory Isaakovich Barenblatt.

[6] Klaus-Jürgen Bathe. *Finite element procedures*. Prentice Hall, Englewood Cliffs, N.J., 1996. Klaus-Jürgen Bathe.; Revision of: Finite element procedures in engineering analysis. 1982.

[7] S. Bellemare, M. Dao, and S. Suresh. The frictional sliding response of elastoplastic materials in contact with a conical indenter. *International Journal of Solids and Structures*, 44(6):1970–1989, 3/15 2007.

[8] Lavinia Borges and Nestor Zouain. A nonlinear optimization procedure for limit analysis. *European Journal of Mechanics, A/Solids*, 15(3):487–512, 1996.

[9] Lavinia Borges, Nestor Zouain, Cyntia Costa, and Raul Feijo. An adaptive approach to limit analysis. *International Journal of Solids and Structures*, 38(10-13):1707–1720, 3 2001.

[10] Frank Philip Bowden and David Tabor. *The friction and lubrication of solids*. Clarendon Pr., Oxford, 1964. by F.P. Bowden and D. Tabor.; 2 v. illus.; Part I was first published in 1950 and is reprinted from corrected sheets of the first impression in 1964. Part II is published in 1964. The text of Part I is basically the same as that of the 1958 reprint.; Bibliography: Includes bibliographies.

[11] B. J. Briscoe, S. K. Biswas, S. K. Sinha, and S. S. Panesar. The scratch hardness and friction of a soft rigid-plastic solid. *Tribology International*, 26(3):183–193, 6 1993.

[12] B. J. Briscoe, E. Pelillo, S. K. Sinha, and P. D. Evans. Scratching maps for polymers. *Wear*, 200(1-2):137–147, 12/1 1996.

[13] E. Buckingham. On physically similar systems; illustrations of the use of dimensional equations. *Physical Review*, 4:345–376, 1914.

[14] S. J. Bull and E. G. Berasetegui. An overview of the potential of quantitative coating adhesion measurement by scratch testing. *Tribology International*, 39(2):99–114, 2 2006.

[15] J. Byerlee. Friction of rocks. *Pure and Applied Geophysics*, 116(4-5):615–626, 1978.

[16] Sophie Cariou, Franz-Josef Ulm, and Luc Dormieux. Hardnesspacking density scaling relations for cohesive-frictional porous materials. *Journal of the Mechanics and Physics of Solids*, 56(3):924–952, 3 2008.

[17] P. Ponte Castaeda. The effective mechanical properties of nonlinear isotropic composites. *Journal of the Mechanics and Physics of Solids*, 39(1):45–71, 1991.

[18] J. M. Challen and P. L. B. Oxley. An explanation of the different regimes of friction and wear using asperity deformation models. *Wear*, 53(2):229–243, 4 1979.

[19] J. M. Challen and P. L. B. Oxley. An explanation of the different regimes of friction and wear using asperity deformation models. *Wear*, 53:229–243, 1979.

[20] Yang-Tse Cheng and Che-Min Cheng. Scaling, dimensional analysis, and indentation measurements. *Materials Science and Engineering: R: Reports*, 44(4-5):91–149, 8/1 2004.

[21] F. D. Dagrain. Influence of the cutter geometry in rock cutting with pdc cutters: an experimental approach, 2001.

[22] J. Desrues. Limitations du choix de l'angle de frottement pour le critère de plasticité de drucker-prager. *Revue Française de Génie Civil*, 6:853–862, 2002.

[23] E. Detournay and P. Defourny. Phenomenological model for the drilling action of drag bits. *International Journal of Rock Mechanics and Mining Sciences and Geomechanics Abstracts*, 29(4):13–23, 7 1992.

[24] D. C. Drucker and W. Prager. Soil mechanics and plastic analysis or limit design. *Quarterly Journal of Applied Mathematics*, 10:157–165, 1952.

[25] F. P. Ganneau, G. Constantinides, and F. J Ulm. Dual-indentation technique for the assessment of strength properties of cohesive-frictional materials. *International Journal of Solids and Structures*, 43(6):1727–1745, 3 2006.

[26] Benjamin Gathier. Multiscale strength homogenization : application to shale nanoindentation, 2008. Thesis Supervisor: Franz-Josef Ulm.

[27] P. Gilormini and E. Felder. Theoretical and experimental study of the ploughingof a rigid-plastic semi-infinite body by a rigid pyramidal indenter. *Wear*, 88(2):195–206, 7/1 1983.

[28] Stephen Gonczy and N. X. Randall. An astm standard for quantitative scratch adhesion testing of thin, hard ceramic coatings. *International Journal of Applied Ceramic Technology*, 2(5):422–428, 2005.

[29] A. A. Griffith. The phenomena of rupture and flow in solids. *Philosophical Transactions of the Royal Society of London Series A, Containing Papers of a Mathematical of Physical Character*, 221:163–198, 1921.

[30] A. V. Hershey. The elasticity of an isotropic aggregate of anisotropic cubic crystals. *Journal of Applied Mechanics*, 21:236–240, 1954.

[31] H. E. Hintermann. Adhesion, friction and wear of thin hard coatings. *Wear*, 100(1-3):381–397, 12 1984.

[32] K. L. Johnson. *Contact mechanics*. Cambridge University Press, 1985.

[33] K. Komvopoulos, N. Saka, and N. P. Suh. Plowing friction in dry and lubricated metal sliding. *Journal of Tribology*, 108(3):301–312, 1986.

[34] E. Krner. Berechnung der elastischen konstanten des vielkristalls aus den konstanten des einkristalls. *Zeitchrift fr Physik*, 151(4):504–518, 1958.

[35] Ki Myung Lee, Chang-Dong Yeo, and Andreas A. Polycarpou. Relationship between scratch hardness and yield strength of elastic perfectly plastic materials using finite element analysis. *Journal of Materials Research*, 23(8):2229–2237, August 2008.

[36] J. Meneve, H. Ronkainen, P. Andersson, K. Vercammen, D. Camino, D. G. Teer, J. Von Stebut, N. M. Gee, M. G. Banks, B. Bellaton, E. Matthaei-Schulz, and H. Vetters. *Scratch Adhesion Testing of Coated SurfacesChallenges and New Directions*, volume 2 of *Adhesion Measurement of Films and Coatings*, chapter 4, pages 79–106. VSP, Utrecht, 2001.

[37] S. Mitaim, F. Dagrain, T. Richard, E. Detournay, and A. Drescher. A novel apparatus to determine the rock strength parameters. 2004.

[38] James Kenneth Mitchell. *Fundamentals of soil behavior*. Wiley, New York, 1993. James K. Mitchell.; Bibliography: Includes bibliographical references (p. 407-425) and indexes.

[39] F. Mohs. *Grundriss der Mineralogie*. Arnoldschen Buchhandlung, Dresden, 1822.

[40] T. Mori and K. Tanaka. Average stress in matrix and average elastic energy of materials with misfitting inclusions. *Acta Metallurgica*, 21(5):571–574, 5 1973.

[41] W. C. Oliver and G. M. Pharr. Measurement of hardness and elastic modulus by instrumented indentation: advances in understanding and refinements to methodology. *Journal of Materials Research*, 19(1):3–20, 2004.

[42] Hugh O'Neill. *The hardness of metals and its measurement*. Chapman & Hall, ltd., London, 1934. by Hugh O'Neill.; Bibliography: "Bibliography and author index": p. 278-287.

[43] J. Alberto Ortega, Benjamin Gathier, and Franz-Josef Ulm. Homogenization of cohesive-frictional strength properties of porous composites: Linear comparison composite approach. *Under Review*.

[44] J. Alberto Ortega, Franz-Josef Ulm, and Younane Abousleimane. The effect of particle shape and grain-scale properties of shale: A micromechanics approach. *International Journal for Numerical and Analytical Methods in Geomechanics*, 2009.

[45] S. P. Paruchuru and A. Jain. Finite element modeling and experimental validation of computational procedures for a fracture mechanics based bone test method. *Trends in Biomaterials & Artificial Organs*, 21(1):1–7, 2007.

[46] Ivaldo D. S. Pontes, Lavinia A. Borges, Nestor Zouain, and Francisco R. Lopes. An approach to limit analysis with cone-shaped yield surfaces. *International Journal for Numerical Methods in Engineering*, 40(21):4011–4032, 1997.

[47] Ernest Rabinowicz. The nature of the static and kinetic coefficients of friction. *Journal of Applied Physics*, 22(11):1373–1379, November 1951 1951.

[48] Ernest Rabinowicz. *Friction and wear of materials*. Wiley, New York, 1965. Bibliography: Includes bibliographies.

[49] N. X. Randall, G. Favaro, and C. H. Frankel. The effect of intrinsic parameters on the critical load as measured with the scratch test method. *Surface and Coatings Technology*, 137(2-3):146–151, 3/15 2001.

[50] T. Richard, E. Detournay, A. Drescher, P. Nicodeme, and D. Fourmaintraux. The scratch test as a means to measure strength of sedimentary rocks. 8-10 July 1998 1998.

[51] Thomas Richard. Determination of rock strength from cutting tests, 1999. University of Minnesota, MS thesis.

[52] Gaëtan Rimmelé, Véronique Barlet-Gouédard, Olivier Porcherie, Bruno Goffé, and Fabrice Brunet. Heterogeneous porosity distribution in portland cement exposed to co2-rich fluids. *Cement and Concrete Research*, 38(8-9):1038–1048, 8 2008.

[53] J. Salençon. *Calcul à la rupture et analyse limite*. Presses de l'École nationale des ponts et chaussées edition, 1983.

[54] Tom Schanz and SpringerLink. *Experimental unsaturated soil mechanics [electronic resource]*. Springer, Berlin ; New York, 2007.

[55] G. Schei, E. Fjr, E. Detournay, C. J. Kenter, G. F. Fuh, and E. Detournay. The scratch test: An attractive technique for determining strength and elastic properties of sedimentary rocks. 14 October 2000.

[56] H. F. Schweiger. On the use of drucker-prager failure criteria for earth pressure problems. *Computers and Geotechnics*, 16(3):223–246, 1994.

[57] Nam P. Suh and H. C Sin. The genesis of friction. *Wear*, 69(1):91–114, 6/1 1981.

[58] David Tabor. *The hardness of metals*. Clarendon Press, Oxford, 2000. by D. Tabor.; Originally published: Oxford : Clarendon Press, 1951.; Bibliography: Includes index.

[59] Noureddine Tayebi, Thomas F. Conry, and Andreas A. Polycarpou. Determination of hardness from nanoscratch experiments: Corrections for interfacial shear stress and elastic recovery. *Journal of Materials Research*, 18(9):2150–2162.

[60] H. Tresca. Mmoire sur l'coulement des corps solides soumis de fortes pressions. *Comptes-rendus de l'Acadmie des Sciences*, 59:754, 1864.

[61] F. J Ulm and Olivier Coussy. *Mechanics and durability of solids*. Prentice Hall, Upper Saddle River, N.J., 2003. Franz-Josef Ulm, Oliver Coussy.; v. : ill. ; 24 cm.; Bibliography: Includes bibliographical references and indexes.

[62] J. Valli. A review of adhesion test methods for thin hard coatings. *Journal of Vacuum Science & Technology A: Vacuum, Surfaces, and Films*, 4(6):3007–3014, 1986.

[63] M. De Vathaire, F. Delamare, and E. Felder. An upper bound model of ploughing by a pyramidal indenter. *Wear*, 66(1):55–64, 1/15 1981.

[64] R. von Mises. Mechanik der festen korper im plastisch deformablen zustand. *Gottinger Nachrichten, Mathematik und Physik*, 1:582–592, 1913.

[65] V. B. Watwood. The finite element method for prediction of crack behavior. *Nuclear Engineering and Design*, 11(2):323–332, 3 1970.

[66] J. A. Williams. Analytical models of scratch hardness. *Tribology International*, 29(8):675–694, 12 1996.

[67] Y. Xie and H. M. Hawthorne. On the possibility of evaluating the resistance of materials to wear by ploughing using a scratch method. *Wear*, 240(1-2):65–71, 5 2000.

[68] A. T. Zehnder. *Lecture Notes on Fracture Mechanics*. March 31 2008.